PIM-1-DERIVED CARBON MOLECULAR SIEVE HOLLOW FIBER MEMBRANES FOR ORGANIC SOLVENT REVERSE OSMOSIS

A Dissertation
Presented to
The Academic Faculty

By

Melinda L. Jue

In Partial Fulfillment
Of the Requirements for the Degree
Doctor of Philosophy in the
School of Chemical & Biomolecular Engineering

Georgia Institute of Technology

December 2017

PIM-1-DERIVED CARBON MOLECULAR SIEVE HOLLOW FIBER MEMBRANES FOR ORGANIC SOLVENT REVERSE OSMOSIS

Approved by:

Dr. Ryan P. Lively, Advisor
School of Chemical & Biomolecular Engineering
Georgia Institute of Technology

Dr. William J. Koros
School of Chemical & Biomolecular Engineering
Georgia Institute of Technology

Dr. Victor Breedveld
School of Chemical & Biomolecular Engineering
Georgia Institute of Technology

Dr. Peter J. Ludovice
School of Chemical & Biomolecular Engineering
Georgia Institute of Technology

Dr. M. G. Finn
School of Chemistry and Biochemistry
Georgia Institute of Technology

Dr. Benjamin A. McCool
Advanced Research Associate
ExxonMobil Research and Engineering

Date Approved: October 25, 2017

ACKNOWLEDGEMENTS

I would first like to thank all of my friends and family who supported me during graduate school and made this thesis possible. The many adventures filled with laughter have made this experience truly unforgettable. I would like to thank all of the members of the Lively Lab, and in particular Brian Pimentel and Simon Pang for keeping me sane and grounded. Undoubtedly, I have not thanked many of the people who have helped me along the way, but for the sake of brevity, I am grateful for their support nonetheless.

I would like to thank my thesis committee members Dr. Victor Breedveld, Dr. M. G. Finn, Dr. William J. Koros, Dr. Peter J. Ludovice, and Dr. Benjamin A. McCool for their supervision and suggestions over the years. Finally, I would like to thank my advisor Dr. Ryan P. Lively for the continued support and guidance that allowed me to grow as a scientist and an individual. I achieved more than I ever dreamed of during graduate school and I got to travel the world, for science.

TABLE OF CONTENTS

ACKNOWLEDGEMENTS iii

LIST OF TABLES vii

LIST OF FIGURES ix

SUMMARY xvi

CHAPTER 1. INTRODUCTION 1
1.1 Organic Solvent Separations 1
1.2 Organic Solvent Reverse Osmosis 6
1.3 Overview of Work 7
1.4 References 8

CHAPTER 2. MICROPOROUS MATERIALS FOR CHALLENGING ORGANIC SOLVENT SEPARATIONS 10
2.1 Introduction 10
2.2 Current State of the Art 12
2.2.1 Microporous Polymers 12
2.2.2 Metal-organic Frameworks 15
2.2.3 Zeolites 21
2.2.4 Carbons 24
2.2.5 Composites 27
2.3 Defects 30
2.4 Conclusions 32
2.5 References 34

CHAPTER 3. TRANSPORT AND ANALYSIS IN MEMBRANES 44
3.1 Gas Transport in Polymeric Membranes 44
3.2 Organic Vapor Transport in Polymers 51
3.3 Organic Solvent Sorption and Transport in Carbon Molecular Sieve Membranes 55
3.4 References 58

CHAPTER 4. ORGANIC MOLECULE TRANSPORT IN THE MICROPOROUS POLYMER PIM-1 60
4.1 Introduction 60
4.2 Experimental 62
4.2.1 Materials 62
4.2.2 Synthesis of PIM-1 62
4.2.3 Film Casting 63
4.2.4 Organic Vapor Sorption 63

4.2.5 Nonsolvent-induced Swelling Test 63
4.2.6 Liquid Permeation 64
4.3 Results and Discussion 65
4.3.1 Organic Vapor Sorption 65
4.3.2 Organic Vapor Diffusion 68
4.3.3 Additional Nonsolvent Transport Data 73
4.3.4 Swelling and Plasticization 75
4.3.5 Organic Liquid Permeation 78
4.4 Conclusions 81
4.5 References 83

CHAPTER 5. FABRICATION OF DEFECT-FREE PIM-1 HOLLOW FIBER MEMBRANES 85
5.1 Introduction 85
5.2 Experimental 87
5.2.1 Materials 87
5.2.2 Spin Dopes 88
5.2.3 Hollow Fiber Spinning 88
5.2.4 Hollow Fiber Module Preparation 91
5.2.5 Single Fiber Gas Permeation 91
5.2.6 Surface Area and Pore Size Analysis 92
5.2.7 Scanning Electron Microscopy 92
5.3 Results and Discussion 93
5.3.1 Development of Ternary Phase Diagrams 93
5.3.2 Bore Fluid Composition 98
5.3.3 Sheath Layer Composition 100
5.3.4 Spin 1 103
5.3.5 Spin 2 104
5.3.6 Spin 3 107
5.3.7 Gas Permeation 110
5.3.8 Additional Fiber Properties 116
5.4 Conclusions 118
5.5 References 120

CHAPTER 6. NONSOLVENT CONDITIONING OF PIM-1 125
6.1 Introduction 125
6.2 Experimental 127
6.2.1 Materials 127
6.2.2 Synthesis and Fabrication of PIM-1 Hollow Fiber Membranes 128
6.2.3 Nitrogen Physisorption 128
6.2.4 Thermogravimetric Analysis 128
6.2.5 Fiber Swelling Measurements 129
6.2.6 Scanning Electron Microscopy 129
6.2.7 Defect Treatments 130
6.2.8 Gas Permeation 130
6.3 Results and Discussion 130

6.3.1 Nonsolvent Evaporation 130
6.3.2 Nonsolvent Choice 135
6.3.3 Alternative Nonsolvent Treatments 139
6.3.4 Defect Treatment in PIM-1 Hollow Fiber Membranes 142
6.3.5 Aging 149
6.4 Conclusions 150
6.5 References 151

CHAPTER 7. FORMATION AND SEPARATION PERFORMANCE OF PIM-1-DERIVED CARBON MOLECULAR SIEVE HOLLOW FIBER MEMBRANES FOR ORGANIC SOLVENT REVERSE OSMOSIS 154
7.1 Introduction 154
7.2 Experimental 157
7.2.1 Materials 157
7.2.2 CMS Formation 157
7.2.3 Physisorption 158
7.2.4 Scanning Electron Microscopy 159
7.2.5 Organic Vapor Sorption Isotherms 159
7.2.6 Fiber Module Assembly 159
7.2.7 Gas Permeation 160
7.2.8 Organic Liquid Permeation 160
7.3 Results and Discussion 148
7.3.1 CMS Characterization 148
7.3.2 Membrane Separations 166
7.4 Conclusions 172
7.5 References 174

CHAPTER 8. CONCLUSIONS AND RECOMMENDATIONS 176
8.1 Summary 176
8.2 Future Work 178
8.3 Critical Needs 181
8.3.1. Pore Size Control 181
8.3.2 Scalable Microporous Membrane Materials 185
8.3.3 Consistent Methods, Testing, and Analysis 186
8.4 References 189

LIST OF TABLES

Table 1.1	Examples of potential organic solvent separations.	3
Table 2.1	Enthalpic and entropic contributions to the diffusion selectivity of propane and propylene in ALPO-34 and ZIF-8.	18
Table 3.1	Kinetic diameters and boiling points of industrially relevant gases.	45
Table 5.1	Spinning parameters for States S1, S2, and S3. The spinneret was kept at 22°C and the water quench bath at 50°C for each spin.	90
Table 5.2	Single component gas permeation results at 100 psig feed pressure and 35°C for a single State S2 PIM-1 fiber. The skin layer is estimated to be 5.8 μm thick based on SEM images.	107
Table 5.3	Single component gas permeation results at 100 psig feed pressure and 35°C for a single State S3 PIM-1 fiber. The skin layer is estimated to be 2.8 μm thick based on SEM images.	110
Table 5.4	Pure component gas permeances for State S3 PIM-1 fibers and reported hollow fiber membranes.	112
Table 5.5	Tabulated gas permeances for State S3 PIM-1 hollow fibers at 100 psig feed pressure at 25 and 45°C.	113
Table 5.6	Ideal selectivities relative to nitrogen for State S3 PIM-1 fibers and reported flat sheet membranes.	114
Table 5.7	Activation energies of permeation of State S3 PIM-1 fibers and reported flat sheet membranes.	115
Table 5.8	BET surface areas based on nitrogen physisorption at 77 K for PIM-1 powder and State S3 PIM-1 hollow fibers.	117
Table 6.1	BET surface area and pore volume of different DMF-conditioned PIM-1 powders as determined by nitrogen physisorption at 77 K.	133
Table 6.2	BET surface areas and pore volumes for PIM-1 films determined from nitrogen physisorption at 77 K.	136
Table 6.3	BET surface areas and pore volumes for different nonsolvent-conditioned PIM-1 powders determined from nitrogen physisorption at 77 K.	141

Table 7.1 Temperature protocol for pyrolyzing PIM-1 powders. 158

Table 7.2 Modified pyrolysis protocol for CMS fibers. 168

LIST OF FIGURES

Figure 1.1	Schematic of a simple membrane-based organic solvent separation.	3
Figure 1.2	(a) Idealized schematic of organic molecule transport through an ultramicropore (<0.7 nm) of an OSRO membrane (left) and a supermicropore (0.7 – 2 nm) of a defective OSRO or OSN membrane (right). The applied pressure is from the top of the membrane to the bottom. (b) OSRO follows a fugacity/chemical potential driving force while OSN follows a pressure driving force. The dashed line indicates a typical operating pressure for OSRO-type separations. The fugacity/chemical potential driving force through a defect-free pathway is often 100x less than the pressure driving force through a defective pathway in an OSRO membrane.	6
Figure 2.1	(a) Chemical structures of microporous polyarylate polymers and (b) their associated molecular weight cutoff curves for polystyrene oligomers in THF measured at 30 bar and 30°C.	14
Figure 2.2	(a) ZIF-8 window size distributions at 35°C with various adsorbates positioned in the window and (b) activation energies of diffusion as a function of guest molecule kinetic diameter for ZIF-8, zeolite 4A, and zeolite 5A.	17
Figure 2.3	(a) Schematic of MOF formation on the bore side of a porous hollow fiber precursor using the interfacial microfluidic membrane processing (IMMP) technique. (b) SEM image of a ZIF-8 membrane grown on a Torlon® hollow fiber support.	20
Figure 2.4	(a) SEM image of MFI nanosheets after seed removal, scale bar represents 1 μm. (b) *p*-Xylene permeance and *p*-xylene/*o*-xylene selectivity for MFI membranes measured with a Wicke-Kallenbach system. Black circles represent single component *p*-xylene permeances taken at decreasing temperature, white circles represent increasing temperature. Red squares represent *p*-xylene permeances for an equimolar *p*-xylene/*o*-xylene mixture, white squares indicate the separation factor.	22
Figure 2.5	(a) Fabrication scheme of asymmetric CMS hollow fiber membranes made from PVDF. (b) Room temperature mixture permeate composition from a CMS fiber pyrolyzed at 550°C.	25

Figure 2.6 (a) Mixed matrix membrane made with 20 wt% of 300 nm unmodified pure silica MFI in Ultem®. Undesirable sieve-in-a-cage morphology is exhibited due to the poor interfacial adhesion of the zeolite and polymer. (b) Mixed matrix membrane made with 15 wt% of 800 nm ZIF-90 in Ultem®. Good filler adhesion is achieved without the need for surface modification of the MOF. 29

Figure 3.1 The contribution of Langmuir sorption at low pressures and Henry's law sorption at high pressures typical of dual mode sorption in glassy polymers. 48

Figure 4.1 Reaction scheme for the low temperature synthesis of PIM-1. 61

Figure 4.2 Sorption isotherms in PIM-1 from 25 to 55°C for (a) DMF and (b) methanol. Film thickness ranged from 50-90 μm. Error bars represent the standard deviation of at least three isotherm measurements, each on different films. Some error bars are smaller than the size of the marker. 66

Figure 4.3 DMF and methanol isosteric heats of sorption as a function of nonsolvent loading. The dashed lines represent the corresponding heat of condensation for each nonsolvent. 68

Figure 4.4 Normalized mass uptake curves for DMF (a) sorption and (b) desorption in PIM-1 with the corresponding fits for the short-time uptake analysis. The sorption step shown is from 0.10 to 0.25 relative pressure and the desorption step from 0.40 to 0.25 relative pressure at 25°C. DMF sorption in PIM-1 is Case II diffusion and DMF desorption in PIM-1 is anomalous diffusion. 69

Figure 4.5 Kinetic sorption data for DMF (red squares) and methanol (gray circles) in PIM-1 for the desorption step from 0.40 to 0.25 relative pressure at 55°C. The Berens-Hopfenberg model with exponential boundary conditions is overlaid (black line) for each curve. The swelling-corrected half thickness of the DMF and methanol films are 33 ± 1 and 31 ± 1 μm, respectively. 70

Figure 4.6 Thermodynamically corrected diffusion coefficients for (a) DMF and (b) methanol in PIM-1 as a function of loading at different temperatures. The error bars represent the standard deviations of at least three individual desorption experiments. 72

Figure 4.7 (a) Sorption isotherms and (b) thermodynamically corrected diffusion coefficients of *n*-heptane in PIM-1 from 25 to 55°C. Film thickness ranged from 60-80 μm. Error bars represent the standard deviation of at least three isotherm measurements, each on different methanol treated films. 73

Figure 4.8	(a) Sorption isotherms and (b) thermodynamically corrected diffusion coefficients of toluene in PIM-1 from 25 to 55°C. Film thickness ranged from 60-80 μm. Error bars represent the standard deviation of at least three isotherm measurements, each on different methanol treated films.	74
Figure 4.9	(a) Sorption isotherms and (b) thermodynamically corrected diffusion coefficients of *o*-xylene in PIM-1 from 25 to 55°C. Film thickness ranged from 60-80 μm. Error bars represent the standard deviation of at least three isotherm measurements, each on different methanol treated films.	74
Figure 4.10	(a) Sorption isotherms and (b) thermodynamically corrected diffusion coefficients of *p*-xylene in PIM-1 from 25 to 55°C. Film thickness ranged from 60-80 μm. Error bars represent the standard deviation of at least three isotherm measurements, each on different methanol treated films.	75
Figure 4.11	One dimensional organic-induced swelling in PIM-1 at 25°C. Error bars represent the standard deviation measured from three films.	77
Figure 4.12	(a) Room temperature methanol permeability in PIM-1. (b) Room temperature *n*-heptane permeability in PIM-1. The predicted permeability based on the solution-diffusion model is shown by the dashed line and the uncertainty in gold.	80
Figure 5.1	Schematic of the spinning apparatus and triple orifice spinneret used to produce PIM-1 hollow fiber membranes. The bore fluid is shown in green, the polymer dope in yellow, and the sheath layer in blue. The three fluids are simultaneously coextruded through the spinneret into the water quench bath, moved around guides, and collected on the take up drum.	89
Figure 5.2	Ternary phase diagram for various PIM-1 solutions. The binodal line for PIM-1/THF/DMAc/EtOH with a constant DMAc to EtOH ratio of 85 wt% to 15 wt% (red circles) and binodal line for PIM-1/THF/NMP (blue squares) are shown. The upwards triangle indicates the dope composition used in Spin 1 and the downwards triangle indicates the dope composition used in Spins 2 and 3.	95
Figure 5.3	Ternary phase diagrams showing the binodal lines for three nonvolatile nonsolvents—PIM-1/THF/water (red circles), PIM-1/THF/DMAc (blue squares), and PIM-1/THF/NMP (green triangles).	96
Figure 5.4	Ternary phase diagram showing the binodal line for the volatile nonsolvent PIM-1/THF/EtOH system.	96

Figure 5.5 Ternary phase diagram for PIM-1/THP/EtOH. 97

Figure 5.6 SEM images of PIM-1 fibers spun using different bore fluid compositions. (a) A fiber spun using 85/15 wt% DMAc/EtOH that produced an internal skin layer. (b) A fiber spun using 60.75/10.75/28.5 wt% DMAc/EtOH/THF bore fluid that produced a somewhat dense, but smooth internal layer. (c) A fiber spun using 46.75/8.25/45 wt% DMAc/EtOH/THF bore fluid with a smooth internal layer. (d) A fiber spun using 38.25/6.75/55 wt% DMAc/EtOH/THF with a rough internal layer. 99

Figure 5.7 PIM-1 hollow fiber spun from a Spin 2 dope without a sheath layer. 100

Figure 5.8 PIM-1 hollow fibers spun using sheath layers composed of (a) 100 wt% NMP, (b) 87.6/12.4 wt% NMP/PVP, (c) 69/31 wt% NMP/PVP, and (d) 37.3/44.5/18.2 wt% NMP/PVP/THF. 102

Figure 5.9 PIM-1 hollow fibers produced from (a) and (b) a 100 wt% 1-butanol sheath layer and (c) and (d) a 25/75 wt% 1-butanol/THF sheath layer. 103

Figure 5.10 SEM images of (a) the cross section and (b) the skin layer and substructure of a PIM-1 hollow fiber produced from State S1 utilizing a pure 1-butanol sheath layer. 104

Figure 5.11 SEM images of (a) the cross section and (b) the skin layer and substructure of a PIM-1 hollow fiber produced from State S2 utilizing a pure 1-butanol sheath layer. 105

Figure 5.12 Mercury intrusion in the relatively dense State S1 fibers compared to the porous States S2 and S3 fibers. 105

Figure 5.13 Effect of THF concentration in the 1-butanol sheath layer on the unaged fiber selectivity. Pure component gas permeation experiments were conducted on single fiber modules with a 100 psig feed pressure at 35°C. The black line is used to guide the eye. 108

Figure 5.14 SEM images of a defect-free State S3 PIM-1 hollow fiber (a) cross section, (b) asymmetric substructure, (c) internal boundary, and (d) skin layer spun with a 17.5 wt% THF in 1-butanol sheath layer. 109

Figure 5.15 Linear regression plots for various gases in aged PIM-1 hollow fibers. 116

Figure 5.16 Nitrogen physisorption at 77 K of PIM-1 powder and State S3 PIM-1 hollow fibers. 117

Figure 6.1 Nitrogen physisorption at 77 K in PIM-1 powders conditioned with differing DMF removal rates. The fast DMF-conditioned sample was soaked in DMF, vacuum filtered, and completely dried during degas at 115°C under $1x10^{-6}$ torr vacuum. The slow DMF-conditioned sample was soaked in DMF, completely dried in a vacuum oven at 80°C under 36 torr vacuum, and then degassed under the same conditions. 132

Figure 6.2 Normalized mass loss during in-situ, pre-analysis drying of methanol-conditioned and DMF-conditioned PIM-1 films. Data shown are during the 1°C/min ramp from 25 to 115°C under flowing dry nitrogen. The methanol-conditioned film was soaked in methanol for 24 hours before in-situ drying. The DMF-conditioned film was soaked in methanol for 24 hours then soaked in DMF for 24 hours before in-situ drying. 134

Figure 6.3 Nitrogen physisorption at 77 K in as-cast (black squares), DMF-conditioned (red circles), and methanol-conditioned (blue triangles) dense PIM-1 films. 136

Figure 6.4 Thermogravimetric analysis curves of as-cast, DMF-conditioned, and methanol-conditioned PIM-1 films. The temperature profile consist of a 10°C/min ramp to 100°C, a one hour hold at 100°C, and a second 10°C/min ramp to 1000°C under a nitrogen atmosphere. 138

Figure 6.5 Nitrogen physisorption at 77 K in diethyl ether-conditioned, methanol-conditioned, acetone-conditioned, and DMF-conditioned PIM-1 powders. 140

Figure 6.6 SEM images of a DMF-conditioned PIM-1 fiber (a) cross section, (b) wall cross section, (c) internal surface layer, and (d) external skin layer. 143

Figure 6.7 Nonsolvent-induced swelling and subsequent shrinkage after drying for PIM-1 hollow fiber membranes. Fibers were measured dry, soaked in various aqueous DMF solutions for 24 hours, dried under vacuum at 80°C, and then remeasured. The relative skin thickness is a measure of the thickness occupied by the skin layer relative to the entire fiber wall. 144

Figure 6.8 (a) PIM-1 fiber treated with a 0 wt% DMF aqueous solution. (b) PIM-1 fiber treated with a 25 wt% DMF aqueous solution. (c) PIM-1 fiber treated with a 50 wt% DMF aqueous solution. (d) PIM-1 fiber treated with an 80 wt% DMF aqueous solution. 145

Figure 6.9 (a) and (c) Porous PIM-1 film without any conditioning. (b) and (d) Porous PIM-1 film after conditioning with a 50 wt% DMF aqueous solution. 146

Figure 6.10 PIM-1 hollow fiber membrane performance after various nonsolvent treatments. Carbon dioxide and methane permeation were measured at 35°C and 100 psig. The black circle represents the unmodified, slightly defective control fiber and the grey star a defect-free, aged fiber. The red squares represent fibers soaked for 24 hours and dried overnight, the green diamonds fibers soaked for 1 hour and dried for 1 hour, and the blue triangles fibers soaked for 1 hour and dried overnight with the DMF wt% in the aqueous solution given above the symbol. Arrows are drawn to guide the eye. The open circle represents fibers soaked in a 0 wt% DMF solution, crossed circle methanol exchanged fibers, and crossed square ambient dried fibers. The 2008 upper bound for a 1 μm thick membrane is drawn for comparison. 148

Figure 7.1 Hypothetical change in CMS pore size distribution with increasing pyrolysis temperature. 155

Figure 7.2 CMS hollow fiber membrane module made from ¼ inch Swagelok® fittings. 159

Figure 7.3 Schematic of dual-pump crossflow system for OSRO testing. 161

Figure 7.4 (a) Asymmetric hollow fiber membrane with a thin skin layer. (b) Asymmetric hollow fiber membrane after substructure collapse exhibiting a thick skin layer. 162

Figure 7.5 (a) and (c) PIM-1 hollow fiber membrane. (b) and (d) CMS hollow fiber membrane pyrolyzed from unmodified PIM-1. 163

Figure 7.6 Carbon dioxide physisorption isotherms at 195 K for PIM-1 pyrolyzed at various temperatures. 164

Figure 7.7 Total pore volume for PIM-1-derived CMS as determined from CO_2 physisorption at 195 K and reported crosslinked PVDF-derived CMS as determined from N_2 physisorption at 77 K. 165

Figure 7.8 *p*-Xylene sorption isotherms at 35°C for PIM-1 and PIM-1-derived CMS pyrolyzed at 575°C, and at 25°C for crosslinked PVDF CMS. 166

Figure 7.9 UV-Vis spectra of rose bengal in THF solutions for a PIM-1-derived CMS membrane pyrolyzed at 750°C. The membrane was run in dead end filtration mode with an applied pressure of 500 psig at room temperature. 167

Figure 7.10 Gas separation performance of PIM-1-derived CMS pyrolyzed at 575°C and crosslinked PVDF-derived CMS. The 2008 Robeson polymer upper bound is given as a reference. 169

Figure 7.11 (a) Room temperature mixture permeation of *p*-xylene and 1,3,5-triisopropylbenzene. A 95 mol% *p*-xylene feed is enriched up to 97 mol% *p*-xylene in a single stage. (b) The corresponding separation factors for each composition. The arrow is in the direction of increasing hydraulic pressure. 170

Figure 7.12 Mixture permselectivity of *p*-xylene/1,3,5-triisopropylbenzene at ambient temperature using PIM-1-derived CMS pyrolyzed at 575°C. The arrow is in the direction of increasing hydraulic pressure. The *p*-xylene permeances for the separation of *p*-xylene/*o*-xylene mixtures using crosslinked PVDF CMS is highlighted in gold. 172

Figure 8.1 (a) Skin layer of an as-spun PIM-1 hollow fiber membrane. (b) Skin layer of a 50 wt% DMF/water treated and pyrolyzed CMS hollow fiber membrane. 180

SUMMARY

Current separation technologies rely heavily on energy-intensive methods such as distillation, crystallization, and absorption to separate organic molecules. Utilization of membrane-based organic solvent separations—that avoid phase changes during separation—could revolutionize the field by enabling new low energy, low carbon emission technologies. However, existing membrane materials are unable to achieve the separation efficiency required to differentiate between very similarly sized organic molecules. Microporous materials are potential game changers in this area due to their ability to provide superb size and shape discrimination. Polymers of intrinsic microporosity (PIMs) are an emerging subclass of materials with rigid backbones that lead to high membrane performance combined with solution processability. To bridge the gap between the development of new, high performance polymers and industrially attractive technologies, more efficient membrane units such as hollow fibers are needed. This work describes the organic solvent molecule transport in and the fabrication of defect-free, asymmetric hollow fiber membranes from PIM-1. These membranes are then used as precursors for the development and proof-of-concept demonstration of microporous carbon molecular sieve membranes for the molecular differentiation of organic solvent molecules. The work here spans a wide range of membrane science and engineering from polymer synthesis, membrane fabrication, and fundamental transport analysis, to module formation and testing.

CHAPTER 1. INTRODUCTION

Current separation technologies rely on energy-intensive methods such as distillation, crystallization, and absorption to separate organic molecules. Utilization of membrane-based separations could significantly decrease the energy demand of such processes by avoiding phase changes during separation. However, existing membrane materials are unable to achieve the separation efficiency required to differentiate between very similarly sized organic molecules such as isomers. Microporous materials offer superb size and shape discrimination and are potential candidate materials for these advanced separations. The development and proof-of-concept demonstration of microporous polymer-derived carbon hollow fiber membranes for the molecular differentiation of organic solvent molecules are described. The work here spans a wide range of membrane science and engineering from polymer synthesis, membrane fabrication, and fundamental transport analysis, to module formation and testing.

1.1 Organic Solvent Separations

The industrial production of chemicals and fuels relies heavily on established separation technologies such as distillation, crystallization, and absorption. Currently, these thermal separations consume anywhere up to 50% of the total energy required for the production processes associated with fuels, chemicals, pharmaceuticals, and water.[1] By avoiding these energy-intensive phase changes during separation, new low energy, low carbon emission separations could be realized. Membranes are one such technology that have been developed to meet these needs. Membrane separations utilize as little as 10% of the energy required for thermal-based desalination technologies.[2-4] The earliest filtration

membranes were able to differentiate between molecules of 10-100x difference in size and evolved to handle size differences of ~3x, in the case of seawater reverse osmosis; today, certain gas separation membranes can separate molecules with just 1.05-1.5x difference in size.[2] Indeed, membrane technology is now the state of the art for seawater desalination facilities[3] and is also competitive in certain gas separations such as air separation,[5] hydrogen recovery,[5] and natural gas processing[5] and is emerging as a leading technology for revolutionizing olefin/paraffin separations.[6]

Recent developments in organic and inorganic material processing have enabled the formation of ultrathin, chemically stable membranes with a high degree of molecular specificity and productivity. These new advanced materials will extend the capabilities of membrane separations into applications involving more aggressive and complex feed mixtures. One area of membrane science that has yet to be extensively investigated—in comparison to the work on gas and water separations—is that of organic solvent separations as shown schematically in Figure 1.1. Organic solvent separations cover a wide range of possible applications including biofuels,[7] pharmaceuticals,[8] and petrochemicals.[9] Several example applications that could benefit from membrane-based organic solvent separations are listed in Table 1.1, along with estimates of the global scale and membrane properties required. Additional examples outside the ones listed, and in particular, those related to pharmaceutical manufacturing, semiconductor waste processing, and biochemical production can also be envisioned, but detailed data on the latter fields is lacking and therefore not included in the table. The exponential growth in membrane research related to organic solvent systems is clear evidence of the broad interest and potential applicability of these types of separations.[10]

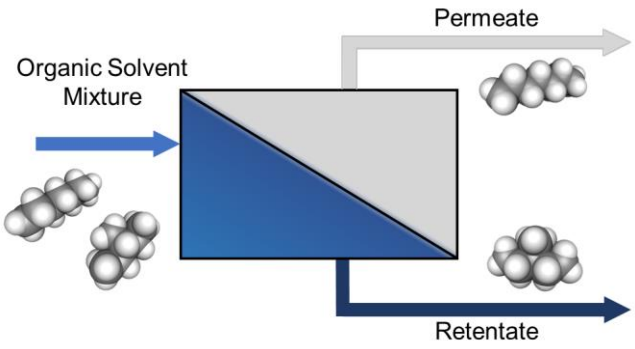

Figure 1.1 Schematic of a simple membrane-based organic solvent separation.

Table 1.1 Examples of potential organic solvent separations.

Class	Compound	Example Separation	Required Pore Size (Å)	Global Production (billion pounds/year)
Alkane	Gasoline	*n*-Heptane/isooctane	5-6	2260[a]
	Alkylate	Isobutane/isooctane	5-6	96[b]
Aromatic	*p*-Xylene	*p*-Xylene/*o*-xylene	5.5	65[c]
	Benzene	Benzene/ethylbenzene	5.3-5.8	15[d]
Biofuel	Bioethanol	Water/ethanol	3-4	120[e]
	Biodiesel	Glycerol/fatty acid methyl ester	6-7	60[e]

[a]Data from ref 11.
[b]Data from ref 12 given in oil equivalents for US production only.
[c]Data from ref 13.
[d]Data from ref 14.
[e]Data from ref 15 given in oil equivalents.

Existing membrane-based organic separations have focused on either the separation of organic vapors[16] or the filtration of large solutes from much smaller solvent molecules.[8] However, the former systems necessitate the availability or generation of vapors,

potentially through energy-intensive steps. Conversely, the separation of entirely liquid phase organic molecules from one another without the need for vaporization or condensation could be a paradigm shift for hydrocarbon and chemical processing. Membrane-based organic separations such as organic solvent nanofiltration (OSN) are a burgeoning area of membrane science and technology. OSN exists at the intersection of pressure driven filtration and chemical potential driven separations and can effectively separate organic molecules with at least an order of magnitude size difference.[17] Fully chemical potential driven organic solvent separations—such as organic solvent reverse osmosis (OSRO)—are in their very infancy, and are being developed to provide even finer distinctions between organic molecules. Hybrid systems such as organic solvent forward osmosis (OSFO) utilize a multistage approach to first separate molecules via chemical potential driven flow—without the need for applied pressure—followed by regeneration of the system streams.[10] In the OSN case, the separation can be thought of as a "solute/solvent" separation; whereas in the case of OSRO, this molecular classification becomes less clear and can be thought of as a "solvent/solvent" separation. However, it is clearer to classify OSRO based on the choice and size of the preferred permeating molecule, which is analogous to the classification system used in gas separations.

The driving force for OSRO separations—based on chemical potential differences across the membrane—is substantially lower than those found in gas separations and pressure-driven filtration-type separations.[4] The chemical potential or fugacity gradient across an OSRO membrane is low as a result of the liquid phases maintained on both the upstream and downstream faces. Consequently, large membrane areas and high applied pressures are needed to maximize the device productivity and overcome the osmotic

pressure of the feed. Therefore, thin membranes are critical for effective OSRO operation, as these best reduce the usage of the already limited driving force across the membrane. As with all membrane applications, even a low concentration of defects can be extremely detrimental to the separation performance. Critically, OSRO separations are particularly inhibited by the presence of defects. The defect pathways in OSRO membranes can result in pores that enable pressure-driven hindered diffusion[18] as opposed to the chemical potential-driven permeation associated with defect-free pathways as illustrated in Figure 1.2. The large differences in driving force for these two pathways suggests that defect permeation will completely dominate the mass transfer in even slightly defective OSRO membranes. Considering this, it is imperative that OSRO membranes essentially be (i) devoid of defects, (ii) highly pressure- and chemical-resistant, and (iii) fabricated in a scalable membrane morphology.

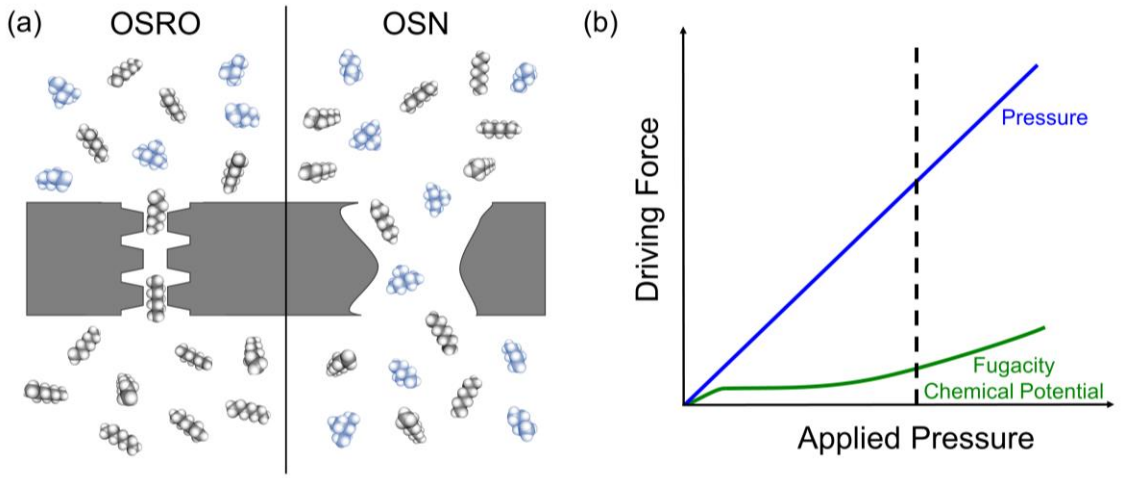

Figure 1.2 (a) Idealized schematic of organic molecule transport through an ultramicropore (< 0.7 nm) of an OSRO membrane (left) and a supermicropore (0.7 – 2 nm) of a defective OSRO or OSN membrane (right). The applied pressure is from the top of the membrane to the bottom. (b) OSRO follows a fugacity/chemical potential driving force while OSN follow a pressure driving force. The dashed line indicates a typical operating pressure for OSRO-type separations. The fugacity/chemical potential driving force through a defect-free pathway is often 100x less than the pressure driving force through a defective pathway in an OSRO membrane.

1.2 Organic Solvent Reverse Osmosis Membranes

An asymmetric CMS hollow fiber membrane meets all of the desirable qualities for an ideal OSRO membrane. Not only is the material chemically inert, membranes in this morphology have high pressure resistance and can be scaled up industrially. The selective layer on an asymmetric membrane can be made very thin—less than 100 nm—yet still remain defect-free.[19] Formation of precursor asymmetric hollow fiber membranes have been reported for a variety of polymers. However, crosslinking or other pretreatments are typically required to maintain the asymmetric structure during high temperature pyrolysis. Depending on the type of crosslinking chemistry, this can lead to a number of additional steps to the fabrication process and potentially introduce to defects. Especially for these

somewhat delicate, multi-step systems, any reduction in the number of fabrication steps or improvements in the reliability can greatly improve the large-scale viability of CMS membranes for OSRO.

1.3 Overview of Work

Building upon the initial success of crosslinked PVDF CMS hollow fiber membranes for OSRO,[19] the focus of this body of work is to develop a simpler fabrication route from polymer to final carbon hollow fiber membrane. A prototypical microporous polymer, polymer of intrinsic microporosity 1 (PIM-1), is used as the precursor material due to its highly rigid backbone and well documented separation performance. The transport of various organic solvents in PIM-1 is examined to evaluate the baseline ability of the polymer to differentiate between highly solvating organic molecules. Next, the development of defect-free PIM-1 hollow fibers—the first of its kind—is discussed with accompanying gas separation performance. These PIM-1 hollow fibers are directly pyrolyzed to form CMS hollow fibers without the need for any crosslinking steps. Finally, the organic solvent reverse osmosis separation of solvent mixtures is described. Suggestions for future work and perspectives on organic solvent separations are given as well.

1.4 References

(1) O. R. N. Laboratory (Ed.). Materials for Separation Technologies: Energy and Emission Reduction Opportunities. Oak Ridge, TN, 2005.

(2) Koros, W. J.; Lively, R. P. Water and beyond: Expanding the spectrum of large-scale energy efficient separation processes. *AIChE J.* **2012**, *58*, 2624-2633.

(3) Elimelech, M.; Phillip, W. A. The Future of Seawater Desalination: Energy, Technology, and the Environment. *Science* **2011**, *333*, 712-717.

(4) Cussler, E. L.; Dutta, B. K. On separation efficiency. *AIChE J.* **2012**, *58*, 3825-3831.

(5) Baker, R. W. Future Directions of Membrane Gas Separation Technology. *Ind. Eng. Chem. Res.* **2002**, *41*, 1393-1411.

(6) Koros, W. J.; Zhang, C. Materials for next-generation molecularly selective synthetic membranes. *Nat. Mater.* **2017**, *16*, 289-297.

(7) Atadashi, I. M.; Aroua, M. K.; Aziz, A. A. Biodiesel separation and purification: A review. *Renew. Energ.* **2011**, *36*, 437-443.

(8) Marchetti, P.; Jimenez Solomon, M. F.; Szekely, G.; Livingston, A. G. Molecular Separation with Organic Solvent Nanofiltration: A Critical Review. *Chem. Rev.* **2014**, *114*, 10735-10806.

(9) Gould, R. M.; White, L. S.; Wildemuth, C. R. Membrane separation in solvent lube dewaxing. *Environ. Prog.* **2001**, *20*, 12-16.

(10) Lively, R. P.; Sholl, D. S. From water to organics in membrane separations. *Nat. Mater.* **2017**, *16*, 276-279.

(11) U.S. Energy Information Administration. International Energy Statistics. https://www.eia.gov/beta/international/?src=-f4 (accessed Oct 17, 2017).

(12) U.S. Department of Energy. Bandwidth Study on Energy Use and Potential Energy Saving Opportunities in U.S. Petrolium Refining. 2015.

(13) International Energy Agency. Energy and GHG Reductions in the Chemical Industry via Catalytic Processes. 2013.

(14) Energetics Inc. Energy and Environmental Profile of the U.S. Chemical Industry. Columbia, Maryland, 2000.

(15) BP. BP Statistical Review of World Energy 2017. 2017.

(16) Smitha, B.; Suhanya, D.; Sridhar, S.; Ramakrishna, M. Separation of organic–organic mixtures by pervaporation—a review. *J. Membrane Sci*. **2004**, *241*, 1-21.

(17) Silva, P.; Han, S.; Livingston, A. G. Solvent transport in organic solvent nanofiltration membranes. *J. Membrane Sci*. **2005**, *262*, 49-59.

(18) Malone, D. M.; Anderson, J. L. Hindered diffusion of particles through small pores. *Chem. Eng. Sci*. **1978**, *33*, 1429-1440.

(19) Koh, D.-Y.; McCool, B. A.; Deckman, H. W.; Lively, R. P. Reverse osmosis molecular differentiation of organic liquids using carbon molecular sieve membranes. *Science* **2016**, *353*, 804-807.

CHAPTER 2. MICROPOROUS MATERIALS FOR CHALLENGING ORGANIC SOLVENT SEPARATIONS

Organic solvent separations could revolutionize the field of separations by enabling new low energy, low carbon emission technologies. Microporous materials are potential game changers for these challenging separations due to their ability to provide superb size and shape discrimination; however, large-scale application of these materials has yet to be adopted. The current state of the art in the separation of similarly-sized organic molecules via microporous materials is discussed.

2.1 Introduction

The development of robust, scalable, and selective membrane materials is the critical challenge facing membrane scientists and engineers. Specifically, microporous materials—materials with pore sizes less than 2 nm—have small and (often) tunable pores that can be used to differentiate even very similarly-sized compounds. Conventional schemes for tuning the micropores typically attempt to alter the sorption capacity of the material rather than deliberately changing the diffusive properties. While synthetically simple to accomplish, this type of functionalization alone is insufficient to enable the size and shape selectivity required for challenging OSRO-type separations. Indeed, for very difficult separations, it is often necessary to limit the diffusing molecule's activated conformational state within the membrane to achieve the target separation.[1,2] Koros and coworkers introduced so-called entropic selectivity as a hallmark of rigid molecular sieving

materials.[1,2] It is responsible for the superb separation of even very similar molecules such as oxygen and nitrogen[3] or *p*-xylene and *o*-xylene.[4]

The difference in size- and shape-based selectivity (or enthalpic and entropic selectivity, respectively) for sorption-diffusion membranes is best described in terms of the transition state theory. The relationship between enthalpic and entropic selectivity can be expressed by Equation 2.1.[2] The left hand side of Equation 2.1(2.1 describes the diffusion selectivity of components *i* and *j* (the ratio of D_i and D_j) within the membrane under equivalent driving force conditions. The right hand side is the product of the respective jump lengths of components *i* and *j* within the membrane (λ_i, λ_j; often quite similar for similarly sized molecules in microporous materials and thus ~1), the enthalpic contribution based on the activation energies of diffusion ($E^*_{D,i}$, $E^*_{D,j}$) and the entropic contribution ($S^*_{D,i}$, $S^*_{D,j}$). The entropic contribution to the diffusion selectivity can be estimated through careful temperature-dependent binary diffusion measurements. Differences in guest molecule size dominate the enthalpic contribution, while the loss of vibrational and rotational modes within an ultramicropore are responsible for the entropic contribution. The concept of entropic selectivity has been investigated in detail for gas separations.[1] It is also possible that the ultramicropores in inorganic membranes such as amorphous silica[5-8] and silicon carbide[9] are able to restrict the conformational degrees of freedom of diffusing molecules, leading to the near-perfect separation of hydrogen at high temperatures. Detailed diffusion data for this class of materials will shed light on the entropic contributions to the selectivity. Importantly, entropic selectivity has essentially not been discussed in the context of organic solvent separations. Designing materials with this capability will lead to critical breakthroughs in challenging OSRO-type separations.

$$\frac{D_i}{D_j} = \left(\frac{\lambda_i^2}{\lambda_j^2}\right) exp\left[\frac{-\left(E_{D,i}^* - E_{D,j}^*\right)}{RT}\right] \cdot exp\left[\frac{S_{D,i}^* - S_{D,j}^*}{R}\right] \quad (2.1)$$

2.2 Current State of the Art

Several classes of microporous materials have been investigated for organic molecule separations and will be briefly described with emphasis on their size and shape selectivity for organic liquids, as this is a critical characteristic of materials capable of revolutionizing organic solvent separations. Although some of these materials have been studied for decades, their use for separating organic liquids remain a largely unexplored field and is ripe for reevaluation under OSRO or even OSN conditions.

2.2.1 Microporous Polymers

Microporous polymers are a growing subclass of materials within the field of polymeric membrane research.[10,11] These amorphous and often glassy polymers are characterized by their rigid backbones and poor packing efficiencies that create interconnected pore networks. High surface areas and pore volumes position microporous polymers in between conventional non-porous polymers and inorganic microporous materials. However, an important advantage of many microporous polymer systems is their solution processability, which enables scalable production of these materials into realistic membrane morphologies.[12,13] Microporous polymers have been primarily studied for gas separation applications, as the packing imperfections between the polymer chains are sufficiently selective to differentiate between similarly-sized gases.[11] For organic separations, these hydrophobic polymeric membranes have been studied for biofuel applications such as the separation of water/oxygenate mixtures via pervaporation.[14-17]

However, when moving from a sorption-driven to a diffusion-driven separation modality like OSRO, the separation performance of the membrane will likely decrease substantially.

Polymers of intrinsic microporosity (PIMs) are the most broadly studied family within microporous polymers and have been investigated for several OSN applications.[29,18,19] PIMs exhibit high organic solvent fluxes with good size-sieving rejection of larger organic solutes.[12,18] Certainly, microporous polymers exhibit very favorable OSN performance since the solute/solvent size difference is fairly substantial and the solute is generally much larger than the average pore size in the PIM network. The structures and OSN performance of several microporous polyarylate membranes are shown in Figure 2.1.[20] The polystyrene oligomer rejection performance begins to decrease as the solute size falls below 1000 g/mol and drops off significantly below 400 g/mol as it approaches the size of the solvent THF (72 g/mol).[20] Decreasing the size difference between the solute and solvent leads to less efficient size sieving and increases the importance of shape selectivity in microporous membranes. Even relatively rigid polymers in the glassy state experience increased segmental motions during solvent diffusion, and this segmental motion is expected to negate any potential entropic or shape selectivity between the diffusing molecules. This issue is further compounded in completely liquid organic systems—where the permeating solvents have been shown to swell and plasticize the membrane.[21,22] Chemical modifications such as crosslinking can help mitigate, but not completely eliminate, the associated organic solvent swelling and plasticization issues while maintaining much of the microporosity.[23-25]

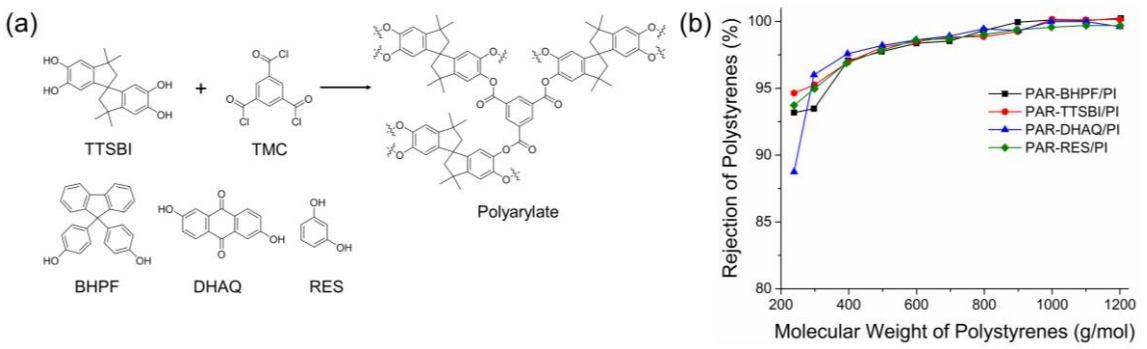

Figure 2.1 (a) Chemical structures of microporous polyarylate polymers and (b) their associated molecular weight cutoff curves for polystyrene oligomers in THF measured at 30 bar and 30°C. Adapted with permission from ref 20. Copyright 2016 Macmillan Publishers.

Current research efforts focusing on microporous polymeric membranes typically utilize large organic-soluble dyes or polymeric oligomers as proxies for larger molecules of interest in OSN.[26] While this provides a more uniform testing protocol and is less expensive than realistic solutes such as active pharmaceutical ingredients, further research utilizing more relevant feed systems is required. As the solvent system changes, it also becomes difficult to find appropriately soluble proxy molecules to characterize the membrane performance. Moreover, Livingston and coworkers have posed the "selectivity challenge" to the OSN field, which is motivated by the inability of state-of-the-art membranes to differentiate between solvents and very small solutes or even other solvents.[27] Relative to traditional non-microporous crosslinked membranes, it is not clear whether or not microporous polymers with permanent pore networks will be able to surmount this selectivity challenge. Fundamental transport measurements (e.g., temperature-dependent diffusivity) of organic solvents in crosslinked and non-crosslinked microporous polymers are needed to quantify and assess their potential for both and size and shape selectivity.

2.2.2 Metal-organic Frameworks and Covalent Organic Frameworks

Metal-organic frameworks (MOFs) are ordered microporous materials consisting of metal nodes interconnected with organic linkers. This simple design motif offers an extraordinary amount of diversity in the fabrication of new structures.[28] Different subclasses of MOFs, such as zeolitic imidazolate frameworks (ZIFs), have been extensively characterized as well.[29] As high surface area and pore volume materials, MOFs have primarily been explored for their potential as small molecule adsorbents, although they are increasingly being investigated for other applications such as membrane-based separations and catalysis.[30,31] Both supported[32] and mixed matrix[33] MOF membranes have been fabricated. The ordered and tunable pore structure of MOFs position these materials as next-generation molecular sieves, with the potential for shape selectivity to be realized.

Particularly for challenging gas separations such as olefin/paraffin, crystal engineering controls both the surface chemistry and pore size that yield high performance adsorption materials. However, these modifications focus on improving the sorption selectivity through the introduction of preferential binding sites[34] or introducing entropic effects to the sorption of specific molecules.[35,36] While showing impressive performance in sorption-dominated breakthrough experiments, it is not as clear how these materials would perform under the near-saturated conditions experienced in a liquid-phase membrane separation without further transport characterization. High performance adsorbent materials do not necessarily translate into high performance membrane materials as they are typically operated at different relative saturations in the MOF.

Although most MOFs are not water stable,[37] many are synthesized and stable in organic solvents. This organic solvent compatibility coupled with tunable pore sizes implies that MOFs are attractive candidates for challenging organic liquid separations. Indeed, ZIF-8 shows impressive diffusion selectivity for industrially-relevant hydrocarbon separations such as for *n*-hexane/3-methylpentane (~20) and 3-methylpentane/2,3-dimethylbutane (~54).[38] Importantly, MOFs and ZIFs can exhibit framework flexibility due to the influence of external stimuli and internal motions similar to the segmental motions in glassy polymers.[39] Molecular modeling work by Sholl and coworkers indicates that the effective molecular sieving window—which is larger than the nominal pore aperture—of ZIF-8 is highly influenced and can even be deformed by the sorbate molecule as shown in Figure 2.2a.[40]

This is somewhat corroborated by experimental data from Nair and coworkers that reveals a monotonic increase in activation energies of diffusion with increasing molecular diameter of the guest molecules in ZIF-8.[38] The increase starkly differs from the rigid zeolites (Figure 2.2b) and is more reminiscent of diffusion in glassy polymers where the diffusing molecule must create a "zone of activation" to make a diffusive jump.[38] Overall, framework flexibility can somewhat complicate the determination of the pore aperture—nominally determined via physisorption and diffraction measurements—and reduce the entropic selectivity of the more flexible MOFs. If the windows of ZIF materials are adapting to activated guest molecules like with glassy polymers, this suggests that ZIFs will also have the same difficulty limiting guest vibrational and rotational modes when compared to more rigid molecular sieving materials. In essence, a flexible aperture permits more conformational states of the activated molecule to pass through compared to a rigid

aperture. While framework flexibility can be beneficial for the transport of molecules larger than the nominal pore aperture, a high degree of flexibility hinders the potential for shape-based molecular separations.

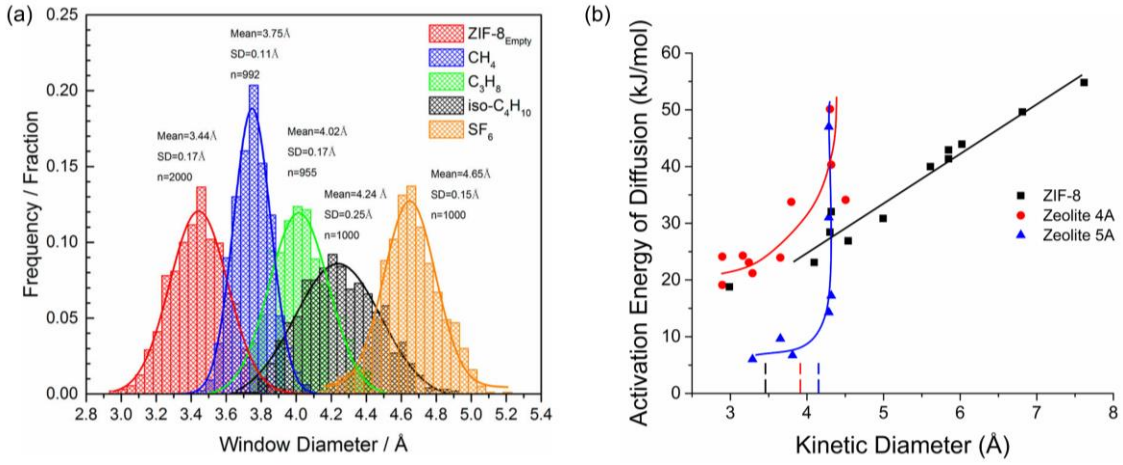

Figure 2.2 (a) ZIF-8 window size distributions at 35°C with various adsorbates positioned in the window and (b) activation energies of diffusion as a function of guest molecule kinetic diameter for ZIF-8, zeolite 4A, and zeolite 5A. Adapted with permission from refs 40 and 38. Copyright 2015 American Chemical Society.

To further illustrate the role of entropic selectivity in molecular sieving materials, Table 2.1 shows both the enthalpic and entropic contributions to the diffusion selectivity for propane and propylene in an aluminophosphate zeolite (ALPO-34, nominal pore size of 3.7 x 4.5 Å) and ZIF-8 (nominal pore size of 3.4 Å). Based on the somewhat limited literature data, we calculated the entropic contribution to the diffusion selectivity according to Equation 2.1. ALPO-34 exhibits excellent selectivity for propylene over propane (~300), with the selectivity largely amplified by the entropic contributions (entropic selectivity ~7). ZIF-8 also shows very high selectivity for propylene over propane, although the diffusion selectivity in that system is entirely dominated by enthalpic effects.[41] This indicates that

the effective molecular sieving window of ZIF-8 is near 4 Å for this system, as predicted in Figure 2.2.

Table 2.1 Enthalpic and entropic contributions to the diffusion selectivity of propane and propylene in ALPO-34 and ZIF-8.

Binary Pair (*i*/*j*)	Adsorbent	T (K)	Enthalpic Contribution	Entropic Contribution	Diffusion Selectivity (D_i/D_j)
propylene / propane	ALPO-34[a]	303	40.8	7.30	298
	ZIF-8[b]	293	138	0.68	93.3

[a]Data from ref 42.
[b]Data from ref 41.

A particularly advantageous feature of MOF and ZIF materials is the ability to fine-tune the pore aperture via the creation of hybrid or mixed linker MOFs. By controlling the relative ratio of the linkers, a variety of pore sizes can be created.[43] Detailed NMR studies combined with molecular modeling of the hybrid structures have shown that mixed linker incorporation occurs at the unit cell level, as opposed to discrete domains within the crystal.[44] These sub-Ångstrom changes to the effective pore size lead to dramatic—i.e., spanning several orders of magnitude—changes in the diffusion coefficient of gases, water, and alcohols.[45] Without temperature-dependent transport data, it is unclear if these types of modifications lead to improved entropic selectivity of the MOF—although it likely depends on the relative flexibility of the linkers involved. Different hybridization strategies have been proposed to not only change the pore size, but to change the structure of the MOF.[46] Similar strategies could be applied to larger pore MOFs to target aromatic separations.

While MOFs have a number of favorable properties for organic solvent separations, fabrication and scalability of defect-free membranes remain an ongoing challenge. Supported MOF membranes are typically brittle and prone to cracking, especially under high pressures. By growing a MOF layer partially within a polymeric support, Livingston and coworkers were able to fabricate more mechanically robust MOF thin film composite membranes for OSN.[47] This type of composite membrane formation has been demonstrated previously for a variety of other MOFs for gas separations.[48-54] The quality of the resulting membranes is highly dependent on the synthesis method and the condition of the substrate before fabrication. Functionalized surfaces and seeded growth techniques generally lead to more continuous MOF films, although concerns regarding grain boundaries and intercrystalline defects remain.[55]

Research has also been conducted on improving the scalability and the pressure resistance of MOF membranes. The interfacial microfluidic membrane processing (IMMP) approach fabricates a MOF membrane on the inside of a porous hollow fiber as shown in Figure 2.3.[48,49,56] This creates thin, yet cylindrical MOF membranes with improved pressure resistance compared to other supported flat sheet membranes.[48,49,56] Recent work utilizing carbon hollow fiber supports extends the capability of the IMMP approach to additional ZIFs requiring more extreme solvothermal synthesis conditions than those of ZIF-8.[50] While promising for the high throughput fabrication of MOF membranes, the conditions required for IMMP have yet to be proven scalable beyond the laboratory.

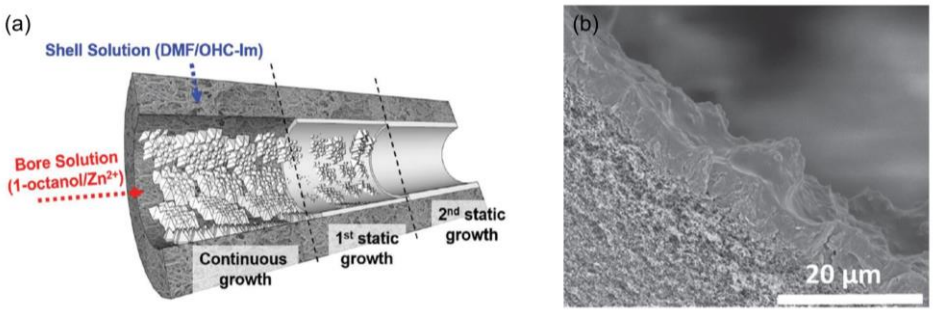

Figure 2.3 (a) Schematic of MOF formation on the bore side of a porous hollow fiber precursor using the interfacial microfluidic membrane processing (IMMP) technique. (b) SEM image of a ZIF-8 membrane grown on a Torlon® hollow fiber support. Adapted with permission from refs 50 and 49. Copyright 2016 and 2017 Wiley-VCH Verlag GmbH & Co.

The majority of MOF research tends to focus on a handful of easily synthesized and stable materials. The broad range of pore sizes available in MOFs indicates that this class of materials has significant potential for size and possibly shape selectivity of organic liquids. Less flexible or smaller pore MOFs may exhibit sharper, more selective molecular weight cutoff curves and this is an area of membrane science that is currently underdeveloped. MOF membranes for OSRO separations have not yet been investigated and will encounter mechanical challenges associated with the very high applied pressures required. Additionally, more MOFs need to be investigated to better understand the parameters with the most impact on organic solvent separations. Molecular modeling simulations of MOF interactions with small liquid organics could aid in this effort. MOFs offer an exceptional degree of flexibility in synthesizing controlled pore size materials to potentially separate a wide range of organics, although membrane fabrication remains an ongoing challenge to large-scale implementation.

Similar to MOFs, covalent organic frameworks (COFs) are another type of ordered microporous material. These structures inherently have larger pores than MOFs, in the 6-

30 Å range, due to the bond angles and sizes of the covalent linkers.[57] Studies on COFs are still in their infancy and focused on the fabrication of new COFs with primarily adsorption data available,[57] although several COF membranes have been created as well.[58-62] Proof-of-concept COF thin films have shown high rejection for large molecule dyes.[60,61] As expected of a large pore material, the molecular weight cutoff curve is not as sharp as those seen in commercial polymeric OSN membranes.[61] It is likely that COFs for OSRO separations will be more promising for the separation of fairly large organic solvents like substituted aromatics or long chain alkylates.

The short-range crystallinity of COFs does not result in brittle membranes like those made entirely from MOFs and instead these materials behave somewhat more like polymeric membranes.[60,61] While not as easily synthesized due to the nature of covalent bond formation compared to ionic bond formation in MOFs, COFs are a promising enabler for OSRO-type separations of large organic molecules.

2.2.3 Zeolites

Zeolites are ordered microporous aluminosilicate materials with well-defined pore structures and pore networks. They are the most well studied microporous material and a wealth of literature is available detailing the transport of various organic molecules in zeolite systems.[63] Due to their fairly rigid and uniform pores, zeolites are perhaps the most truly size- and shape-selective microporous material discussed here.

Zeolite membranes have primarily been studied for pervaporation and vapor separations. For example, NaA type zeolite membranes have been widely investigated for the pervaporation of water/alcohol mixtures.[64] These hydrophilic materials show very high

separation factors in alcohol dehydration separations.[64] For completely organic mixtures such as isomers, zeolites have already been shown to have some of the highest separation capabilities. MFI membranes formed from single layer nanosheets exhibit separation factors as high as almost 8000 for *p*-xylene over *o*-xylene, shown in Figure 2.4, which completely dwarf the separation factors obtainable by other membrane materials for this molecular pair.[65] Importantly, the robust chemical resistance and excellent separation performance of these membranes have resulted in continued interest in utilizing zeolites for organic separations.

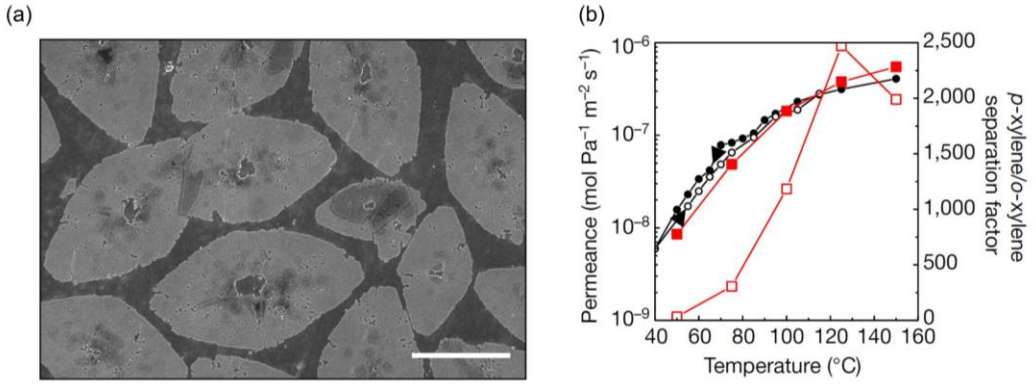

Figure 2.4 (a) SEM image of MFI nanosheets after seed removal, scale bar represents 1 µm. (b) *p*-Xylene permeance and *p*-xylene/*o*-xylene selectivity for MFI membranes measured with a Wicke-Kallenbach system. Black circles represent single component *p*-xylene permeances taken at decreasing temperature, white circles represent increasing temperature. Red squares represent *p*-xylene permeances for an equimolar *p*-xylene/*o*-xylene mixture, white squares indicate the separation factor. Adapted with permission from ref 65. Copyright 2017 Macmillan Publishers.

While the properties of zeolites as separation materials are certainly promising, there are limited zeolite structures available compared to the vast array of MOFs. Many theoretical structures have been predicted, yet it is synthetically challenging to realize most of them. As a result, research on zeolites has been primarily constrained to modifying existing zeolites. The lack of large pore zeolites becomes especially problematic when

separating molecules in the 10-20 Å range. Only a few large pore zeolites are readily available—such as the type X zeolites—for those types of separations.[66] Unlike polymeric membranes, zeolite membranes are typically tested with low concentration vapor feeds that showcase the highest possible separation performance obtainable since the penetrant concentration is dilute in the membrane.[4] However, at high feed concentrations, the zeolite pores can become saturated and the productivity of the membrane can decrease drastically.[4] The use of single layer zeolite sheets somewhat mitigates the concern regarding high sorbate loading within the pores; however, translation into large surface area membranes remains an issue.

As with MOFs and other crystalline materials, the longstanding challenge has been the fabrication of defect-free membranes at scale.[67-69] Supported zeolite membranes have been fabricated in the hollow fiber morphology with low defect concentrations.[70] Although higher pressure resistance is expected in a hollow fiber morphology compared to a flat sheet, it is likely that supported zeolite membranes will suffer the same relatively low pressure limitations as MOF membranes when challenged with typical OSRO conditions. Moreover, there is a lack of research on zeolite membranes for organic liquid separations in OSN and OSRO modalities. While presently the most well-studied and highest performing microporous material for size- and shape-selective separation of organics, zeolite materials must still overcome substantial fabrication issues to facilitate their use in challenging organic liquid separations.

2.2.4 Carbons

Carbon materials are the product of the controlled pyrolysis of an organic precursor, typically an amorphous polymer. The resulting amorphous carbon structure that is formed is comprised of sp^2 hybridized carbon sheets that pack inefficiently to create a bimodal distribution of micropores, more similar in microstructure to microporous polymers than ordered MOFs or zeolites.[1] Simpler activated carbon materials have been studied for adsorption of a variety of compounds, but the large and non-uniform pore size distribution is not advantageous for membrane applications and are certainly not shape-selective materials.[71] More advanced carbon membranes—carbon molecular sieve membranes (CMS)—have been explored and characterized for primarily gas separation applications.[72] They show very high selectivities for similar sized gas pairs[2,73] driven by entropic contributions and are promising candidate materials for organic liquid separations.[4]

While not necessarily to the same degree as zeolites, CMS membranes can exhibit both size and shape selectivity. Once carbonized, the CMS experiences significantly less swelling and plasticization due to organic solvents than their polymeric precursors; in fact, any swelling/plasticization phenomena have not been conclusively observed in the literature. The pyrolysis conditions are used to tune the membrane transport properties by controlling the final pore size, and increasing pyrolysis temperature generally tightens the pore network and decreases the average pore size.[73-76] While advantageous for gas separations, this can be challenging when utilizing these materials for larger organic liquid separations. Regardless, CMS hollow fiber membranes have been used to demonstrate the proof-of-concept molecular separation of *p*-xylene from *o*-xylene.[4] Starting from the pyrolysis of crosslinked polymeric poly(vinylidene fluoride) hollow fibers (Figure 2.5a),

these solvent-resistant CMS fibers are able to enrich an equimolar liquid feed to 81 mol% *p*-xylene at ambient temperature as shown in Figure 2.5b.[4] The CMS fibers are mechanically robust and can withstand extremely high applied pressures, over 100 bar, required to enable organic solvent reverse osmosis.[4]

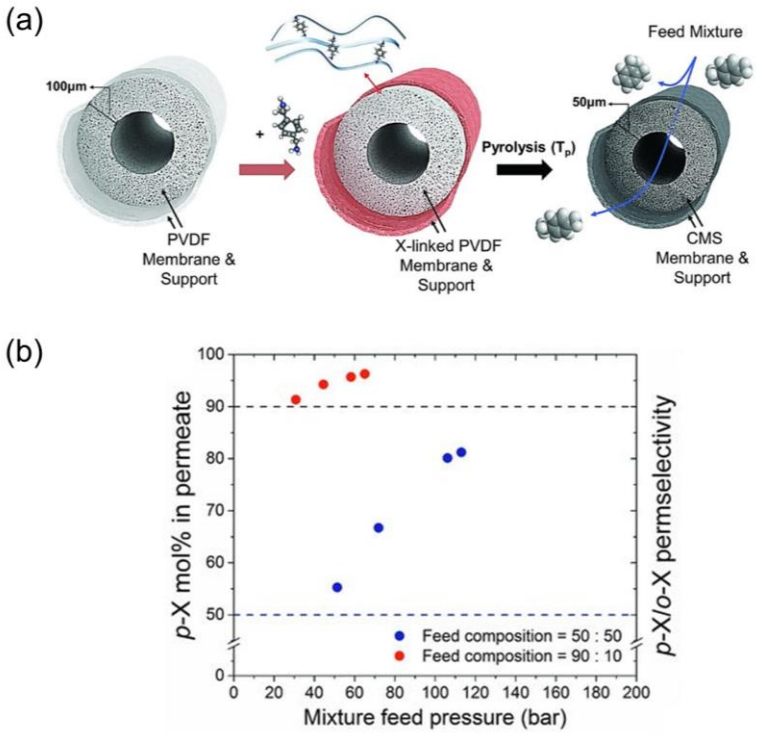

Figure 2.5 (a) Fabrication scheme of asymmetric CMS hollow fiber membranes made from PVDF. (b) Room temperature mixture permeate composition from a CMS fiber pyrolyzed at 550°C. Adapted with permission from ref 4. Copyright 2016 American Association for the Advancement of Science.

In addition to CMS, other carbon-based membranes have been fabricated as well. For example, graphene oxide membranes depend on the packing defects between the impermeable carbon sheets to achieve molecular separation.[77,78] The surface chemistry of the sheets and the interactions with the separation medium affect the interlayer spacing and thus the resulting separation performance.[77] Functionalized graphene oxide membranes

show very high solvent flux and good size rejection of large dyes molecules, although it is subject to the charge interactions between the membrane and the dye.[78] However, it is unclear how the interlayer spacing of the graphene oxide sheets change with increasing applied pressure, like those needed for OSN and OSRO separations. Due to the semi-random nature of the pore structure created by the stacked sheets, graphene and graphene oxide membranes are not likely to exhibit significant shape selectivity without additional functionalization.

Although less brittle than MOFs and zeolites, CMS are still rigid materials. Flat sheet CMS membranes experience the same limitations as supported MOF and zeolite membranes and are not highly pressure resistant. However, CMS membranes maintain the advantage of solution processability from their polymeric precursors and can be pre-fabricated into the desired membrane morphology before pyrolysis. This allows for a much simpler and more scalable fabrication than current MOF and zeolite membranes. CMS membrane fabrication scale up schemes have been discussed and demonstrated in the literature.[79]

Certainly, a more detailed understanding of the CMS formation process and the resulting structure would improve the understanding of how to further tune these materials for organic solvent separations. Methods to create CMS membranes containing pores in the 6-15 Å region are critically needed to extend OSRO-type separations to large hydrocarbon molecules. The necessity of pressure resistant hollow fiber membrane precursors hinders the study of new polymers for CMS formation when compared to similar efforts made in gas separations. The use of composite CMS structures for high throughput testing could greatly improve the utility of these materials, but requires careful

matching of thermomechanical properties. Overall, the combination of favorable aspects of polymer processing with the size and shape selectivity of rigid molecular sieving materials position CMS membranes as a promising class of materials for enabling challenging organic separations.

2.2.5 Composites

Mixed matrix membranes (MMMs) are hybrid membrane materials that combine a continuous phase (typically polymer) with a discontinuous filler (typically a microporous porous material like a MOF, zeolite, or CMS). Hybrid membranes are promising membrane systems since they combine the facile processability of polymers with the high separation performance of rigid microporous materials. MMMs for organic separations have primarily been focused around pervaporation separations.[80] In these systems, the inclusion of the filler is often used to enhance the sorption selectivity of a desired component rather than alter the diffusive selectivity.[80] Hybrid membranes have also been studied for OSN-type separations. Several methods have been developed to create different types of polymer/MOF hybrid membranes including *in situ* growth,[81] interfacial synthesis,[47] interfacial polymerization,[82] and mixed matrix membranes.[80] The inclusion of a size-selective filler tends to boost the separation performance while simultaneously increasing the permeance of the membrane compared to the base polymer.[80]

Although likely less detrimental than in gas separations, interfacial defects between the filler and the polymer matrix can negatively affect the membrane performance. Interfacial defects in MMMs tend to cause the fluid to bypass the filler while the continuous polymer phase prevents unimpeded pressure-driven flow. The fluid transport in the non-

selective voids is significantly slower for liquids compared to gases due to the differences in gas and liquid molecular diffusion coefficients. In this way, the presence of defects in MMMs is not as detrimental as for entirely MOF, zeolite, and carbon membranes—although the separation performance does indeed suffer as a result of defects. Particularly problematic for zeolite/organic polymer composites, incompatibility between the phases can create non-selective defect pathways such as the ones shown in Figure 2.6a.[83] Various methods have been devised to modify the surface of the zeolite particles to improve interfacial adhesion.[84] Even so, the use of zeolites has largely been avoided since the discovery of MOFs, primarily due to the fact that the organic linker components of MOFs greatly improve the adhesion between the two phases in composite membranes without the need for surface functionalization (Figure 2.6b).[85] Further reducing the inorganic content of the filler by utilizing COFs, improves the compatibility of the filler and the polymer even more.[86-89] Even without interfacial defects, the performance of each phase needs to be matched to one another to achieve concomitant improvement in permeance and selectivity compared to the base polymer. In addition, solvent resistance is expected to follow that of the parent polymeric material as the filler content is generally very low, which suggests that MMMs in OSN or OSRO applications may need further modification to improve the solvent resistance. This additional criteria can introduce restrictions to the choice of filler and membrane materials.

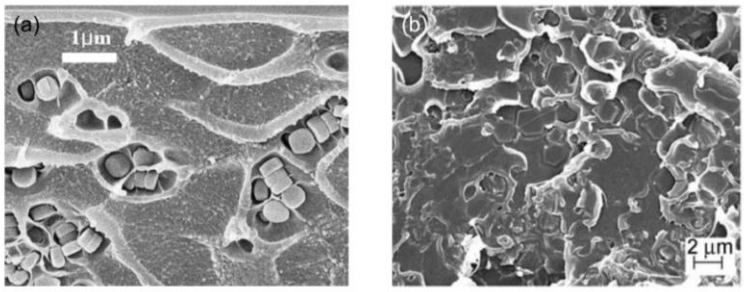

Figure 2.6 (a) Mixed matrix membrane made with 20 wt% of 300 nm unmodified pure silica MFI in Ultem®. Undesirable sieve-in-a-cage morphology is exhibited due to the poor interfacial adhesion of the zeolite and polymer. (b) Mixed matrix membrane made with 15 wt% of 800 nm ZIF-90 in Ultem®. Good filler adhesion is achieved without the need for surface modification of the MOF. Adapted with permission from refs 83 and 85. Copyright 2009 American Chemical Society and 2010 Wiley-VCH Verlag GmbH & Co.

The transport analysis of composite membranes can become quite complicated when compared to single component membranes. Many different models have been developed, typically based on the Maxwell equation, to represent the permeation of gases in various MMMs.[90-93] Information on not only the individual components permeabilities, but particle sizes, shapes, dispersion, and adhesion within the membrane for the filler are sometimes required. Using careful measurements of the MMM performance coupled with measurements of the pure continuous polymer phase, the properties of the inorganic filler can be back calculated using the appropriate permeation model. Theoretically, this type of analysis can be adapted for studying the permeation of organic liquids through MMMs after accounting for the non-idealities introduced by moving to an organic liquid systems. However, much of the fundamental transport data and modeling work associated with liquid phase organic solvent permeation in MMMs are currently lacking in the literature.

Hybrid materials are promising candidates for organic liquid separations, but more data is needed to better utilize them. Although improvements in separation performance

are reported, little transport analysis is available for these materials beyond routine permeation analysis. The combination of a fairly flexible polymer with discrete rigid fillers cannot exceed the separation capability of a purely rigid microporous material. However, other aspects besides selectivity, such as membrane processability and cost, need to be considered as well. In that regard, MMMs may find a place as a membrane material with improved separation capabilities (compared to the polymer) with simpler fabrication (compared to the filler). Selection rules for both the filler and polymer performance are needed as with MMMs for gas separations. The transport mechanism for organic liquids is not yet fully understood for these systems as well. While it is reasonable to expect the enthalpic selectivity contributions of the filler to positively influence the resulting composite performance, the role of entropy selectivity of the filler is more ambiguous.

2.3 Defects

As with all membrane-based applications, controlling defects is a critical issue. Defects, especially in OSRO applications with low driving forces for defect-free transport, can severely compromise the membrane's performance by allowing non-selective transport pathways to dominate. Methods have been developed to address defects in a variety of membranes and membrane materials, although polymeric membrane systems are the most common. Many of these methods originated from defect treatments for gas or water separation membranes. While conceptually similar, special care must be taken when directly translating these methods for use with organic solvents due to the potential for strong and non-ideal interactions between the defect treatment and the solvent.

One of the most common methods to address defects in both flexible and brittle membranes is via the formation of composite membrane structures. An additional layer—typically a highly permeable polymer layer such as poly(dimethylsiloxane) (PDMS)—is coated on top of the selective membrane layer to seal defects and protect the membrane.[94] This top layer effectively blocks unimpeded transport through defects while adding minimal resistance to the selective layer. Other layers can also be added to the composite structure to improve the adhesion and compatibility of the different layers.[94] Directly utilizing PDMS-coated membranes for organic solvent applications is not particularly feasible due to the propensity for PDMS to swell in many organic solvents. Significant swelling of a composite layer inside a defect could further damage brittle membranes and worsen the separation performance. Utilizing more solvent-resistant, yet highly permeable polymers as top layers should achieve the same effect as PDMS-coated gas separation membranes, although this has not been explored in detail. Especially for polymeric membranes that can swell significantly in organic solvents, choosing a top layer with a similar degree of swelling is critical to prevent delamination of the different layers.

Thermal annealing is another common technique to improve polymeric membrane performance. The membrane is heated to near its glass transition temperature to impart a small degree of polymer chain mobility, decrease the free volume, and promote other changes to the material.[95,96] While useful for many polymer systems, thermal annealing is not applicable to some of the more rigid polymers without glass transition temperatures or the more crystalline materials previously discussed.

Finally, interfacially polymerized membranes have the advantage of healing defects as they appear during membrane formation. Monomers dissolved in two immiscible layers

meet and form a thin and self-limiting polymer at the interface. Originally developed for polymeric membranes,[97] similar techniques have been adopted for the interfacial fabrication of MOFs[48,98] and composites.[99] However, not all of the microporous materials discussed here are amenable to formation via interfacial polymerization or other interfacial synthesis techniques. As with all additional layers to the membrane, the solvent stability, flux, and adhesion to the original membrane are key parameters to consider for OSRO.

Other methods to address specific types of defects in MOFs[98] and zeolites[67] have been discussed in the literature. These defect treatments tend to be less broadly applicable across all the membrane types discussed here (e.g., removal of grain boundaries) but are still instructive for improving the separation performance of specific classes of membranes.

2.4 Conclusions

Organic solvent separations are an emerging field within membrane technology with the potential to enable energy-efficient separation processes. Utilization of fundamental knowledge gained over the last 50 to 60 years from industrial gas and water separation membranes should enable rapid development in this area. While many challenges in the field remain, the positive potential of this technology spans a wide application space and there is significant room for the study of new systems and new methodologies that relate broadly to organic solvent separations. Indeed, this is far from a saturated field of study and many targets can be envisioned including developing platform microporous materials, creating meaningful membrane areas and form factors, defining critical separation targets for the field, understanding the role of enthalpic/entropic selectivities in large molecule separations, and addressing the role of defects and defect

formation fundamentals. Organic solvent separations could potentially revolutionize separations technology and enable lower energy, lower carbon emission separations, and potentially lead to commercial products not yet possible with conventional technologies. However, game-changing breakthroughs in material performance coupled with scalable and relatively low-cost membrane fabrication techniques are required. Moreover, robust and reliable membrane devices are needed to garner industrial attention. The economic benefits of membrane separations need to drive the adaptation of the technology rather than relying on meeting regulatory needs alone; indeed, one path forward is for membrane separation processes to open up pathways to new products like biofuels not currently available with existing separation technologies. The strong foundation established by scientists and engineers working in the gas and water separation areas, combined with a surge in acceptance of membrane systems by industry in these application spaces, strongly suggests that the future for membrane-based organic solvent separations is bright.

2.5 REFERENCES

(1) Koros, W. J.; Zhang, C. Materials for next-generation molecularly selective synthetic membranes. *Nat. Mater*. **2017**, *16*, 289-297.

(2) Singh, A.; Koros, W. J. Significance of Entropic Selectivity for Advanced Gas Separation Membranes. *Ind. Eng. Chem. Res*. **1996**, *35*, 1231-1234.

(3) Zimmerman, C. M.; Koros, W. J. Entropic Selectivity Analysis of a Series of Polypyrrolones for Gas Separation Membranes. *Macromolecules* **1999**, *32*, 3341-3346.

(4) Koh, D.-Y.; McCool, B. A.; Deckman, H. W.; Lively, R. P. Reverse osmosis molecular differentiation of organic liquids using carbon molecular sieve membranes. *Science* **2016**, *353*, 804-807.

(5) Prabhu, A. K.; Oyama, S. T. Highly hydrogen selective ceramic membranes: application to the transformation of greenhouse gases. *J. Membrane Sci*. **2000**, *176*, 233-248.

(6) Lee, D.; Oyama, S. T. Gas permeation characteristics of a hydrogen selective supported silica membrane. *J. Membrane Sci*. **2002**, *210*, 291-306.

(7) Gavalas, G. R.; Megiris, C. E.; Nam, S. W., Deposition of H_2-permselective SiO_2 films. *Chem. Eng. Sci*. **1989**, *44*, 1829-1835.

(8) Kim, S.; Gavalas, G. R. Preparation of H2 Permselective Silica Membranes by Alternating Reactant Vapor Deposition. *Ind. Eng. Chem. Res*. **1995**, *34*, 168-176.

(9) Elyassi, B.; Sahimi, M.; Tsotsis, T. T. Silicon carbide membranes for gas separation applications. *J. Membrane Sci*. **2007**, *288*, 290-297.

(10) McKeown, N. B.; Budd, P. M. Polymers of intrinsic microporosity (PIMs): organic materials for membrane separations, heterogeneous catalysis and hydrogen storage. *Chem. Soc. Rev*. **2006**, *35*, 675-683.

(11) Kim, S.; Lee, Y. M. Rigid and microporous polymers for gas separation membranes. *Prog. Polym. Sci*. **2015**, *43*, 1-32.

(12) Fritsch, D.; Merten, P.; Heinrich, K.; Lazar, M.; Priske, M. High performance organic solvent nanofiltration membranes: Development and thorough testing of thin film composite membranes made of polymers of intrinsic microporosity (PIMs). *J. Membrane Sci*. **2012**, *401–402*, 222-231.

(13) Jue, M. L.; Breedveld, V.; Lively, R. P. Defect-free PIM-1 hollow fiber membranes. *J. Membrane Sci*. **2017**, *530*, 33-41.

(14) Adymkanov, S. V.; Yampol'skii, Y. P.; Polyakov, A. M.; Budd, P. M.; Reynolds, K. J.; McKeown, N. B.; Msayib, K. J. Pervaporation of alcohols through highly permeable PIM-1 polymer films. *Polym. Sci. Ser. A+* **2008**, *50*, 444-450.

(15) Žák, M.; Klepic, M.; Štastná, L. Č.; Sedláková, Z.; Vychodilová, H.; Hovorka, Š.; Friess, K.; Randová, A.; Brožová, L.; Jansen, J. C.; Khdhayyer, M. R.; Budd, P. M.; Izák, P. Selective removal of butanol from aqueous solution by pervaporation with a PIM-1 membrane and membrane aging. *Sep. Purif. Technol*. **2015**, *151*, 108-114.

(16) Budd, P. M.; Elabas, E. S.; Ghanem, B. S.; Makhseed, S.; McKeown, N. B.; Msayib, K. J.; Tattershall, C. E.; Wang, D. Solution-Processed, Organophilic Membrane Derived from a Polymer of Intrinsic Microporosity. *Adv. Mater*. **2004**, *16*, 456-459.

(17) Wu, X. M.; Zhang, Q. G.; Soyekwo, F.; Liu, Q. L.; Zhu, A. M. Pervaporation removal of volatile organic compounds from aqueous solutions using the highly permeable PIM-1 membrane. *AIChE J*. **2016**, *62*, 842-851.

(18) Gorgojo, P.; Karan, S.; Wong, H. C.; Jimenez-Solomon, M. F.; Cabral, J. T.; Livingston, A. G. Ultrathin Polymer Films with Intrinsic Microporosity: Anomalous Solvent Permeation and High Flux Membranes. *Adv. Funct. Mater*. **2014**, *24*, 4729-4737.

(19) Tsarkov, S.; Khotimskiy, V.; Budd, P. M.; Volkov, V.; Kukushkina, J.; Volkov, A. Solvent nanofiltration through high permeability glassy polymers: Effect of polymer and solute nature. *J. Membrane Sci*. **2012**, *423–424*, 65-72.

(20) Jimenez-Solomon, M. F.; Song, Q.; Jelfs, K. E.; Munoz-Ibanez, M.; Livingston, A. G. Polymer nanofilms with enhanced microporosity by interfacial polymerization. *Nat. Mater*. **2016**, *15*, 760-767.

(21) Jue, M. L.; McKay, C. S.; McCool, B. A.; Finn, M. G.; Lively, R. P. Effect of Nonsolvent Treatments on the Microstructure of PIM-1. *Macromolecules* **2015**, *48*, 5780-5790.

(22) Ogieglo, W.; Ghanem, B.; Ma, X.; Pinnau, I.; Wessling, M. How Much Do Ultrathin Polymers with Intrinsic Microporosity Swell in Liquids? *J. Phys. Chem. B* **2016**, *120*, 10403-10410.

(23) Du, N.; Cin, M. M. D.; Pinnau, I.; Nicalek, A.; Robertson, G. P.; Guiver, M. D. Azide-based Cross-Linking of Polymers of Intrinsic Microporosity (PIMs) for Condensable Gas Separation. *Macromol. Rapid Comm*. **2011**, *32*, 631-636.

(24) Du, N.; Dal-Cin, M. M.; Robertson, G. P.; Guiver, M. D., Decarboxylation-Induced Cross-Linking of Polymers of Intrinsic Microporosity (PIMs) for Membrane Gas Separation. *Macromolecules* **2012**, *45*, 5134-5139.

(25) Song, Q.; Cao, S.; Pritchard, R. H.; Ghalei, B.; Al-Muhtaseb, S. A.; Terentjev, E. M.; Cheetham, A. K.; Sivaniah, E. Controlled thermal oxidative crosslinking of polymers of intrinsic microporosity towards tunable molecular sieve membranes. *Nat. Commun*. **2014**, *5*.

(26) Marchetti, P.; Jimenez Solomon, M. F.; Szekely, G.; Livingston, A. G. Molecular Separation with Organic Solvent Nanofiltration: A Critical Review. *Chem. Rev*. **2014**, *114*, 10735-10806.

(27) Marchetti, P.; Peeva, L.; Livingston, A. The Selectivity Challenge in Organic Solvent Nanofiltration: Membrane and Process Solutions. *Annu. Rev. Chem. Biomol*. **2017**, *8*, 473-497.

(28) Chung, Y. G.; Camp, J.; Haranczyk, M.; Sikora, B. J.; Bury, W.; Krungleviciute, V.; Yildirim, T.; Farha, O. K.; Sholl, D. S.; Snurr, R. Q. Computation-Ready, Experimental Metal–Organic Frameworks: A Tool To Enable High-Throughput Screening of Nanoporous Crystals. *Chem. Mater*. **2014**, *26*, 6185-6192.

(29) Pimentel, B. R.; Parulkar, A.; Zhou, E.-k.; Brunelli, N. A.; Lively, R. P. Zeolitic Imidazolate Frameworks: Next-Generation Materials for Energy-Efficient Gas Separations. *ChemSusChem* **2014**, *7*, 3202-3240.

(30) Adil, K.; Belmabkhout, Y.; Pillai, R. S.; Cadiau, A.; Bhatt, P. M.; Assen, A. H.; Maurin, G.; Eddaoudi, M. Gas/vapour separation using ultra-microporous metal-organic frameworks: insights into the structure/separation relationship. *Chem. Soc. Rev*. **2017**, *46*, 3402-3430.

(31) Kuppler, R. J.; Timmons, D. J.; Fang, Q.-R.; Li, J.-R.; Makal, T. A.; Young, M. D.; Yuan, D.; Zhao, D.; Zhuang, W.; Zhou, H.-C. Potential applications of metal-organic frameworks. *Coordin. Chem. Rev*. **2009**, *253*, 3042-3066.

(32) Shekhah, O.; Liu, J.; Fischer, R. A.; Woll, C. MOF thin films: existing and future applications. *Chem. Soc. Rev*. **2011**, *40*, 1081-1106.

(33) Zornoza, B.; Tellez, C.; Coronas, J.; Gascon, J.; Kapteijn, F. Metal organic framework based mixed matrix membranes: An increasingly important field of research with a large application potential. *Micropor. Mesopor. Mat*. **2013**, *166*, 67-78.

(34) Cui, X.; Chen, K.; Xing, H.; Yang, Q.; Krishna, R.; Bao, Z.; Wu, H.; Zhou, W.; Dong, X.; Han, Y.; Li, B.; Ren, Q.; Zaworotko, M. J.; Chen, B. Pore chemistry and size control in hybrid porous materials for acetylene capture from ethylene. *Science* **2016**, *353*, 141-144.

(35) Herm, Z. R.; Wiers, B. M.; Mason, J. A.; van Baten, J. M.; Hudson, M. R.; Zajdel, P.; Brown, C. M.; Masciocchi, N.; Krishna, R.; Long, J. R. Separation of Hexane Isomers in a Metal-Organic Framework with Triangular Channels. *Science* **2013**, *340*, 960-964.

(36) Cadiau, A.; Adil, K.; Bhatt, P. M.; Belmabkhout, Y.; Eddaoudi, M. A metal-organic framework–based splitter for separating propylene from propane. *Science* **2016**, *353*, 137-140.

(37) Burtch, N. C.; Jasuja, H.; Walton, K. S. Water Stability and Adsorption in Metal–Organic Frameworks. *Chem. Rev*. **2014**, *114*, 10575-10612.

(38) Zhang, K.; Lively, R. P.; Zhang, C.; Chance, R. R.; Koros, W. J.; Sholl, D. S.; Nair, S. Exploring the Framework Hydrophobicity and Flexibility of ZIF-8: From Biofuel Recovery to Hydrocarbon Separations. *J. Phys. Chem. Lett*. **2013**, *4*, 3618-3622.

(39) Coudert, F.-X.; Boutin, A.; Jeffroy, M.; Mellot-Draznieks, C.; Fuchs, A. H. Thermodynamic Methods and Models to Study Flexible Metal–Organic Frameworks. *ChemPhysChem* **2011**, *12*, 247-258.

(40) Verploegh, R. J.; Nair, S.; Sholl, D. S. Temperature and Loading-Dependent Diffusion of Light Hydrocarbons in ZIF-8 as Predicted Through Fully Flexible Molecular Simulations. *J. Am. Chem. Soc*. **2015**, *137*, 15760-15771.

(41) Pimentel, B. R.; Lively, R. P. Enabling Kinetic Light Hydrocarbon Separation via Crystal Size Engineering of ZIF-8. *Ind. Eng. Chem. Res*. **2016**, *55*, 12467-12476.

(42) Ruthven, D. M.; Reyes, S. C. Adsorptive separation of light olefins from paraffins. *Micropor. Mesopor. Mat*. **2007**, *104*, 59-66.

(43) Thompson, J. A.; Blad, C. R.; Brunelli, N. A.; Lydon, M. E.; Lively, R. P.; Jones, C. W.; Nair, S. Hybrid Zeolitic Imidazolate Frameworks: Controlling Framework Porosity and Functionality by Mixed-Linker Synthesis. *Chem. Mater*. **2012**, *24*, 1930-1936.

(44) Jayachandrababu, K. C.; Verploegh, R. J.; Leisen, J.; Nieuwendaal, R. C.; Sholl, D. S.; Nair, S. Structure Elucidation of Mixed-Linker Zeolitic Imidazolate Frameworks by Solid-State 1H CRAMPS NMR Spectroscopy and Computational Modeling. *J. Am. Chem. Soc*. **2016**, *138*, 7325-7336.

(45) Eum, K.; Jayachandrababu, K. C.; Rashidi, F.; Zhang, K.; Leisen, J.; Graham, S.; Lively, R. P.; Chance, R. R.; Sholl, D. S.; Jones, C. W.; Nair, S. Highly Tunable Molecular Sieving and Adsorption Properties of Mixed-Linker Zeolitic Imidazolate Frameworks. *J. Am. Chem. Soc*. **2015**, *137*, 4191-4197.

(46) Bunck, D. N.; Dichtel, W. R. Mixed Linker Strategies for Organic Framework Functionalization. *Chem. Eur. J*. **2013**, *19*, 818-827.

(47) Campbell, J.; Davies, R. P.; Braddock, D. C.; Livingston, A. G. Improving the permeance of hybrid polymer/metal-organic framework (MOF) membranes for organic solvent nanofiltration (OSN) - development of MOF thin films via interfacial synthesis. *J. Mater. Chem. A* **2015**, *3*, 9668-9674.

(48) Brown, A. J.; Brunelli, N. A.; Eum, K.; Rashidi, F.; Johnson, J. R.; Koros, W. J.; Jones, C. W.; Nair, S. Interfacial microfluidic processing of metal-organic framework hollow fiber membranes. *Science* **2014**, *345*, 72-75.

(49) Eum, K.; Rownaghi, A.; Choi, D.; Bhave, R. R.; Jones, C. W.; Nair, S. Fluidic Processing of High-Performance ZIF-8 Membranes on Polymeric Hollow Fibers: Mechanistic Insights and Microstructure Control. *Adv. Funct. Mater*. **2016**, *26*, 5011-5018.

(50) Eum, K.; Ma, C.; Koh, D.-Y.; Rashidi, F.; Li, Z.; Jones, C. W.; Lively, R. P.; Nair, S. Zeolitic Imidazolate Framework Membranes Supported on Macroporous Carbon Hollow Fibers by Fluidic Processing Techniques. *Adv. Mater. Interfaces* **2017**, *4*, 1700080.

(51) Arnold, M.; Kortunov, P.; Jones, D. J.; Nedellec, Y.; Kärger, J.; Caro, J. Oriented Crystallisation on Supports and Anisotropic Mass Transport of the Metal-Organic Framework Manganese Formate. *Eur. J. Inorg. Chem*. **2007**, *2007*, 60-64.

(52) Yao, J.; Dong, D.; Li, D.; He, L.; Xu, G.; Wang, H. Contra-diffusion synthesis of ZIF-8 films on a polymer substrate. *Chem. Commun*. **2011**, *47*, 2559-2561.

(53) Liu, Y.; Ng, Z.; Khan, E. A.; Jeong, H.-K.; Ching, C.-b.; Lai, Z. Synthesis of continuous MOF-5 membranes on porous α-alumina substrates. *Micropor. Mesopor. Mat*. **2009**, *118*, 296-301.

(54) McCarthy, M. C.; Varela-Guerrero, V.; Barnett, G. V.; Jeong, H.-K. Synthesis of Zeolitic Imidazolate Framework Films and Membranes with Controlled Microstructures. *Langmuir* **2010**, *26*, 14636-14641.

(55) Stock, N.; Biswas, S. Synthesis of Metal-Organic Frameworks (MOFs): Routes to Various MOF Topologies, Morphologies, and Composites. *Chem. Rev*. **2012**, *112*, 933-969.

(56) Eum, K.; Ma, C.; Rownaghi, A.; Jones, C. W.; Nair, S. ZIF-8 Membranes via Interfacial Microfluidic Processing in Polymeric Hollow Fibers: Efficient Propylene Separation at Elevated Pressures. *ACS Appl. Mater. Inter*. **2016**, *8*, 25337-25342.

(57) Ding, S.-Y.; Wang, W. Covalent organic frameworks (COFs): from design to applications. *Chem. Soc. Rev*. **2013**, *42*, 548-568.

(58) Hao, D.; Zhang, J.; Lu, H.; Leng, W.; Ge, R.; Dai, X.; Gao, Y. Fabrication of a COF-5 membrane on a functionalized α-Al_2O_3 ceramic support using a microwave irradiation method. *Chem. Commun*. **2014**, *50*, 1462-1464.

(59) Lu, H.; Wang, C.; Chen, J.; Ge, R.; Leng, W.; Dong, B.; Huang, J.; Gao, Y. A novel 3D covalent organic framework membrane grown on a porous α-Al_2O_3 substrate under solvothermal conditions. *Chem. Commun*. **2015**, *51*, 15562-15565.

(60) Dey, K.; Pal, M.; Rout, K. C.; Kunjattu H, S.; Das, A.; Mukherjee, R.; Kharul, U. K.; Banerjee, R. Selective Molecular Separation by Interfacially Crystallized Covalent Organic Framework Thin Films. *J. Am. Chem. Soc*. **2017**, *139*, 13083-13091.

(61) Kandambeth, S.; Biswal, B. P.; Chaudhari, H. D.; Rout, K. C.; Kunjattu H, S.; Mitra, S.; Karak, S.; Das, A.; Mukherjee, R.; Kharul, U. K.; Banerjee, R. Selective Molecular Sieving in Self-Standing Porous Covalent-Organic-Framework Membranes. *Adv. Mater*. **2017**, *29*, 1603945.

(62) Li, G.; Zhang, K.; Tsuru, T. Two-Dimensional Covalent Organic Framework (COF) Membranes Fabricated via the Assembly of Exfoliated COF Nanosheets. *ACS Appl. Mater. Inter*. **2017**, *9*, 8433-8436.

(63) Keil Frerich, J.; Krishna, R.; Coppens, M.-O. Modeling of Diffusion in Zeolites. Rev. *Chem. Eng*. **2000**, *16*, 71-197.

(64) Wee, S.-L.; Tye, C.-T.; Bhatia, S. Membrane separation process—Pervaporation through zeolite membrane. *Sep. Purif. Technol*. **2008**, *63*, 500-516.

(65) Jeon, M. Y.; Kim, D.; Kumar, P.; Lee, P. S.; Rangnekar, N.; Bai, P.; Shete, M.; Elyassi, B.; Lee, H. S.; Narasimharao, K.; Basahel, S. N.; Al-Thabaiti, S.; Xu, W.; Cho, H. J.; Fetisov, E. O.; Thyagarajan, R.; DeJaco, R. F.; Fan, W.; Mkhoyan, K. A.; Siepmann, J. I.; Tsapatsis, M. Ultra-selective high-flux membranes from directly synthesized zeolite nanosheets. *Nature* **2017**, *543*, 690-694.

(66) Baerlocher, C.; McCusker, L. B.; Olson, D. H. *Atlas of zeolite framework types*; Elsevier. B. V.: Amsterdam, The Netherlands, 2007.

(67) Rangnekar, N.; Mittal, N.; Elyassi, B.; Caro, J.; Tsapatsis, M. Zeolite membranes - a review and comparison with MOFs. *Chem. Soc. Rev*. **2015**, *44*, 7128-7154.

(68) Gascon, J.; Kapteijn, F.; Zornoza, B.; Sebastián, V.; Casado, C.; Coronas, J. Practical Approach to Zeolitic Membranes and Coatings: State of the Art, Opportunities, Barriers, and Future Perspectives. *Chem. Mater*. **2012**, *24*, 2829-2844.

(69) Caro, J.; Noack, M.; Kölsch, P.; Schäfer, R. Zeolite membranes – state of their development and perspective. *Micropor. Mesopor. Mat.* **2000**, *38*, 3-24.

(70) Ge, Q.; Wang, Z.; Yan, Y. High-Performance Zeolite NaA Membranes on Polymer−Zeolite Composite Hollow Fiber Supports. *J. Am. Chem. Soc.* **2009**, *131*, 17056-17057.

(71) Dąbrowski, A.; Podkościelny, P.; Hubicki, Z.; Barczak, M. Adsorption of phenolic compounds by activated carbon—a critical review. *Chemosphere* **2005**, *58*, 1049-1070.

(72) Ismail, A. F.; David, L. I. B. A review on the latest development of carbon membranes for gas separation. *J. Membrane Sci*. **2001**, *193*, 1-18.

(73) Zhang, C.; Koros, W. J. Ultraselective Carbon Molecular Sieve Membranes with Tailored Synergistic Sorption Selective Properties. *Adv. Mater*. **2017**, *29*, 1701631.

(74) Geiszler, V. C.; Koros, W. J. Effects of Polyimide Pyrolysis Conditions on Carbon Molecular Sieve Membrane Properties. *Ind. Eng. Chem. Res*. **1996**, *35*, 2999-3003.

(75) Kiyono, M.; Williams, P. J.; Koros, W. J. Effect of pyrolysis atmosphere on separation performance of carbon molecular sieve membranes. *J. Membrane Sci*. **2010**, *359*, 2-10.

(76) Fu, S.; Wenz, G. B.; Sanders, E. S.; Kulkarni, S. S.; Qiu, W.; Ma, C.; Koros, W. J. Effects of pyrolysis conditions on gas separation properties of 6FDA/DETDA:DABA(3:2) derived carbon molecular sieve membranes. *J. Membrane Sci*. **2016**, *520*, 699-711.

(77) Huang, L.; Li, Y.; Zhou, Q.; Yuan, W.; Shi, G. Graphene Oxide Membranes with Tunable Semipermeability in Organic Solvents. *Adv. Mater*. **2015**, *27*, 3797-3802.

(78) Huang, L.; Chen, J.; Gao, T.; Zhang, M.; Li, Y.; Dai, L.; Qu, L.; Shi, G. Reduced Graphene Oxide Membranes for Ultrafast Organic Solvent Nanofiltration. *Adv. Mater*. **2016**, *28*, 8669-8674.

(79) Karvan, O.; Johnson, J. R.; Williams, P. J.; Koros, W. J. A Pilot-Scale System for Carbon Molecular Sieve Hollow Fiber Membrane Manufacturing. *Chem. Eng. Technol*. **2013**, *36*, 53-61.

(80) Jia, Z.; Wu, G. Metal-organic frameworks based mixed matrix membranes for pervaporation. *Micropor. Mesopor. Mat.* **2016**, *235*, 151-159.

(81) Campbell, J.; Burgal, J. D. S.; Szekely, G.; Davies, R. P.; Braddock, D. C.; Livingston, A. Hybrid polymer/MOF membranes for Organic Solvent Nanofiltration (OSN): Chemical modification and the quest for perfection. *J. Membrane Sci*. **2016**, *503*, 166-176.

(82) Van Goethem, C.; Verbeke, R.; Hermans, S.; Bernstein, R.; Vankelecom, I. F. J. Controlled positioning of MOFs in interfacially polymerized thin-film nanocomposites. *J. Mater. Chem. A* **2016**, *4*, 16368-16376.

(83) Bae, T.-H.; Liu, J.; Lee, J. S.; Koros, W. J.; Jones, C. W.; Nair, S. Facile High-Yield Solvothermal Deposition of Inorganic Nanostructures on Zeolite Crystals for Mixed Matrix Membrane Fabrication. *J. Am. Chem. Soc*. **2009**, *131*, 14662-14663.

(84) Bastani, D.; Esmaeili, N.; Asadollahi, M. Polymeric mixed matrix membranes containing zeolites as a filler for gas separation applications: A review. *J. Ind. Eng. Chem*. **2013**, *19*, 375-393.

(85) Bae, T.-H.; Lee, J. S.; Qiu, W.; Koros, W. J.; Jones, C. W.; Nair, S. A High-Performance Gas-Separation Membrane Containing Submicrometer-Sized Metal–Organic Framework Crystals. *Angew. Chem. Int. Edit*. **2010**, *49*, 9863-9866.

(86) Zou, C.; Li, Q.; Hua, Y.; Zhou, B.; Duan, J.; Jin, W. Mechanical Synthesis of COF Nanosheet Cluster and Its Mixed Matrix Membrane for Efficient CO_2 Removal. *ACS Appl. Mater. Inter*. **2017**, *9*, 29093-29100.

(87) Cao, X.; Qiao, Z.; Wang, Z.; Zhao, S.; Li, P.; Wang, J.; Wang, S. Enhanced performance of mixed matrix membrane by incorporating a highly compatible covalent organic framework into poly(vinylamine) for hydrogen purification. *Int. J. Hydrogen Energ*. **2016**, *41*, 9167-9174.

(88) Meng, L.; Zou, X.; Guo, S.; Ma, H.; Zhao, Y.; Zhu, G. Self-Supported Fibrous Porous Aromatic Membranes for Efficient CO_2/N_2 Separations. *ACS Appl. Mater. Inter*. **2015**, *7*, 15561-15569.

(89) Shan, M.; Seoane, B.; Rozhko, E.; Dikhtiarenko, A.; Clet, G.; Kapteijn, F.; Gascon, J. Azine-Linked Covalent Organic Framework (COF)-Based Mixed-Matrix Membranes for CO_2/CH_4 Separation. *Chem. Eur. J*. **2016**, *22*, 14467-14470.

(90) Vinh-Thang, H.; Kaliaguine, S. Predictive Models for Mixed-Matrix Membrane Performance: A Review. *Chem. Rev*. **2013**, *113*, 4980-5028.

(91) Sheffel, J. A.; Tsapatsis, M. A model for the performance of microporous mixed matrix membranes with oriented selective flakes. *J. Membrane Sci*. **2007**, *295*, 50-70.

(92) Hashemifard, S. A.; Ismail, A. F.; Matsuura, T. Prediction of gas permeability in mixed matrix membranes using theoretical models. *J. Membrane Sci*. **2010**, *347*, 53-61.

(93) Petropoulos, J. H.; Papadokostaki, K. G.; Minelli, M.; Doghieri, F. On the role of diffusivity ratio and partition coefficient in diffusional molecular transport in binary composite materials, with special reference to the Maxwell equation. *J. Membrane Sci*. **2014**, *456*, 162-166.

(94) Baker, R. W. Future Directions of Membrane Gas Separation Technology. *Ind. Eng. Chem. Res*. **2002**, *41*, 1393-1411.

(95) Zhou, F.; Koros, W. J. Study of thermal annealing on Matrimid® fiber performance in pervaporation of acetic acid and water mixtures. *Polymer* **2006**, *47*, 280-288.

(96) Swaidan, R.; Ghanem, B.; Litwiller, E.; Pinnau, I. Effects of hydroxyl-functionalization and sub-T_g thermal annealing on high pressure pure- and mixed-gas CO_2/CH_4 separation by polyimide membranes based on 6FDA and triptycene-containing dianhydrides. *J. Membrane Sci*. **2015**, *475*, 571-581.

(97) Lee, K. P.; Arnot, T. C.; Mattia, D. A review of reverse osmosis membrane materials for desalination—Development to date and future potential. *J. Membrane Sci*. **2011**, *370*, 1-22.

(98) Shah, M.; McCarthy, M. C.; Sachdeva, S.; Lee, A. K.; Jeong, H.-K. Current Status of Metal–Organic Framework Membranes for Gas Separations: Promises and Challenges. *Ind. Eng. Chem. Res*. **2012**, *51*, 2179-2199.

(99) Lau, W. J.; Ismail, A. F.; Misdan, N.; Kassim, M. A. A recent progress in thin film composite membrane: A review. *Desalination* **2012**, *287*, 190-199.

CHAPTER 3. TRANSPORT AND ANALYSIS IN MEMBRANES

The theory and methods to analyze the sorption, diffusion, and permeation of gases, organic vapors, and organic liquids in polymeric and carbon membranes are discussed in detail. Both ideal and non-ideal transport mechanisms are addressed.

Parts of this chapter are adapted from 'Jue, M. L.; Lively, R. P. Targeted gas separations through polymer membrane functionalization. *React. Funct. Polym.* **2015**, *86*, 88-110.' with permission of Elsevier B. V., from 'Jue, M. L.; McKay, C. S.; McCool, B. A.; Finn, M. G.; Lively, R. P. Effect of Nonsolvent Treatments on the Microstructure of PIM-1. *Macromolecules* **2015**, *48*, 5780-5790.' with permission of the American Chemical Society, and from 'Jue, M. L.; Breedveld, V.; Lively, R. P. Defect-free PIM-1 hollow fiber membranes. *J. Polym. Sci.* **2017**, *530*, 33-41.' with permission of Elsevier B. V.

3.1 Gas Transport in Polymeric Membranes

It is useful to first review the fundamentals of gas transport in polymeric membranes, as this is a launching point for the complexities associated with organic solvent transport in membrane materials. Membranes utilized for gas separations differ from ultrafiltration (UF), nanofiltration (NF), and aqueous reverse osmosis (RO) membranes for a variety of reasons. In gas separations, not only are the sizes of the molecules being separated small, but the size differences are also less pronounced. A few tenths of Ångstrom differences are common for industrially relevant gas pairs. Table 3.1 lists the kinetic diameters of several commonly separated light gases. For instance, the separation of O_2 and N_2 from air is based on a size difference of just 0.18 Å between the two

molecules. Such a narrow size separation is challenging, especially from a materials development standpoint; even nanometer sized defects could compromise a membrane's performance. Defect free membranes are essential to enable effective separation processes.

Table 3.1 Kinetic diameters and boiling points of industrially relevant gases.

Gas	He	H_2	O_2	N_2	CO_2	CH_4
Kinetic Diameter (Å)	2.60	2.89	3.46	3.64	3.30	3.80
Boiling Point (K)	4.23	20.37	90.25	77.36	194.7	111.66

Membrane performance is described in terms of gas permeability and selectivity, with these metrics commonly used to compare different membranes. The flux through dense polymers follows Fick's first law of diffusion where penetrant gases move through the membrane down a chemical potential gradient that can be expressed in terms of fugacity, pressure, or concentration. The permeability, *P*, of a gas in a membrane is the flux, *J*, normalized by the membrane thickness, *l*, and the fugacity differential across it, Δf, as given by Equation 3.1. The Peng-Robinson equation of state can be used to calculate the transmembrane fugacity. Often the determination of the permeability can be further simplified by using the transmembrane pressure instead of the fugacity differential, especially for ideal systems like non-condensable gases at low pressures. Permeability is an intrinsic property of the material and its processing history that expresses the ease at which a gas molecule can move through a polymer. It is typically expressed in Barrers where 1 Barrer = 10^{-10} cm^3(STP) cm cm^{-2} s^{-1} $cmHg^{-1}$ = 3.35 x 10^{-16} mol m m^{-2} s^{-1} Pa^{-1}.

$$P = \frac{J \cdot l}{\Delta f} \approx \frac{J \cdot l}{\Delta p} \tag{3.1}$$

The permeability, *P*, can be further broken down into its diffusivity, *D*, and sorption, *S*, contributions, as shown in Equation 3.2. This equation is valid for a solution-diffusion model of transport through the membrane. In solution-diffusion, the gas must first sorb into the membrane on the upstream side, diffuse through the material, and then desorb on the downstream side.

$$P = D \cdot S \tag{3.2}$$

Typically only two of the parameters in the solution-diffusion model need to be measured experimentally, with the third calculated from Equation 3.2. In common practice, the steady state permeability is measured and time lag analysis is used to determine the diffusion coefficient from the transient region.[1] For very small gases with high diffusivities such as H_2 and He, the time lag is too small to accurately determine the diffusion coefficient. More accurate transport diffusivity coefficients can be determined by independently measuring the permeabilities and obtaining solubilities from sorption isotherms.[2] However, in this approach, the diffusivity coefficient is an average value representing the range of penetrant concentrations across the membrane from upstream to downstream.

The diffusion coefficient itself is a measure of the speed (i.e., the mean squared displacement per unit time) a gas moves through the polymer due to random thermal motions. Diffusion typically follows an Arrhenius-type dependence on temperature and can vary by several orders of magnitude due to modifications to the polymer structure.

Diffusion is fastest for small molecules, hence diffusive selectivity favors smaller kinetic diameter molecules.

The solubility coefficient reflects the gas's solubility in the polymer and typically follows a van 't Hoff relationship with temperature. Changing the solubility of inert gases is much more difficult than the diffusivity (especially for glassy polymers), and as such, chemical modifications only result in roughly an order of magnitude change in values. Solubility selectivity tends to favor the most condensable gas, i.e., the gas with the highest boiling point/critical temperature. Table 3.1 lists the boiling points of several common gases.

The most prevalent model of pressure-dependent gas sorption in glassy polymers is the dual mode sorption model. At low pressures, the concentration of the gas in the polymer resembles a Langmuir isotherm as a result of the gas adsorbing in the excess free volume sites within the polymer.[3] As the pressure increases, the rate of gas uptake begins to follow Henry's law—similar to a gas in a liquid.[3] As shown in Equation 3.3 and graphically in Figure 3.1, dual mode sorption can be expressed as the algebraic sum of the Henry's law, C_D, and Langmuir, C_H, contributions. The Henry's law coefficient is given by k_D, the Langmuir capacity constant by C'_H, the affinity constant by b, and the pressure by p.

$$C = C_D + C_H = k_D p + \frac{C'_H b p}{1 + bp} \tag{3.3}$$

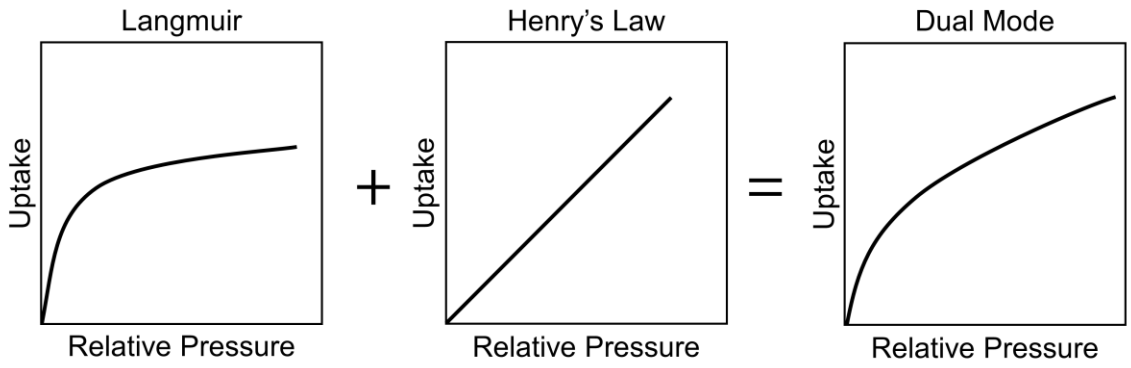

Figure 3.1 The contribution of Langmuir sorption at low pressures and Henry's law sorption at high pressures typical of dual mode sorption in glassy polymers.

Sorption isotherms can be used to construct sorption isosteres. The isosteric heat of sorption at a given loading is determined from the slope of the natural log of sorbate pressure against the inverse experimental temperature. The isosteric heats of sorption can also be modeled using dual mode parameters at different temperatures.[4]

Different methods have been proposed to correlate gas permeability with polymer structure. Frequently the polymer free volume, and more specifically the fractional free volume (FFV), is related to the diffusion coefficient and permeability by an Arrhenius-type relationships.[5] The concept of free volume is the difference in specific volume at equilibrium of a solid polymer and its occupied volume under normal conditions, a non-equilibrium quantity. Over time, the polymer free volume will decrease due to the thermal motions of the chains relaxing towards their equilibrium packing.

Theoretical models can be used to determine an occupied volume for a system. The most commonly used expression is 1.3 times the sum of the van der Waals volume, V_w, derived from Bondi's group contribution theory.[6] This term is the inverse average packing density at 0 K for complex organic molecules, which were used as polymer analogues.[6]

Equation 3.4 is used to estimate the *FFV* of a polymer where V_f is the free volume, V_{sp} is the specific volume measured from a sample, and V_{oc} is the occupied volume calculated based on theory.

$$FFV = \frac{V_f}{V_{sp}} = \frac{V_{sp} - V_{oc}}{V_{sp}} \tag{3.4}$$

In addition to permeability, selectivity is the other major defining property of a membrane. The ideal selectivity—also referred to as the permselectivity—of gas *i* compared to gas *j*, $\alpha_{i/j}$, is the ratio of pure gas permeabilities, as given by Equation 3.5. Similarly it can be expressed as a product of the diffusivity and sorption selectivities.

$$\propto_{i/j} = \frac{P_i}{P_j} = \frac{D_i}{D_j}\frac{S_i}{S_j} \tag{3.5}$$

The majority of membrane research reports performance in terms of ideal selectivities. For non-interacting gases, this does not prove to be highly problematic and serves as a useful indication of the membrane's true performance. Permeation experiments with mixed gases typically try to simulate a feed stream of interest (e.g., 50% CO_2/50% CH_4, 14% CO_2/86% N_2, etc.). Mixed gas permeation data are much more representative of actual membrane performance since they account for the competitive adsorption and possible diffusional effects between the gases and polymer. In the case of mixed gas experiments, a separation factor, given by Equation 3.6, is used rather than an ideal selectivity to describe the membrane's performance, although a selectivity based on the mixed gas permeabilities may still be calculated using Equation 3.5. The *y* values correspond to the permeate composition and the *x* values to the feed composition.

$$\beta_{i/j} = \frac{y_i/y_j}{x_i/x_j} \tag{3.6}$$

Although real process streams are composed of mixtures of many different gases, experimental setups are usually limited to binary systems when assessing membrane performance. Permeation studies of gas mixtures with more than two components quickly becomes mathematically unwieldy and performance metrics are then best represented in terms of permeate purity and target recovery. Indeed, expressions for the diffusion coefficient become highly complex due to the number of paired interactions between the gases. However, a membrane's true performance ability is best understood when investigated under the specific conditions it will be utilized.

A strong interaction between gas penetrants and a polymer matrix that results in increased polymer segmental mobility is known as plasticization. Plasticization exhibits a general increase in permeability of all species and lowering of selectivity due to a disproportionate increase in the slow gas permeability. These changes are usually due to a species strongly sorbing to the polymer and causing it to swell, similar to a solvent.

Ideally, a membrane requires a high permeability combined with a high selectivity to make it attractive for industrial applications. This tradeoff is easily visualized using selectivity-permeability plots usually referred to as Robeson plots. These plots compare gas pair selectivity to single component permeability. A current state of the art line (typically referred to as Robeson's upper bound) is then drawn based on published ideal selectivities and permeabilities, with the upper right hand corner having the most desirable combination of properties. Newly synthesized membranes are often compared on Robeson plots as a quick gauge of performance to existing materials. The initial plots created in

1991 were updated in 2008 and again in 2015 to reflect the trends in improvement of gas separation membranes.[7,8] These trends have also been theoretically supported.[9]

3.2 Organic Vapor Transport in Polymers

Similar to gas sorption, organic vapor sorption in glassy polymers can be described using dual mode sorption—as given in Equation 3.3—below any solvent-induced transitions that may occur. Sorption analysis also follows the same type as that used for gas sorption isotherms to obtain heats of sorption, although the heat of solvent condensation plays an important role.

The diffusion coefficient can be estimated from the transient data obtained during sorption isotherm measurements. For gravimetric sorption systems, the raw weight change data for each step of the isotherm can be normalized via Equation 3.7. The mass uptake at time t is given by M_t and the uptake at equilibrium (i.e., infinite time) is given by M_∞. The instantaneous sample weight is represented by m_t, the initial weight for the sorption interval by m_0, and the final mass for the sorption interval by m_∞. The normalized, non-dimensional quantity M_t/M_∞ can then be fit to an appropriate transport model to estimate the diffusion coefficient.

$$\frac{M_t}{M_\infty} = \frac{m_t - m_0}{m_\infty - m_0} \tag{3.7}$$

Different diffusional regimes exist that can significantly complicate the process of modeling mass uptake over time, especially for polymer/organic solvent systems. One simple method to quickly determine the diffusion regime uses the short-time mass uptake data for $M_t/M_\infty \leq 0.5$. Here, the short-time experimental data is fit to Equation 3.8 with k

and *n* as constants. The exponent *n* is used to determine the time dependence of the mass uptake and distinguish between different diffusion regimes.

$$\frac{M_t}{M_\infty} = kt^n \tag{3.8}$$

The most common and well-understood type of diffusion is Case I diffusion or Fickian diffusion. Case I diffusion is characterized by the transport diffusion coefficient, the rate of which is much slower than any other relaxations that might be occurring within the polymer.[10] This type of diffusion has an *n* value of 0.5 with the slope of the initial uptake being linear in square root time. There are many well established equations for modeling Case I diffusion for numerous configurations and boundary conditions.[11]

Case I diffusion is rarely exhibited for glassy polymers that have significant penetrant-induced swelling or relaxation effects. The opposite extreme is Case II diffusion where diffusion is much faster than the relaxation processes.[10] Case II diffusion has an *n* value equal to 1 with the slope of the initial uptake now being linear with time. The defining parameter of Case II diffusion is the velocity of the moving front between the swollen polymer gel and the glassy core that has yet to see the penetrant. It is mathematically more complex to determine an accurate diffusion coefficient from Case II systems because the moving front velocity is much slower than diffusion; in any event, the diffusivity in that case is no longer an important performance parameter. In rare cases, super Case II diffusion where $n \geq 1$ can exist, but it is not as well understood as Case I or Case II diffusion.[12] Both Case I and Case II are defined by only a single parameter, the diffusion coefficient and the moving front velocity, respectively.

Intermediate values of n, where $0.5 \leq n \leq 1$, are also possible and lead to the so-called anomalous diffusion regime. Anomalous diffusion is characterized by both a diffusional and relaxational component. Many different models have been proposed to accurately describe the different sorption and desorption curves for anomalous diffusion, but no single model appears to fully describe these types of systems.[11,12] Anomalous diffusion does have the advantage over Case II diffusion of being able to extract a more accurate diffusion coefficient from non-Fickian sorption data, given an appropriate model.

The Berens-Hopfenberg model is one such model that can be used to describe anomalous diffusion in glassy polymers. This model uses a linear superposition of the fast Fickian diffusion at early times, $M_{t,F}$, and slower polymer relaxations at long times, $M_{t,R}$, to determine the total mass uptake, M_t, as given in Equation 3.9.

$$M_t = M_{t,F} + M_{t,R} \tag{3.9}$$

Relative pressure changes in flowing gravimetric sorption apparatuses are not truly instantaneous step changes and require the use of an exponential boundary condition to the Fickian sorption equation.[11] The fully modified Behrens-Hopfenberg for a plane sheet is given in Equations 3.10 and 3.11. The normalized total uptake, M_t/M_∞, for the Behrens-Hopfenberg model with an exponential boundary condition (BH-exp) is the combination of the relative weight factor for Fickian contributions given by φ_F, the Fickian uptake (F-exp), and the first order relaxations with a relaxation rate constant k.

$$\left.\frac{M_t}{M_\infty}\right|_{BH-exp} = \left[\varphi_F \left(\left.\frac{M_t}{M_\infty}\right|_{F-exp}\right) + (1-\varphi_F)\big(1 - exp(-kt)\big)\right] \tag{3.10}$$

The infinite series solution for the Fickian uptake with an exponential boundary condition is given by Equation 3.11. The time is given by *t*, the time constant by τ_s, the Fickian or transport diffusion coefficient by *D*, and the film half thickness by *l*. This Berens-Hopfenberg model gives a total of four adjustable parameters—φ_F, *k*, τ_s, and *D*—that can be used to fit the normalized experimental data.

$$\left.\frac{M_t}{M_\infty}\right|_{F-exp} = 1 - exp\left(-\frac{t}{\tau_s}\right)\left(\frac{\tau_s D}{l^2}\right)^{\frac{1}{2}} \tan\left(\frac{l^2}{\tau_s D}\right)^{\frac{1}{2}} - \frac{8}{\pi^2}\sum_{n=0}^{\infty}\frac{exp\left(-D(2n+1)^2\pi^2\frac{t}{4l^2}\right)}{(2n+1)^2\left(1-(2n+1)^2\left(\frac{\tau_s D\pi^2}{4l^2}\right)\right)} \tag{3.11}$$

It is important to note that in each step of the isotherm (i.e., each incremental exposure of the film to the organic vapor), the film thickness needs to be adjusted to approximate the partially-swollen polymer film. A linear extrapolation between the dry ($p/p^0 = 0$) and the swollen ($p/p^0 = 1$) thickness can be used to estimate the film thickness as a function of penetrant loading in the absence of more accurate dilatometry measurements. The vapor-activity-dependent film thickness is almost certainly not linear, yet is representative of the diffusion values and trends obtained from more complex film thickness estimation techniques.

Loading dependent diffusion coefficient, *D*, such as the ones determined from sorption isotherm measurements, can be corrected using a thermodynamic factor as shown in Equation 3.12. The need for the thermodynamic correction comes from the nonlinear relationship between the penetrant concentration and activity where *q* is the loading and *p* is the absolute pressure at that step in the isotherm.[13] Under ideal conditions in dilute

systems, the thermodynamically corrected diffusivity, D_0, is independent of penetrant concentration.[13] However, this is generally not the case when the penetrants are strongly sorbing, as with some polymer/organic systems.

$$D = D_0 \frac{dln(p)}{dln(q)} \tag{3.12}$$

3.3 Organic Solvent Sorption and Transport in Carbon Molecular Sieve Membranes

Sorption in rigid microporous materials like carbon molecular sieves typically follows a single site Langmuir sorption isotherm, as given in Equation 3.13. The loading C is a function of the Langmuir capacity constant C'_H, the affinity constant b, and the fugacity f.

$$C = \frac{C'_H bf}{1 + bf} \tag{3.13}$$

The diffusion coefficients can be estimated with either traditional Fickian analysis or Maxwell-Stefan analysis, depending on the ideality of the system.[14] Both ideal Fickian and non-ideal Maxwell-Stefan analysis yield similar diffusion coefficients for organic molecules with nearly identical sorption isotherms in the CMS (e.g., *p*-xylene and *o*-xylene in crosslinked PVDF CMS).[14] For flowing gravimetric sorption systems, the infinite series solution with an exponential boundary condition, as given in Equation 3.11, can be used to determine the Fickian diffusion coefficient. Regardless of the exact analytical method, the transport diffusion coefficients determined from sorption isotherm measurements can also

be corrected by Equation 3.12 to obtain the thermodynamically-corrected diffusion coefficient.

For organic solvent transport in CMS, Fick's first law can be applied to calculate the intrinsic permeance of the system, assuming no bulk flow through defects in the membrane.[14] The concentration gradient can be expressed as a chemical potential gradient assuming equilibrium between the liquid phases and the membrane are maintained on both the upstream and downstream faces. The expression for the flux of component *i*, N_i, can then be used to define an intrinsic permeance P_i/l in terms of sorption and diffusion, as given in Equation 3.14.[14] The universal gas constant is given by *R*, the temperature by *T*, the specific molar volume by V_i, the concentration in mol fraction by *x*, the activity coefficient by γ, and the absolute pressure by *p* for the upstream (feed) and downstream (permeate), respectively. The Wilson equation can be used to estimate the activity coefficients. The permselectivity and separation factor can calculated by Equations 3.5 and 3.6, respectively. It is important to note that the approach described here is approximate; more exact definitions of liquid permeability in the case of non-swelling microporous membranes are still needed.

$$\frac{P_i}{l} = \frac{N_i}{\left(\frac{RT}{\hat{V}_i}\ln\left(x_{i,up}^{soln}\gamma_{i,up}^{soln}\right) + p_{up}\right) - \left(\frac{RT}{\hat{V}_i}\ln\left(x_{i,down}^{soln}\gamma_{i,down}^{soln}\right) + p_{down}\right)} \tag{3.14}$$

In gas separations, the transmembrane pressure is typically used to express the driving force (F_d) for nearly ideal systems. However, use of this transmembrane pressure to express the driving force is not accurate when describing highly non-ideal organic liquid mixtures. The intrinsic driving force takes into account the osmotic pressure of the system

and is given in Equation 3.15.[14] The composition is given by *x*, the activity coefficient by *γ*, and the hydraulic absolute pressure by *p* for the upstream and downstream, respectively. Unlike polymeric systems, the change in molar volume due to mixing is assumed to be non-zero.

$$F_d = \frac{RT}{\widehat{V}_i} \ln\left(\frac{x_{i,up}\gamma_{i,up}}{x_{i,down}\gamma_{i,down}}\right) + (p_{up} - p_{down}) \tag{3.15}$$

3.4 References

(1) Koros, W. J.; Zimmerman, C. M. Transport and barrier properties. In *Comprehensive Desk Reference of Polymer Characterization and Analysis*; Brady, R. F., Ed.; American Chemical Society: Washington, DC, 2003; pp 680-699.

(2) Bondar, V. I.; Freeman, B. D.; Yampolskii, Y. P. Sorption of Gases and Vapors in an Amorphous Glassy Perfluorodioxole Copolymer. *Macromolecules* **1999**, *32*, 6163-6171.

(3) Koros, W. J.; Chan, A. H.; Paul, D. R. Sorption and transport of various gases in polycarbonate. *J. Membrane Sci.* **1977**, *2*, 165-190.

(4) Koros, W. J.; Paul, D. R.; Huvard, G. S. Energetics of gas sorption in glassy polymers. *Polymer* **1979**, *20*, 956-960.

(5) Vrentas, J. S.; Vrentas, C. M. Predictive methods for self-diffusion and mutual diffusion coefficients in polymer-solvent systems. *Eur. Polym. J.* **1998**, *34*, 797-803.

(6) Bondi, A. *Physical Properties of Molecular Liquids, Crystals and Glasses*; Wiley: New York, 1968.

(7) Robeson, L. M. The upper bound revisited. *J. Membrane Sci.* **2008**, *320*, 390-400.

(8) Swaidan, R.; Ghanem, B.; Pinnau, I. Fine-Tuned Intrinsically Ultramicroporous Polymers Redefine the Permeability/Selectivity Upper Bounds of Membrane-Based Air and Hydrogen Separations. *ACS Macro Lett.* **2015**, *4*, 947-951.

(9) Freeman, B. D. Basis of Permeability/Selectivity Tradeoff Relations in Polymeric Gas Separation Membranes. *Macromolecules* **1999**, *32*, 375-380.

(10) Alrey, T.; Gurnee, E. F.; Lloyd, W. G. Diffusion in glassy polymers. *J. Polym. Sci. Pol. Sym.* **1966**, *12*, 249-261.

(11) Crank, J. *The Mathematics of Diffusion*; Claredon Press, 1979.

(12) Frisch, H. L. Sorption and transport in glassy polymers-a review. *Polym. Eng. Sci.* **1980**, *20*, 2-13.

(13) Kärger, J.; Ruthven, D. M.; Theodorou, D. N. *Diffusion in nanoporous materials*; John Wiley & Sons, 2012.

(14) Koh, D.-Y.; McCool, B. A.; Deckman, H. W.; Lively, R. P. Reverse osmosis molecular differentiation of organic liquids using carbon molecular sieve membranes. *Science* **2016**, *353*, 804-807.

CHAPTER 4. ORGANIC MOLECULE TRANSPORT IN THE MICROPOROUS POLYMER PIM-1

Organic molecule sorption, diffusion, and permeation in the microporous polymer PIM-1 are studied to evaluate the separation capability of the CMS precursor. The transport of organic vapors can be explained using the Berens-Hopfenberg model that accounts for Fickian diffusion and sorbate-induced swelling of the polymer matrix. Due to the susceptibility of PIM-1 to this swelling and plasticization, unmodified PIM-1 membranes are not likely to be suitable for OSRO applications—although there is potential for other types of organic solvent separations. Understanding the specifics of the polymer/nonsolvent interactions can be used to manipulate the microstructural properties of the material for new applications.

Part of this chapter is adapted from 'Jue, M. L.; McKay, C. S.; McCool, B. A.; Finn, M. G.; Lively, R. P. Effect of Nonsolvent Treatments on the Microstructure of PIM-1. *Macromolecules* **2015**, *48*, 5780-5790.' with permission of the American Chemical Society.

4.1 Introduction

Microporous polymeric materials have attracted significant interest for a variety of potential separation applications due to their combination of synthetic tunability and unusually facile processability. The most well-studied linear microporous polymer, PIM-1 (polymer of intrinsic microporosity 1, with the synthesis scheme shown in Figure 4.1),[1] has a characteristic spirocenter between the cyclopentane rings that hinders efficient chain

packing. These 90° bends in the polymer chain impart "intrinsic" microporosity and high free volume that is uncommon for amorphous, solution processable polymers. As a result, PIM materials have high permeabilities with moderate selectivities that helped redefine the current state of the art for many of the commonly studied gas pairs.[2]

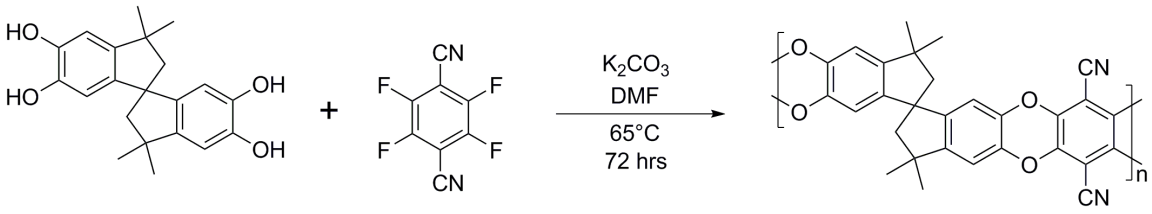

Figure 4.1 Reaction scheme for the low temperature synthesis of PIM-1.

Although the hydrophobic PIM-1 has mainly been studied as a gas separation membrane, it is a promising candidate for organic solvent nanofiltration applications since it has limited organic solvent solubility. Previous studies have focused primarily on the solvent permeance and rejection of various sized organic molecules to probe the membrane's performance.[3,4,5] However, limited transport data exists for these PIM-1 systems.[6] This work investigates the interactions and transport behavior of organic molecules with PIMs, using PIM-1 as the prototypical microporous polymer. The efficacy of methanol treatments as a means to reverse conditioning—changes to the membrane's performance with time and/or processing due to changes in the polymer microstructure—in PIM-1 is also explored. For clarity, the term nonsolvent is used to describe organic molecules, typically liquid organic solvents at ambient conditions, which cannot dissolve PIM-1.

4.2 Experimental

4.2.1 Materials

Tetrafluoroterephthalonitrile (TFTPN, Alfa Aesar) was purified via vacuum sublimation at 140°C.[7] 5,5',6,6'-tetrahydroxy-3,3,3',3'-tetramethyl-1,1'-spirobisindane (TTSBI, Alfa Aesar) was purified by reprecipitation from hot methanol with dichloromethane.[7] Anhydrous potassium carbonate (Alfa Aesar) was crushed and stored in a desiccator before use. Anhydrous *N*,*N*-dimethylformamide (DMF) was used as received. All other organic solvents were ACS grade and used as received from various commercial suppliers.

4.2.2 Synthesis of PIM-1

PIM-1 was synthesized by the low temperature polycondensation of TFTPN and TTSBI, as shown in Figure 4.1.[1] All glassware was dried in a 110°C convection oven prior to use. TFTPN (6.02 g, 30.1 mmol) and TTSBI (10.25 g, 30.1 mmol) were added to anhydrous DMF (200 mL) in a 500 mL round bottom flask. The mixture was stirred while heating to 65°C to completely dissolve the monomers. Next, potassium carbonate (10.25 g, 2.5 eq.) was added to the warmed solution and the reaction was stirred under a nitrogen atmosphere at 65°C for 72 hours. After completion, the reaction was cooled to room temperature and DI water (200 mL) was added to quench the reaction and precipitate the polymer. The mixture was then vacuum filtered and washed with additional DI water (500 mL) to remove any undissolved salts. Next the polymer was dissolved in chloroform (200 mL) and reprecipitated from methanol (400 mL). The purified polymer was vacuum filtered and dried at 70°C under vacuum until completely dry, producing PIM-1 in 86%

yield. The molecular weight as determined by gel permeation chromatography (GPC) in THF was M_n = 46,500 with a PDI = 1.5 when compared against polystyrene standards.

4.2.3 Film Casting

PIM-1 films were cast on PTFE dishes from 2 wt% PIM-1 in THF solutions and allowed to slowly dry in a saturated THF atmosphere at room temperature. The film thickness was determined by a G-6C dial thickness gauge with a 0-1 mm range and 0.001 mm graduation (Peacock).

4.2.4 Organic Vapor Sorption

DMF and methanol vapor sorption isotherms were measured in a VTI-SA+ instrument (TA Instruments). Each sorption isotherm was run on individual small coupon segments cut from a single PIM-1 film. Prior to each experiment, the coupon was soaked in methanol for at least 24 hours and dried in-situ at 115°C for 12 hours under flowing nitrogen. Organic vapor sorption isotherms were obtained at 25, 35, 45, and 55°C for DMF, methanol, *n*-heptane, toluene, *o*-xylene, and *p*-xylene in PIM-1. A maximum of 0.85 relative saturation was used to prevent damage from nonsolvent condensation within the instrument. Sample measurements were repeated at least 3 times, each on a new film, at every temperature to determine average sorption and diffusion data.

4.2.5 Nonsolvent-induced Swelling Test

Swelling tests were performed on PIM-1 films to quantify the degree of nonsolvent-induced swelling at unit activity of the nonsolvent. Previously methanol-soaked and dried samples were cut into rectangular coupons. The dry weights and coupon dimensions were

recorded before immersing the coupons in nonsolvent for at least 24 hours. Before each wet measurement, the coupon was gently dabbed with a wipe to remove excess solvent left on the surface. Each test was run in triplicate on different coupons to determine the unit activity uptake and maximum extent of isotropic swelling. Coupon dimensions were measured using ImageJ image processing software. The dry (p/p^0 = 0) and swollen (p/p^0 = 1) membrane dimensions were used to estimate the membrane film thickness as a function of vapor activity during the sorption and diffusion experiments. Thick PIM-1 films (>200 μm) were used to minimize the loss due to nonsolvent evaporation; however, the highly volatile and highly swollen nonsolvent-treated samples were still difficult to accurately measure.

4.2.6 Liquid Permeation

The hydraulic permeation of organic liquids at room temperature was measured using a high pressure stirred cell (HP4750, Sterlitech). Dense, free standing PIM-1 films were directly measured in the pressure cell without masking of the film. The feed pressure was controlled using a high pressure syringe pump (500D, Teledyne Isco). The pressure was ramped slowly, at approximately 1 psi/second, to achieve the desired upstream pressure. Samples were allowed to permeate for at least 24 hours until steady state flux was observed. The change in upstream volume with time was recorded via the syringe pump and used to calculate the flow rate through the membrane. Methanol and *n*-heptane samples were measured in triplicate on individual, methanol-treated PIM-1 films.

4.3 Results and Discussion

4.3.1 Organic Vapor Sorption

Organic vapor sorption isotherms were first measured for DMF and methanol to investigate their behavior in PIM-1. DMF was chosen as a conditioning organic solvent due to its high boiling point, polar aprotic nature, and likely favorable interactions with PIM-1—while still remaining as a nonsolvent for the high molecular weight polymer. It is important to note that DMF was used during the synthesis of PIM-1 and only becomes a nonsolvent past a critical polymer molecular weight.[7] Methanol is commonly used to reverse the effects of aging and conditioning in PIM-1 membranes and was studied to determine which properties contribute to this ability. Sorption isotherms were measured in PIM-1 films that were soaked in methanol until the time of testing to ensure a uniform processing history between different samples and experiments.

The DMF sorption isotherms in PIM-1 at 25, 35, 45, and 55°C are shown in Figure 4.2a. Sorption isotherms were repeated in at least triplicate to estimate the accuracy of the measurements. Desorption isotherms were also measured at the same relative pressure points for each experiment. The full sorption/desorption isotherm exhibits a small amount of hysteresis that follows the same shape as the sorption branch. Until high DMF relative pressures—near 0.55—the isotherm follows a dual mode response characteristic of vapor sorption in glassy polymers. At higher relative pressures (up to unit activity), the uptake begins to increase significantly and exponentially. Due to instrument limitations, all unit activity relative pressure points were measured by hand. Even with the discontinuity between measurement types, the shape of the isotherms is consistent with

those exhibited for a variety of organic vapors in PIM-1.[6] This dramatic increase in uptake at high penetrant loadings is a Flory-Huggins-type response characteristic of strongly sorbing penetrants in rubbery polymers.[8] It is important to note that even at 25°C, the unit activity nonsolvent uptake is so significant that the nonsolvent/polymer composite was more DMF than PIM-1 on both a mass and volume basis. As the penetrant loading increases, the polymer begins to swell—beyond a simple Henry's-type dissolution of penetrant into polymer—to accommodate excess penetrant into the system. The overall shape of the sorption isotherms also remains consistent as the temperature increases.

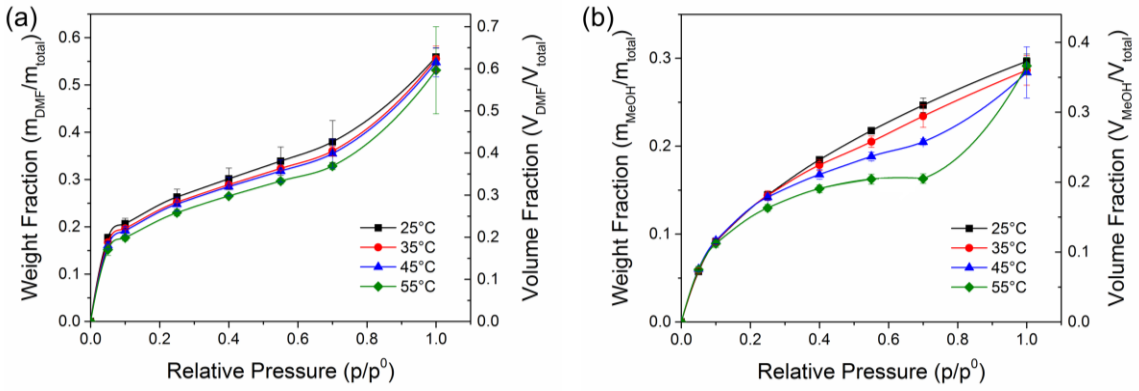

Figure 4.2 Sorption isotherms in PIM-1 from 25 to 55°C for (a) DMF and (b) methanol. Film thickness ranged from 50-90 μm. Error bars represent the standard deviation of at least three isotherm measurements, each on different films. Some error bars are smaller than the size of the marker.

The PIM-1/methanol sorption isotherm—shown in Figure 4.2b—is noticeably different compared to PIM-1/DMF. At 25°C, the isotherm exhibits a prototypical dual mode response at all methanol vapor pressures tested. Increasing temperature begins to increase swelling noticeably. It is likely that the interactions between methanol and PIM-1 become more favorable with increasing sorption temperature, which is reflected in the gradual shift from dual mode sorption behavior to sorption in a swollen network.

The total uptake at unit activity for methanol in PIM-1 is significantly lower than that of DMF, 30 wt% (37 vol%), compared to 55 wt% (58 vol%), respectively. Based on isotherm analysis alone, it is relatively clear that PIM-1 remains essentially a glass when exposed to unit activity methanol (below 35°C), whereas PIM-1 is rubbery when exposed to unit activity DMF (simple visual inspection of the membranes supports this assumption). Based on isotherm analysis, penetrant-induced transitions of PIM-1 occur at approximately 0.34 weight fraction (0.38 volume fraction) at 25°C for DMF and at approximately 0.20-0.16 weight fraction (0.27-0.22 volume fraction) at 45-55°C for methanol.[9]

Since the sorption isotherms follow a dual mode fit at low relative pressures (i.e., below the nonsolvent-induced transition previously noted), they can be used to determine the heat of sorption of the nonsolvent in PIM-1. Figure 4.3 shows the negative heats of sorption, $-\Delta H_s$, relative to the heat of condensation for both DMF and methanol. The volume fractions in Figure 4.3 span the entire dual mode relative pressure range (up to 0.55) in the sorption isotherms. Methanol in PIM-1 has a heat of sorption near its heat of condensation at low methanol loadings. In traditional, nonpolymeric microporous materials, this is indicative of new sorbates interacting with sorbates already present in the material, similar to vapor condensing on liquid already in the pores. A heat of sorption more exothermic than the heat of condensation comes from favorable interactions between the penetrant and the polymer. At higher volume fraction loadings, methanol no longer preferentially interacts with itself and begins to interact more strongly with the polymer. Although the microscopic nature of these interactions are unclear, the increase in methanol sorption exothermicity is entirely consistent with energetics of sorption in glassy polymers.[10] On the other hand, DMF exhibits a strongly exothermic interaction with PIM-

1—beyond simple pore filling—throughout the entire range of nonsolvent loadings. For DMF volume fractions above 0.2 (vol_{DMF}/vol_{total}), the heat of sorption becomes less exothermic. This behavior is also consistent with a phenomenological description of energetics.[10] At this loading, the micropores are completely filled with DMF and hole creation between the polymer chains is required to accommodate more DMF into the system. The process of hole creation is endothermic and reduces the magnitude of the exothermic response. This again indicates that the PIM-1/DMF interactions are highly favorable, especially when compared to PIM-1/methanol interactions.

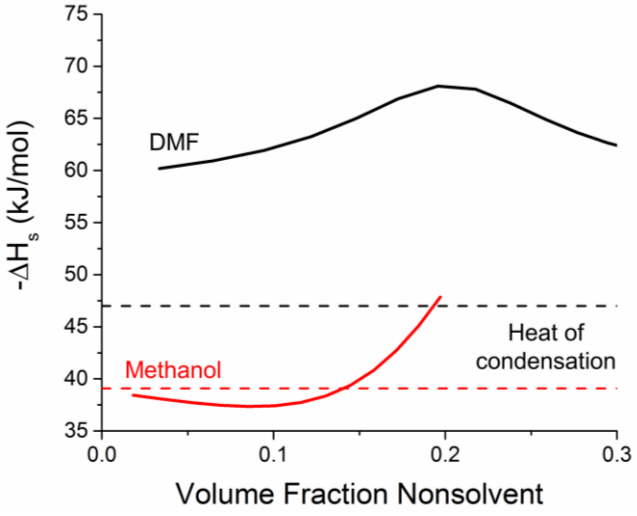

Figure 4.3 DMF and methanol isosteric heats of sorption as a function of nonsolvent loading. The dashed lines represent the corresponding heat of condensation for each nonsolvent.

4.3.2 Organic Vapor Diffusion

For the case of organic vapors in PIM-1, there is substantial penetrant-induced swelling that complicates the diffusion analysis. Short-time uptake analysis was applied to the normalized DMF mass uptake curve shown in Figure 4.4a to determine the diffusional regime. For DMF sorption in PIM-1, *n* is approximately equal to 1 at each sorption step

and is clearly Case II diffusion. However, the *n* values are less than 0.9 for each of the DMF desorption steps investigated (Figure 4.4b), thereby classifying the system as having anomalous diffusion. Considering this, vapor desorption isotherms were used to calculate the diffusion coefficients for the PIM-1/nonsolvent systems in this study. When looking at the short-time data for methanol in PIM-1, the sorption and desorption are much faster than DMF in PIM-1. Methanol sorption and desorption curves were treated as anomalous diffusion and desorption curves were used to calculate diffusion coefficients to be consistent with the DMF analysis. This classification of anomalous diffusion is in agreement with other studies of PIM-1/organic vapor systems; Vopicka et al. have investigated the sorption of a wide variety of organics and gases in PIM-1 and also observed anomalous diffusion behavior.[6]

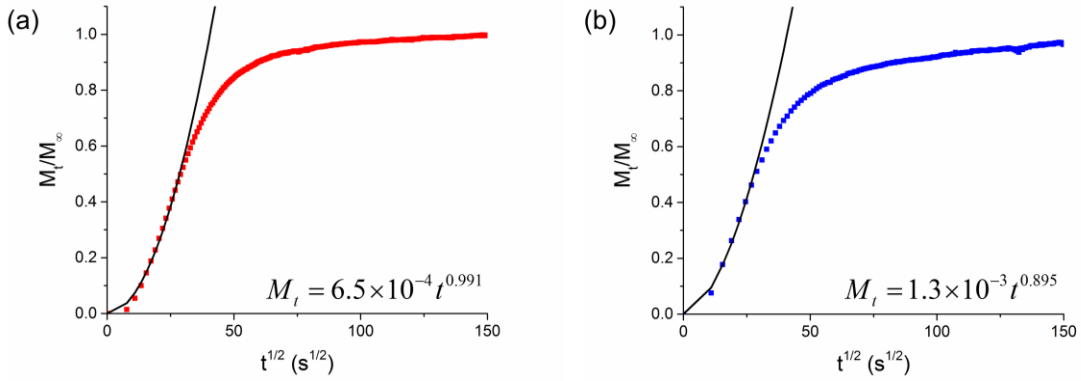

Figure 4.4 Normalized mass uptake curves for DMF (a) sorption and (b) desorption in PIM-1 with the corresponding fits for the short-time uptake analysis. The sorption step shown is from 0.10 to 0.25 relative pressure and the desorption step from 0.40 to 0.25 relative pressure at 25°C. DMF sorption in PIM-1 is Case II diffusion and DMF desorption in PIM-1 is anomalous diffusion.

In this study, the Berens-Hopfenberg model was used to analyze the anomalous diffusion data. Relative pressure changes in the gravimetric sorption apparatus are not instantaneous step changes and require the use of an exponential boundary condition for

the Fickian sorption equation for a plane sheet; Burgess and Koros have shown this to be satisfactory treatment for vapor diffusion measurements using this apparatus.[11] Other studies of water sorption in poly(ethylene terephthalate) (PET) and poly(ethylene furanoate) (PEF) showed similar sigmoidal uptake curves as these PIM-1/nonsolvent systems.[12] Burgess et al. thoroughly demonstrated the utility of this model to both fit a variety of anomalous uptake curve shapes and determine the penetrant diffusion coefficient.[12,13] As shown in Figure 4.5, the model fits are in excellent agreement with both the DMF and methanol desorption data and can accurately capture the sigmoidal behavior at early times when mass uptake is plotted against square root time.

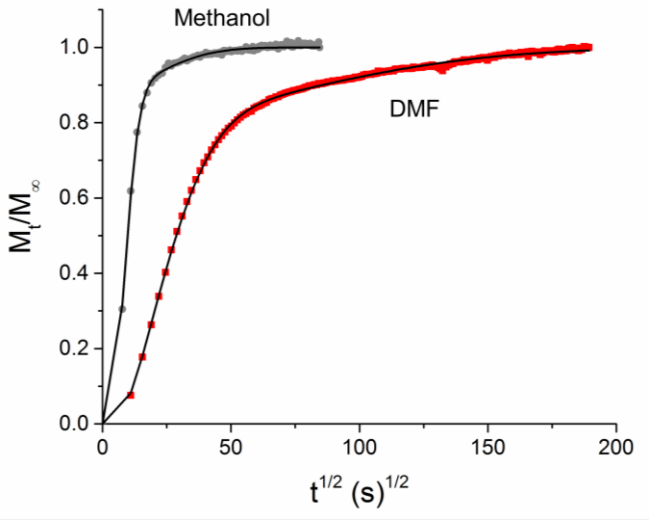

Figure 4.5 Kinetic sorption data for DMF (red squares) and methanol (gray circles) in PIM-1 for the desorption step from 0.40 to 0.25 relative pressure at 55°C. The Berens-Hopfenberg model with exponential boundary conditions is overlaid (black line) for each curve. The swelling-corrected half thickness of the DMF and methanol films are 33 ± 1 and 31 ± 1 μm, respectively.

It is important to note that in each step of the isotherm, the film thickness was adjusted to approximate the partially-swollen film thickness using a linear extrapolation. Regardless of the exact relationship chosen, the conclusions drawn from the diffusion data

are entirely unchanged, although the absolute values of the diffusion coefficients do vary slightly (± 30%). For DMF, the swollen film thickness was approximately 25% larger than the dry film; for methanol, the swollen film was 20% larger than the dry film.

Under ideal conditions in dilute systems, the thermodynamically corrected diffusivity is independent of penetrant concentration.[14] However, this is not the case when the penetrants are strongly sorbing. Two different responses can be seen in the diffusion coefficient trends in PIM-1 that are indicative of the particular polymer-penetrant interactions of the system. Plasticization leads to positive deviations from ideality with the diffusion coefficient increasing with loading. Plasticization occurs when there are favorable polymer-penetrant interactions that increase the local segmental mobility and decrease the resistance to diffusion. As the polymer begins to plasticize, it is easier for new penetrants to make the diffusive jumps through the membrane and the diffusion coefficient increases. Negative deviations (i.e., a reduction) from the ideal response—known as clustering—can occur in systems where the penetrants exhibit strong intermolecular hydrogen bonding or other strong intermolecular interactions.[15] In clustering systems, the penetrants preferentially interact with penetrants already sorbed in the polymer and additional activation energy is required to make the diffusive jumps through the membrane. In essence, clustering penetrants must overcome intermolecular attractions and the activation energy necessary to move into a free volume element. Thus at higher loadings, a decrease in the penetrant diffusion coefficient is observed.

The corrected DMF diffusion coefficients in PIM-1 at 25, 35, 45, and 55°C are shown in Figure 4.6a. Based on the diffusion data, DMF clearly plasticizes PIM-1, with almost an order of magnitude increase in diffusivity with DMF loading being observed.

This type of behavior is exhibited in other systems such as vinyl chloride in poly(vinyl chloride) where the penetrant is expected to plasticize the polymer during sorption.[16]

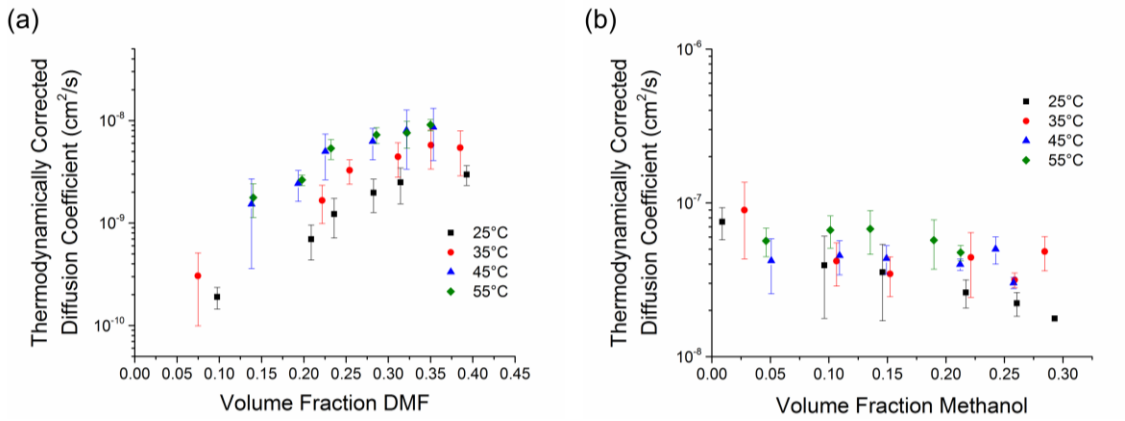

Figure 4.6 Thermodynamically corrected diffusion coefficients for (a) DMF and (b) methanol in PIM-1 as a function of loading at different temperatures. The error bars represent the standard deviations of at least three individual desorption experiments.

The thermodynamically corrected diffusivities for methanol in PIM-1 exhibit a different trend than DMF in PIM-1 as shown in Figure 4.6b. At all temperatures, the corrected diffusivity is within the same order of magnitude as a function of methanol loading—although the diffusivity tends to decrease slightly with increasing methanol loading at the lowest temperatures measured and is essentially ideal at higher experimental temperatures. The slight downturn in diffusivity with loading at lower temperatures can be indicative of methanol clustering in PIM-1, although sorption enthalpy analysis somewhat confounds this interpretation. Regardless, the diffusion data clearly shows that methanol does not plasticize PIM-1, which is a critical factor in its efficacy as an agent to reverse conditioning and aging.

4.3.3 Additional Nonsolvent Transport Data

The same procedure to analyze DMF and methanol sorption and diffusion data was applied to additional nonsolvents in PIM-1. The sorption isotherms and thermodynamically corrected diffusion coefficients for *n*-heptane, toluene, *o*-xylene, and *p*-xylene are shown in Figures 4.7 - 4.10. *n*-Heptane exhibits dual mode behavior, similar to methanol, at all loadings and temperatures. Toluene, *o*-xylene, and *p*-xylene clearly display plasticization effects. *o*-Xylene exhibits substantial sorption at unit activity, partially due to the difficulty in accurately weighing such a swollen and plasticized polymer gel.

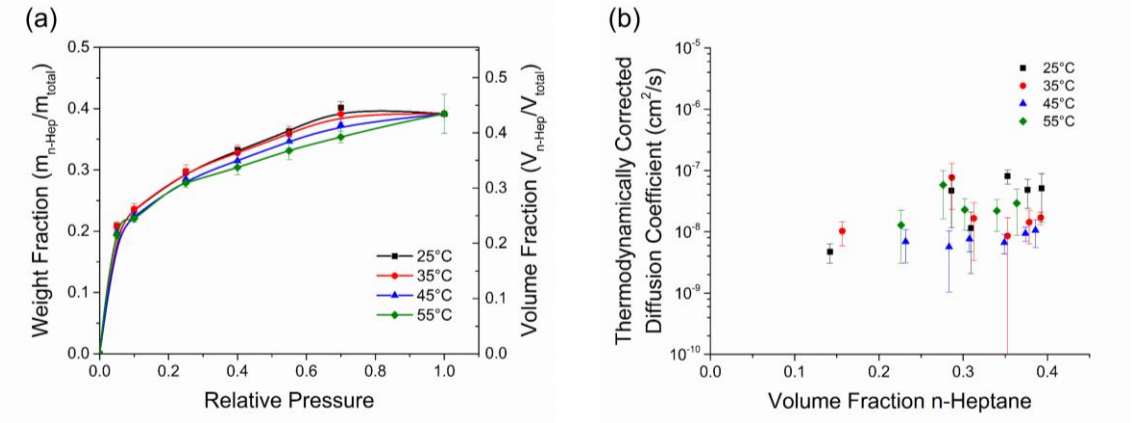

Figure 4.7 (a) Sorption isotherms and (b) thermodynamically corrected diffusion coefficients of *n*-heptane in PIM-1 from 25 to 55°C. Film thickness ranged from 60-80 µm. Error bars represent the standard deviation of at least three isotherm measurements, each on different methanol treated films.

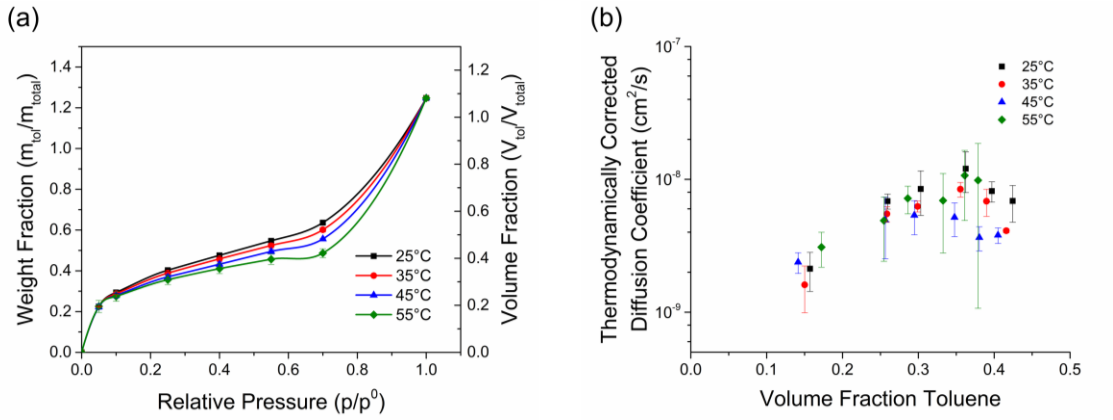

Figure 4.8 (a) Sorption isotherms and (b) thermodynamically corrected diffusion coefficients of toluene in PIM-1 from 25 to 55°C. Film thickness ranged from 60-80 µm. Error bars represent the standard deviation of at least three isotherm measurements, each on different methanol treated films.

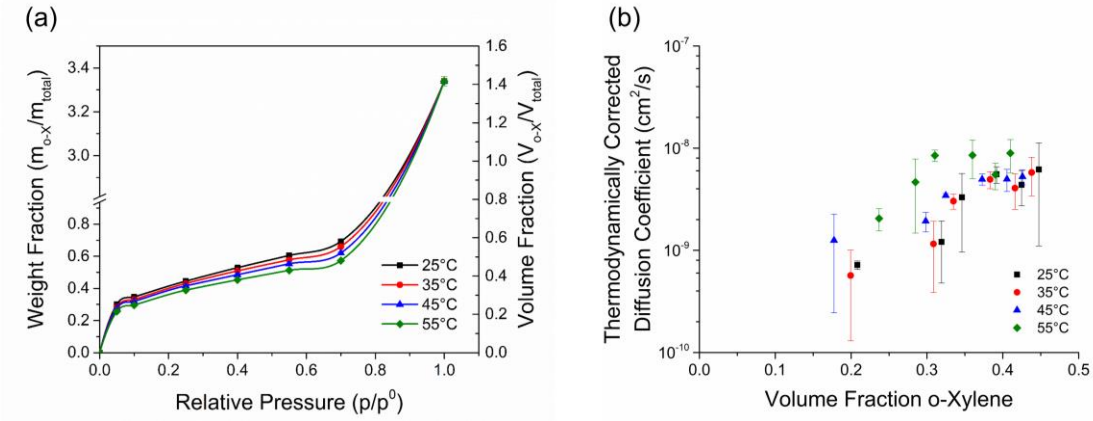

Figure 4.9 (a) Sorption isotherms and (b) thermodynamically corrected diffusion coefficients of *o*-xylene in PIM-1 from 25 to 55°C. Film thickness ranged from 60-80 µm. Error bars represent the standard deviation of at least three isotherm measurements, each on different methanol treated films.

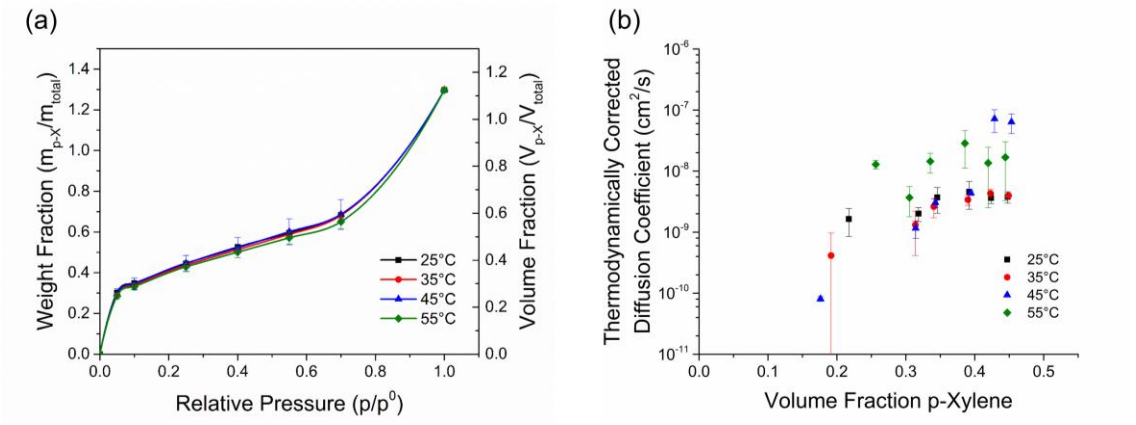

Figure 4.10 (a) Sorption isotherms and (b) thermodynamically corrected diffusion coefficients of *p*-xylene in PIM-1 from 25 to 55°C. Film thickness ranged from 60-80 µm. Error bars represent the standard deviation of at least three isotherm measurements, each on different methanol treated films.

4.3.4 Swelling and Plasticization

Swelling and plasticization are often mentioned when discussing the behavior of strongly interacting polymer-penetrant systems. Typically, swelling and plasticization occur simultaneously within a system and are often used interchangeably in the literature. However, there is a subtle difference between the effects of swelling and plasticization in glassy polymers that is particularly important when discussing the behavior of nonsolvents such as DMF and methanol interacting with PIM-1.

On one hand, swelling is a sorbate-induced change in the polymer specific volume and can be accurately defined as a positive deviation from volume additivity for guest sorption in glassy polymers. This is essentially due to guest sorption in unrelaxed free volume elements or in the permanent micropores in the case of PIMs. Additional dissolved guest sorption—Henry's-type sorption—is believed to be responsible for polymer volume changes upon sorption.[8] In the dissolved sorption mode, sorbates cause polymer chain

segments to separate to accommodate additional sorbate molecules, which is dependent on the Henry's law constant for that particular polymer-sorbate pair. In general, swelling can be observed on the macroscopic scale and is relatively easy to quantify.

On the other hand, plasticization is an increase in the polymer's segmental mobility due to favorable polymer-penetrant interactions. Plasticization manifests itself in a number of measurable properties such as increased gas permeability with increasing pressure, increased penetrant diffusivity, lowering of the glass transition temperature, etc. The CO_2-induced plasticization effects on glassy polymers have been extensively studied.[17,18,19] In these systems, sorbate-induced increases in sorption are the result of strong polymer-CO_2 interactions that both swell and plasticize the polymer network. Relative to swelling analysis, more detailed sorption, diffusion, and/or permeation data are needed to quantitatively determine the extent of plasticization in a given polymer-penetrant system. It is worth noting that it is possible to have swelling in glassy polymers without plasticization (as shown in Figure 4.6b and Figure 4.11 for methanol). Conversely, plasticization onset is clearly linked to swelling and in fact is usually linked with an increase in swelling tendency.[20]

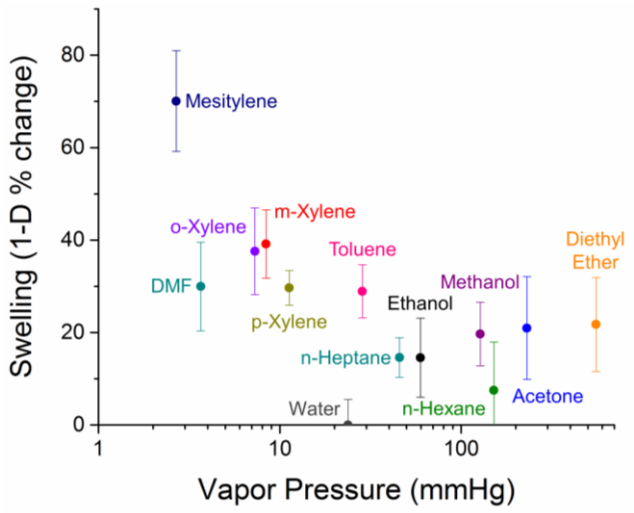

Figure 4.11 One dimensional organic-induced swelling in PIM-1 at 25°C. Error bars represent the standard deviation measured from three films.

Many different organics appreciably swell PIM-1 and some strongly plasticize it. These two factors are crucial in elucidating the role of nonsolvent sorption and diffusion in the conditioning of PIM-1. Another critical factor is the vapor pressure of the nonsolvent, as the vapor pressure directly relates to the driving force for surface evaporation from the film. Figure 4.11 shows the relative amount of swelling against the vapor pressure of many different organic nonsolvents in PIM-1 at 25°C. Especially for the very high swelling and very high vapor pressure organics, the amount of swelling was experimentally difficult to measure accurately due to low mechanical integrity of the films or very fast nonsolvent evaporation while weighing, respectively. Generally, films with very high nonsolvent mass uptakes (where there is more nonsolvent than polymer) are too swollen to be useable in any practical membrane application. *o*-Xylene in PIM-1 had the highest mass uptake of the nonsolvents measured with a 330 wt% increase. Mesitylene in PIM-1 had a similarly high mass uptake, 310 wt% increase, but the observed swelling was twice as large as *o*-xylene. The amount of swelling and the mass uptake are not linearly related and further allude to

the differences between the specific polymer-penetrant interactions even for chemically similar penetrants.

Both DMF and methanol swell PIM-1 to a similar degree (Figure 4.11)—30% and 20%, respectively. However, the vapor pressure for methanol is 40 times greater than that of DMF at 25°C. This high vapor pressure is another necessary component for understanding why methanol treatments are effective at increasing the free volume in polymers and how that reverses aging. The higher vapor pressure leads to a stronger driving force for the nonsolvent to evacuate the polymer once the sample is removed from the liquid. The boundary condition for nonsolvent evaporation is proportional to $p^0_{nonsolvent} - p_{nonsolvent,ambient}$. Ideally, a nonsolvent with a very high vapor pressure, a large degree of swelling in PIM-1, and little to no plasticization would be desirable for a nonsolvent treatment to increase the free volume. Single factors, like high degree of swelling alone, are not sufficient to increase the free volume once the film is dried. It is unlikely that there exists a nonsolvent that can swell PIM-1 to the extent of mesitylene with a very high vapor pressure that would not also significantly plasticize. Indeed, the evaporation rate is a key parameter in determining the extent of additional free volume that can be added or removed from PIM-1 as a result of nonsolvent conditioning.

4.3.5 Organic Liquid Permeation

The solution-diffusion model can be applied to describe the pure component transport of organic molecules in polymeric membranes. Using the sorption and diffusion coefficients obtained from the gravimetric sorption isotherm experiments, the permeability of the membrane can be predicted and compared to experimentally measured permeation

results. The methanol and *n*-heptane permeabilities at room temperature are shown in Figure 4.12. Only the nonsolvents that do not significantly plasticize PIM-1 were successfully tested under the hydraulic permeation conditions used. The solution-diffusion model predicts permeability values that are within ~50% of those measured for methanol and ~170% for *n*-heptane. Some of this error can be attributed to using the loading-dependent diffusion coefficient obtained at only 0.85 relative pressure (due to the limitations of the vapor sorption instrument). Using approximately unit activity diffusion coefficients would be a more accurate representation of the liquid-phase behaviour occurring during hydraulic permeation. Especially for *n*-heptane, the large standard deviation in the diffusion coefficient estimation (which itself is based on an estimation of the swollen film thickness) leads to very large standard deviations in the predicted permeability from the solution-diffusion model. Despite the large uncertainty, these measurements reflect good agreement in the transport behavior—especially when considering that the sorption, diffusion, and permeation were each measured independently on separate apparatuses using different membranes.

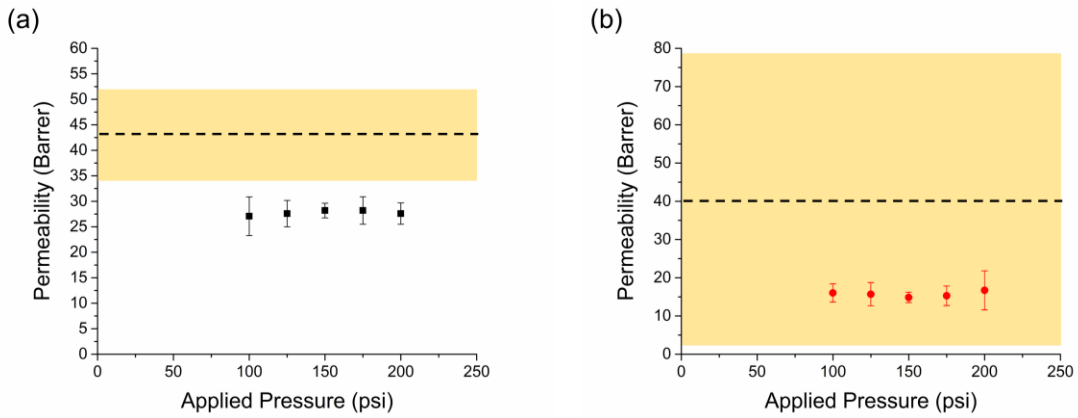

Figure 4.12 (a) Room temperature methanol permeability in PIM-1. (b) Room temperature *n*-heptane permeability in PIM-1. The predicted permeability based on the solution-diffusion model is shown by the dashed line and the uncertainty in gold.

Solvents that do noticeably plasticize the membrane, such as DMF, toluene, and xylenes, were not testable in the high pressure cells. The swollen and plasticized PIM-1 membranes softened significantly and were not mechanically robust enough to withstand the applied pressure. As a result, the membranes tore and developed substantial defects during pressurization. Attempts at masking the PIM-1 films using solvent-proof epoxy and aluminium foil were equally problematic, as the polymer swells significantly in the presence of solvent, creating wrinkled membranes with poor adhesion to the foil.

Although not feasible for OSRO-type separations due to the significant swelling and potential plasticization, PIM-1 membranes have been investigated for a few OSN applications.[3-5] Typically, non-plasticizing solvents such as alcohols or linear alkanes are used as the solvent for organic dyes to measure the rejection.[3-5] However, the influence of plasticizing solvents on the rejection performance has not been investigated. A mixed solvent system of varying concentrations of *n*-heptane/toluene was used to probe the effects of solvent-induced plasticization on polystyrene oligomer rejection. Unfortunately, reliable

rejection results were difficult to obtain due to concerns over the quality of the dense PIM-1 membranes used. Even for large area membranes, the thick films had low fluxes that caused the membranes to exhibit unrealistic rejection results. Although the initial OSN experiments were inconclusive, it is still probable that the introduction of plasticizing nonsolvents will decrease the rejection performance while simultaneously increasing the permeance of the membrane, similar to plasticization in gas separation membranes.

4.4 Conclusions

While extensively characterized for gas separations, PIM-1 membranes have shown some interesting performance for separations involving organic solvents. The transport of organic vapor molecules in PIM-1 follows that of a glassy polymer, rather than a rigid microporous material. The large amount of accessible pore volume acts to increase the sorption capacity of the organics, leading to high permeabilities, without significantly altering the transport behavior mechanism. The diffusion of organics is well described by the Berens-Hopfenberg model, which accounts for both Fickian diffusion and anomalies due to sorbate-induced polymer relaxations. Organic solvents such as methanol and *n*-heptane that have fairly high vapor pressures and lower propensities to swell PIM-1 do not plasticize the polymer and can be utilized as the solvent for OSN separations. However, highly swelling, low vapor pressure organic solvents such as DMF, toluene, and xylenes significantly plasticize PIM-1 and ultimately render the membranes unusable for these applications.

Although PIM-1 does show some promise for separations involving organic solvents such as OSN, the above mentioned swelling and plasticization effects do not make

unmodified PIM-1 membranes attractive for OSRO. However, the ability to manipulate PIM-1 via exposure to different nonsolvents allows for facile tailoring of the polymer at the microstructural level.

4.5 References

(1) Mason, C. R.; Maynard-Atem, L.; Al-Harbi, N. M.; Budd, P. M.; Bernardo, P.; Bazzarelli, F.; Clarizia, G.; Jansen, J. C. Polymer of Intrinsic Microporosity Incorporating Thioamide Functionality: Preparation and Gas Transport Properties. *Macromolecules* **2011**, *44*, 6471-6479.

(2) Robeson, L. M. The upper bound revisited. *J. Membrane Sci*. **2008**, *320*, 390-400.

(3) Fritsch, D.; Merten, P.; Heinrich, K.; Lazar, M.; Priske, M. High performance organic solvent nanofiltration membranes: Development and thorough testing of thin film composite membranes made of polymers of intrinsic microporosity (PIMs). *J. Membrane Sci*. **2012**, *401-402*, 222-231.

(4) Gorgojo, P.; Karan, S.; Wong, H. C.; Jimenez-Solomon, M. F.; Cabral, J. T.; Livingston, A. G. Ultrathin Polymer Films with Intrinsic Microporosity: Anomalous Solvent Permeation and High Flux Membranes. *Adv. Funct. Mater.* **2014**, *24*, 4729-4737.

(5) Tsarkov, S.; Khotimskiy, V.; Budd, P. M.; Volkov, V.; Kukishkina, J.; Volkov, A. Solvent nanofiltration through high permeability glassy polymers: Effect of polymer and solute nature. *J. Membrane Sci*. **2012**, *423-424*, 65-72.

(6) Vopicka, O.; Friess, K.; Hynek, V.; Sysel, P.; Zgazar, M.; Sipek, M.; Pilnacek, K.; Lanc, M.; Jansen, J. C.; Mason, C. R.; Budd, P. M. Equilibrium and transient sorption of vapours and gases in the polymer of intrinsic microporosity PIM-1. *J. Membrane Sci*. **2013**, *434*, 148-160.

(7) Song, J.; Du, N.; Dai, Y.; Robertson, G. P.; Guiver, M. D.; Thomas, S.; Pinnau, I. Linear High Molecular Weight Ladder Polymers by Optimized Polycondensation of Tetrahydroxytetramethylspirobisindane and 1,4-Dicyanotetrafluorobenzen. *Macromolecules* **2008**, *41*, 7411-7417.

(8) Fleming, G. K.; Koros, W. J. Dilation of polymers by sorption of carbon dioxide at elevated pressures. 1. Silicone rubber and unconditioned polycarbonate. *Macromolecules* **1986**, *19*, 2285-2291.

(9) Minelli, M.; Friess, K.; Vopicka, O.; De Angelis, M. G. Modeling gas and vapor sorption in a polymer of intrinsic microporosity (PIM-1). *Fluid Phase Equilibr*. **2013**, *347*, 35-44.

(10) Koros, W. J.; Paul, D. R.; Huvard, G. S. Energetics of gas sorption in glassy polymers. *Polymer* **1979**, *20*, 956-960.

(11) Crank, J. *The Mathematics of Diffusion*, 2nd ed.; Clarendon Press: Oxford, 1979.

(12) Burgess, S. K.; Mikkilineni, D. S.; Yu, D. B.; Kim, D. J.; Mubarak, C. R.; Kriegel, R. M.; Koros, W. J. Diffusion Coefficient Modeling in Polyester Barrier Materials: Applications of Infinite Series Solutions. *Polymer* **2014**, *55*, 6870-6882.

(13) Burgess, S. K.; Kriegel, R. M.; Koros, W. J., Diffusion Coefficient Modeling in Polyester Barrier Materials: Applications of Infinite Series Solutions. *Soc. Plast. E. - ANTEC*, Las Vegas, Nevada, 2014; pp 830-835.

(14) Kärger, J.; Ruthven, D. M.; Theodorou, D. N. *Diffusion in Nanoporous Materials*; John Wiley-VCH: Germany, 2012.

(15) Kamaruddin, H. D.; Koros, W. J. Sorption of methanol/MTBE and diffusion of methanol in 6FDA-ODA polyimide. *J. Polym. Sci. Pol. Phys*. **2000**, *38*, 2254-2267.

(16) Berens, A. R. Diffusion and relaxation in glassy polymer powders: 1. Fickian diffusion of vinyl chloride in poly(vinyl chloride). *Polymer* **1977**, *18*, 697-704.

(17) Chan, A. H.; Paul, D. R. Influence of history on the gas sorption, thermal, and mechanical properties of glassy polycarbonate. *J. Appl. Polym. Sci*. **1979**, *24*, 1539-1550.

(18) Chiou, J. S.; Barlow, J. W.; Paul, D. R. Plasticization of glassy polymers by CO_2. *J. Appl. Polym. Sci*.**1985**, *30*, 2633-2642.

(19) Wind, J. D.; Sirard, S. M.; Paul, D. R.; Green, P. F.; Johnston, K. P.; Koros, W. J. Carbon Dioxide-Induced Plasticization of Polyimide Membranes: Pseduo-Equilibrium Relationships of Diffusion, Sorption, and Swelling. *Macromolecules* **2003**, *36*, 6433-6441.

(20) Wind, J. D.; Sirard, S. M.; Paul, D. R.; Green, P. F.; Johnston, K. P.; Koros, W. J. Relaxation Dynamics of CO_2 Diffusion, Sorption, and Polymer Swelling for Plasticized Polyimide Membranes. *Macromolecules* **2003**, *36*, 6442-6448.

CHAPTER 5. FABRICATION OF DEFECT-FREE PIM-1 HOLLOW FIBER MEMBRANES

A modified dual-bath method of spinning was employed to fabricate defect-free, integrally skinned, asymmetric PIM-1 hollow fiber membranes utilizing an immiscible liquid protective layer. Spinning techniques capable of addressing specific challenges presented by PIM-1 solutions are discussed. In particular, dual-bath spinning via a triple orifice spinneret circumvents the primary issue associated with spinning PIM-1, namely the lack of suitable nonvolatile solvents. The water-immiscible sheath layer coextruded with the PIM-1 polymer solution reduces evaporation of the volatile solvent (tetrahydrofuran) relative to fibers directly exposed to air, thus producing an asymmetric hollow fiber membrane structure. The work here describes the process of developing spin dopes, fabricating hollow fibers, and gas testing the resulting membrane modules. While not directly applicable for organic solvent separations, the fabrication of PIM-1 membranes in the hollow fiber morphology is a vital first step for improving the development of CMS membranes for OSRO.

Part of this chapter is adapted from 'Jue, M. L.; Breedveld, V.; Lively, R. P. Defect-free PIM-1 hollow fiber membranes. *J. Membrane Sci.* **2017**, *530*, 33-41.' with permission of Elsevier B. V.

5.1 Introduction

As a result of PIM-1's exceptional separation performance, many new microporous polymers have been developed utilizing and refining the original design principles—often

resulting in the production of new polymers that exceed PIM-1's performance.[1] However, one major limitation to the large scale implementation of these advanced materials is the lack of development of scalable membrane morphologies. Research on new polymeric membrane materials is almost exclusively focused on dense flat sheet or thin film composite membrane morphologies.[2-5] While advantageous for fundamental polymer characterization due to the relatively small amount of material required, flat sheet membranes—and by extension plate and frame membrane modules—are often not suitable for processes with limited space or extreme pressure requirements.[6] Hollow fiber membranes (HFMs) are another membrane morphology that utilizes asymmetric, or partially porous (i.e., a radial gradient in porosity that terminates in a dense membrane layer), membranes to create high-flux devices with very high pressure resistance.[6,7] Hollow fibers are already used industrially due to their highly scalable production and ease of fabrication into high surface area-to-volume ratio modules.[8]

Typical hollow fiber membranes are made from a handful of commercially available and well-studied polymers such as cellulose acetate, poly(ether sulfone), and several polyimide-containing polymers.[9] The fabrication process of HFMs requires significantly more polymer and specialized equipment than that of thin film composite membranes and is likely a limiting factor to the development of HFMs from new polymers. Before this work, no integrally skinned, asymmetric PIM-1 HFMs had been fabricated, in part due to the poor solubility properties of PIM-1 relative to polymers traditionally used to create HFMs. Attempts have been made to produce PIM-1 HFMs, but only low incorporation blends, with 15 wt% PIM-1 or less, were achieved.[10,11] Even this low

percentage of PIM-1 in the polyimide hollow fibers significantly improved the separation performance and gives precedence to fabricating a HFM entirely out of a PIM polymer.[10,11]

The work described here details the process of spinning the first defect-free, pure PIM-1 HFMs with accompanying characterization and gas separation analysis to quantify the performance metrics. PIM-1 is known to age substantially after film formation and its long term performance has been questioned.[12] However, significant research has been dedicated to develop methods for arresting this aging process and these methods could likely be applied to the spinning process described here.[12-16] It is important to note that the focus of this study is the development of protocols for spinning PIM polymers, using PIM-1 as the prototypical example, and not the effects of aging. The techniques discussed can also be applied to spinning other high performance polymers with similar solubility limitations, such as many of the PIM-1 derivative polymers that have already been described in the literature.[1]

5.2 Experimental

5.2.1 Materials

PIM-1, with a number average molecular weight of 65,000 Da and PDI less than 2, was synthesized and characterized as previously described via the low temperature method.[17] *N*,*N*-Dimethylformamide (DMF), *N*-methyl-2-pyrrolidone (NMP), tetrahydrofuran (THF), *N*,*N*-dimethylacetamide (DMAc), tetrahydropyran (THP), 1-butanol, methanol (MeOH), ethanol (EtOH), and hexanes (a mixture of hexane isomers containing 60% *n*-hexane) were purchased from Alfa Aesar or VWR and used without further purification.

Gases used for fiber permeation were 99+% pure. Ultra high purity (UHP) grade helium, hydrogen, nitrogen, argon, and methane were supplied by Airgas. Ultra pure carrier (UPC) grade oxygen, research grade carbon dioxide, and research grade ethane were also supplied by Airgas. Instrument grade (99.5% pure) ethylene was supplied by Tech Air.

5.2.2 Spin Dopes

The composition of the final polymer solution was chosen based on cloud point measurements. Ternary mixtures of PIM-1, solvent, and nonsolvent were mixed in 20 mL sample vials. Varying solution compositions were used to understand the ternary phase space and locate the position of the binodal line—the delineation between the one phase and two phase solution composition regions. The binodal line was estimated using the dope compositions that formed either turbid or partially dissolved solutions. Ternary phase diagrams were created for multiple PIM-1/solvent/nonsolvent systems.

Polymer dopes used for spinning were prepared by allowing the solution of polymer, solvent, and nonsolvent to slowly mix in a sealed glass jar on a heated roller until a homogenous, transparent, and bubble-free solution was obtained. PIM-1 was dried overnight at 70°C under vacuum before use. Dry THF, DMAc, and EtOH were used as the solvent and nonsolvents, respectively.

5.2.3 Hollow Fiber Spinning

Hollow fiber membranes were spun using the spinning apparatus shown schematically in Figure 5.1. A second outer sheath layer was coextruded along with the polymer dope and bore fluid from a triple orifice spinneret.[18] For spinning PIM-1, the

sheath layer was composed of a nonsolvent fluid rather than a secondary polymer dope typically used in dual-layer spinning. The dope, bore, and sheath fluids were pressurized via high pressure syringe pumps (Teledyne Isco) and fed through a custom designed triple orifice spinneret also depicted schematically in Figure 5.1.

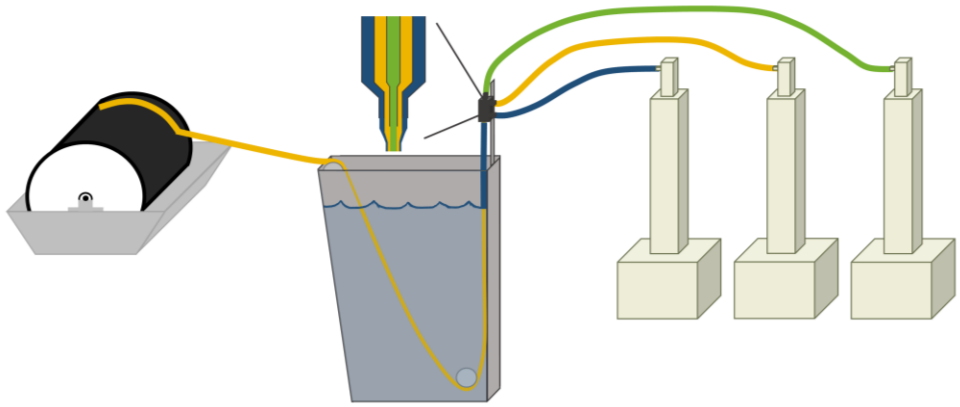

Figure 5.1 Schematic of the spinning apparatus and triple orifice spinneret used to produce PIM-1 hollow fiber membranes. The bore fluid is shown in green, the polymer dope in yellow, and the sheath layer in blue. The three fluids are simultaneously coextruded through the spinneret into the water quench bath, moved around guides, and collected on the take up drum.

Although many conditions were tested, three specific sets of conditions are used as examples to highlight important aspects of spinning PIM-1 HFMs. For clarity, the term 'state' is used to refer to the exact spinning parameters used (compositions, flow rates, air gaps, etc.) to produce a particular set of fibers. The term 'spin' refers to a group of states where various operating parameters were changed systematically, but with a constant dope composition. The parameters for each state discussed here are listed in Table 5.1 as States S1, S2, and S3, respectively.

Table 5.1 Spinning parameters for States S1, S2, and S3. The spinneret was kept at 22°C and the water quench bath at 50°C for each spin.

Parameter	S1	S2	S3
Dope Composition (wt%)	17.5 PIM-1 67.5 THF 12.75 DMAc 2.25 EtOH	15 PIM-1 69.5 THF 13.25 DMAc 2.25 EtOH	15 PIM-1 69.5 THF 13.25 DMAc 2.25 EtOH
Bore Fluid Composition (wt%)	50 THF 42.5 DMAc 7.5 EtOH	45 THF 46.75 DMAc 8.25 EtOH	45 THF 46.75 DMAc 8.25 EtOH
Sheath Composition (wt%)	100 1-Butanol	100 1-Butanol	82.5 1-Butanol 17.5 THF
Dope/Bore/Sheath/Flow Rates (mL/h)	120/40/50	120/80/75	120/120/75
Air Gap (mm)	25	15	15
Take Up Drum Rate (m/min)	1.5	1.5	2
Draw Ratio	0.84	0.84	0.90

After spinning, the fibers were soaked in deionized water for three days—with the water changed daily—to remove any residual solvents.[7] The fibers were then solvent exchanged in a two-step process, methanol followed by hexanes, before drying at 50°C under vacuum overnight.[7] This solvent exchange protocol was used to gradually decrease the surface tension of the liquid inside the pores of the nascent membranes to prevent unnecessary densification of the substructure.[8] Once the fibers were completely dry, they were allowed to age at ambient conditions for two months before permeation testing to avoid the confounding effects of rapid initial aging during measurements.[20,21]

5.2.4 Hollow Fiber Module Preparation

Single hollow fiber membranes were assembled into modules made from ¼ inch stainless steel tubing and Swagelok® fittings as described in detail elsewhere.[22] 3M™ DP100 clear epoxy was used to seal the modules and separate the bore and shell sides from one another. Modules were left to cure overnight at ambient conditions before testing.

5.2.5 Single Fiber Gas Permeation

Hollow fiber modules were tested in a high throughput, temperature controlled, isobaric permeation system. To acquire triplicate measurements for each experiment, three membrane modules each with a single fiber were connected in parallel to the gas feed and slowly pressurized to 100 psig. Fibers were pressurized on the shell side of the module and the permeate analyzed through the bore side. The temperature was maintained at either 25, 35, or 45°C and allowed a minimum of 4 hours to reach thermal equilibrium. The permeate flow rate for each module was measured using a soap bubble flowmeter. Modules were allowed to permeate for a minimum of 12 hours after switching gas feeds before any measurements were taken. Steady state permeation was assumed when no discernable change in permeate flow rate over a two hour period was observed.

Pure component methane and carbon dioxide permeation at 35°C were used to quickly assess the selectivity of the newly spun (unaged) membranes. Sufficiently defect-free fibers were then allowed to age for two months before comprehensive permeation testing. Single component permeation measurements were taken at 100 psig feed pressure and 25, 35, and 45°C for helium, hydrogen, oxygen, nitrogen, argon, methane, carbon dioxide, ethane, and ethylene in that order. The gases were tested in approximate order of

increasing sorption affinity and from low to high temperature to minimize the effects of plasticization and conditioning on the permeation results. The permeate flow rate was used to calculate the membrane permeance. With the exception of carbon dioxide, ethane, and ethylene, the transmembrane fugacity can be accurately represented by the transmembrane pressure. All permeation measurements were taken from the same set of triplicate modules.

5.2.6 Surface Area and Pore Size Analysis

BET surface areas and pore volumes of PIM-1 were determined from nitrogen physisorption measurements at 77 K taken on a BELSORP-max (Microtrac). Samples were degassed before analysis at 110°C under vacuum for 12 hours. Fiber pore size was determined using an AutoPore IV mercury porosimeter (Micromeritics) without prior degassing.

5.2.7 Scanning Electron Microscopy

Samples were sputtered using a Hummer 6 Gold/Palladium Sputterer. Scanning electron microscopy (SEM) was performed using a Hitachi SU8230 FE-SEM with a cold field emission gun at 5 kV accelerating voltage and 20 μA emission current. The image processing software ImageJ was used to estimate fiber dimensions based on these SEM images.

5.3 Results and Discussion

5.3.1 Development of Ternary Phase Diagrams

Ternary phase diagrams are particularly useful for estimating the behavior of polymer solutions during the spinning process. Many different ternary phase diagrams have been published for the commonly spun polymers and usually contain some combination of volatile solvent, nonvolatile solvent, volatile nonsolvent, and nonvolatile nonsolvent with the possible inclusion of other additives such as pore formers.[23] All of these components allow the phase inversion process to be fine-tuned and precisely controlled to form the desired morphological structure. NMP is the most common nonvolatile solvent and usually is the majority component in spin dopes because of its strong solvating power, miscibility with water in the quench bath, low volatility, and relatively benign health hazards. PIM-1 is unusual compared to other polymers used for hollow fiber spinning in that it is insoluble in NMP; indeed, NMP acts as a very weak nonsolvent for PIM-1. As such, only low concentrations of PIM-1 can be incorporated into NMP and still remain a one phase solution.[10,11] However, PIM-1 dopes with polymer and NMP concentrations typically found in the literature for spinning glassy polymers yield a two phase solution.

By far the most prevalent solvents used for film casting of PIM-1 are tetrahydrofuran, chloroform, and dichloromethane, although a few other chlorinated solvents can be used. Each of these solvents is considered volatile—boiling points less than roughly 100°C, but chloroform and dichloromethane are immiscible with the water quench bath and significantly more toxic than THF. As a result, THF is likely the only possible solvent choice for dry jet/wet quench spinning of PIM-1. The lack of a nonvolatile

solvent—and the resulting consequence of having to use a dope comprised of only volatile components—significantly complicates the spinning of PIM-1, as will be discussed in detail later on.

The ternary phase diagrams for two different nonsolvent choices are shown in Figure 5.2. For these types of systems, the area to the left of the binodal line is the one-phase region and the area to the right is the two-phase region. The binodal line for the PIM-1/THF/NMP system (blue squares in Figure 5.2) designates a large and predominantly one phase region and a very small two phase region. This clearly indicates that NMP acts as a very weak nonsolvent for PIM-1 since two phase behavior is only seen at NMP concentrations greater than 70 wt%. The shape of this PIM-1/THF/NMP ternary phase diagram is also "inverted" compared to typical ternary phase diagrams—most ternary phase diagrams used for spinning are predominantly composed of the two phase region like the one shown for DMAc/EtOH nonsolvents in Figure 5.2.[23] The inverted nature of this phase diagram makes it difficult to predict how the dope will phase separate upon introduction to the water quench bath. Several attempts at spinning hollow fibers from NMP-rich dopes yielded round fibers with the desired asymmetric structure. However, those fibers were very difficult to spin and extremely brittle once dried—to the point of being essentially untestable—and that dope composition was ultimately abandoned for subsequent spins.

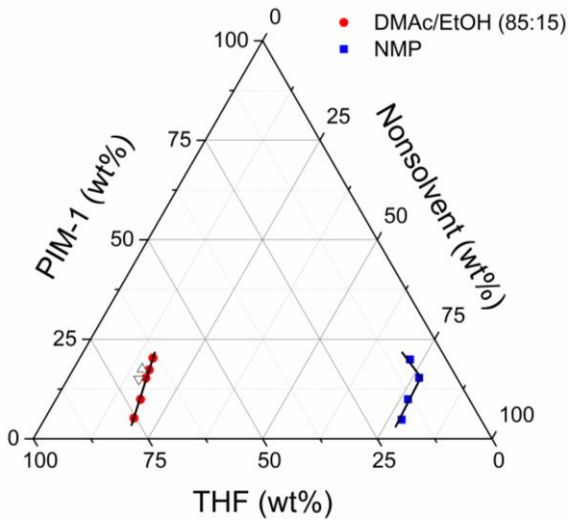

Figure 5.2 Ternary phase diagram for various PIM-1 solutions. The binodal line for PIM-1/THF/DMAc/EtOH with a constant DMAc to EtOH ratio of 85 wt% to 15 wt% (red circles) and binodal line for PIM-1/THF/NMP (blue squares) are shown. The upwards triangle indicates the dope composition used in Spin 1 and the downwards triangle indicates the dope composition used in Spins 2 and 3.

Additional ternary phase diagrams for other PIM-1/THF/nonsolvent systems were created to develop a deeper understanding of the nonsolvent effects on the PIM-1 solution properties. Due to the hydrophobic nature of PIM-1, even the addition of small amounts of water—less than 0.5 wt%—to the spin dope causes phase separation to occur as can be seen in the ternary phase diagram in Figure 5.3. Alcohols, such as ethanol, are generally weaker nonsolvents than water for hydrophobic polymers (Figure 5.4) and can act as volatile nonsolvents.

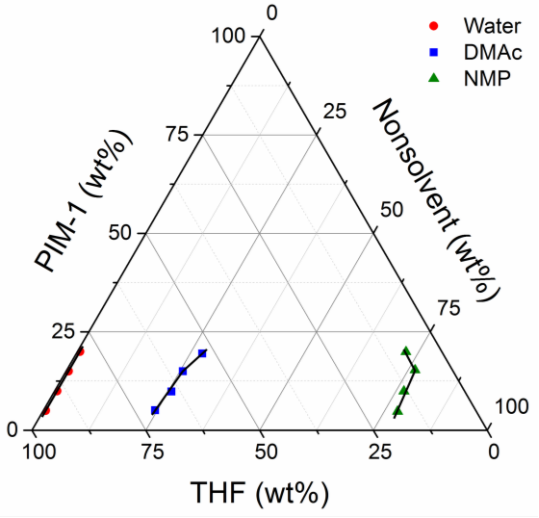

Figure 5.3 Ternary phase diagrams showing the binodal lines for three nonvolatile nonsolvents—PIM-1/THF/water (red circles), PIM-1/THF/DMAc (blue squares), and PIM-1/THF/NMP (green triangles).

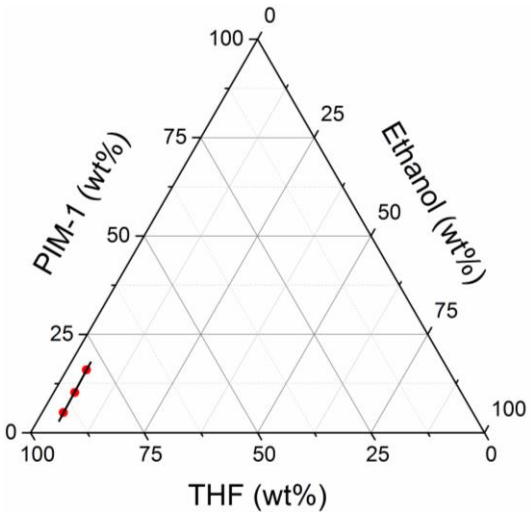

Figure 5.4 Ternary phase diagram showing the binodal line for the volatile nonsolvent PIM-1/THF/EtOH system.

DMAc is another amide used in spinning. Similar to NMP, DMAc also behaves as a weak nonsolvent for PIM-1; however, DMAc is a stronger nonsolvent than NMP for PIM-1 based on the ternary phase diagrams shown in Figure 5.3. Lastly, tetrahydropyran was investigated as a possible nonvolatile solvent for PIM-1 (Figure 5.5). However, it was

not used in actual spinning experiments due to its significantly reduced solvating power combined with poor water miscibility. A combination of 85 wt% to 15 wt% DMAc to EtOH was chosen as the final nonsolvent composition to create the desired ternary phase diagram shown by the red circles in Figure 5.2.

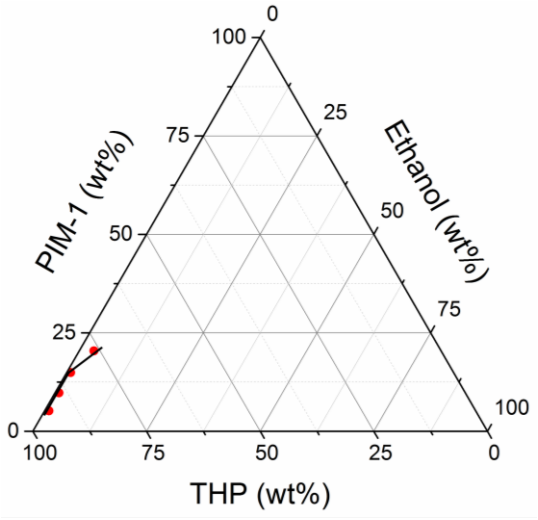

Figure 5.5 Ternary phase diagram for PIM-1/THP/EtOH.

Once the final dope composition was chosen, the composition of a neutral bore fluid was estimated from the intercept of the binodal line with the 0 wt% polymer axis. A slightly nonsolvent rich bore fluid was found to maintain round fibers without creating an internal skin layer and was used for most of the spins. The inclusion of hydrophilic additives such as polyvinylpyrrolidone (PVP) and lithium nitrate negatively affected the solubility of the spin dope. Even low concentrations of these additives—less than 5 wt%—caused previously one phase solutions to phase separate and were not considered for further spinning trials.

5.3.2 Bore Fluid Composition

The bore fluid composition contributes significantly to the spinability of round PIM-1 fibers. Nonsolvent-rich bore fluids are necessary to prevent fiber collapse during this PIM-1 spinning process. A wide range of mixtures were tested with each new spin dope to determine the most appropriate composition. Figure 5.6 highlights the effect of several different bore fluid compositions on the resulting fiber morphology. Using a purely nonsolvent bore fluid (Figure 5.6a) ensures that the fiber bore remains open during spinning. However, it can cause phase inversion to occur on the internal surface of the fiber—effectively creating a dual skinned hollow fiber. For gas separation applications, the presence of an internal skin layer is not highly beneficial and adds an additional transport resistance.

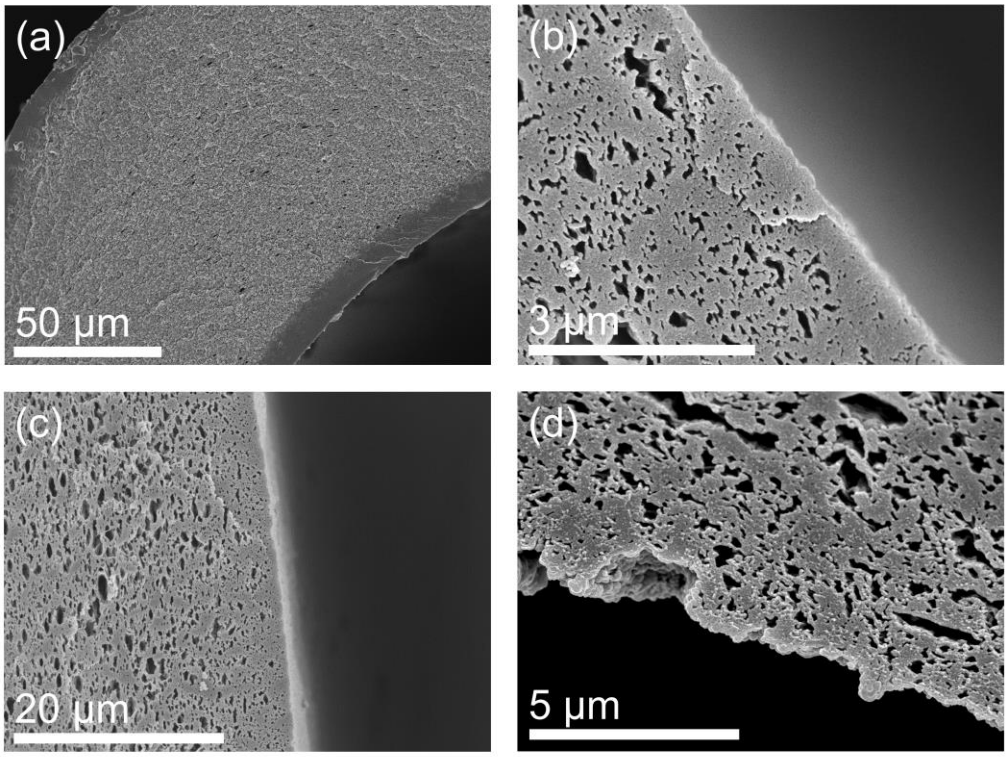

Figure 5.6 SEM images of PIM-1 fibers spun using different bore fluid compositions. (a) A fiber spun using 85/15 wt% DMAc/EtOH that produced an internal skin layer. (b) A fiber spun using 60.75/10.75/28.5 wt% DMAc/EtOH/THF bore fluid that produced a somewhat dense, but smooth internal layer. (c) A fiber spun using 46.75/8.25/45 wt% DMAc/EtOH/THF bore fluid with a smooth internal layer. (d) A fiber spun using 38.25/6.75/55 wt% DMAc/EtOH/THF with a rough internal layer.

The fibers shown in Figure 5.6 were spun from 17.5 wt% PIM-1 dopes and have a fairly dense substructure. Increasing the solvent content of the bore fluid up to nearly 50 wt% THF creates internal layers that are not significantly different in porosity than the surrounding substructure (Figure 5.6b and c). Once the bore fluid begins to become solvent-rich (Figure 5.6d), it begins dissolving the internal interface and creating a rough surface. Fibers also flatten in this regime of bore fluid composition.

5.3.3 Sheath Layer Composition

As previously discussed, the final spin dopes for PIM-1 consist mainly of the volatile solvent THF. Unlike conventional spin dopes that are mostly nonvolatile NMP, these THF dopes are much more difficult to work with due to rapid solvent evaporation in the air gap after leaving the spinneret. Spinning fibers using the dry jet, wet quench method creates flat, dense fibers with this dope composition as seen in Figure 5.7. The rapid solvent loss produces a thick (tens of micrometers) outer skin on the fiber that significantly slows the solvent/nonsolvent counter exchange in the water quench bath. As a result, solvent loss from the nascent fiber occurs into the bore fluid instead and the fiber flattens as a result. Air gaps lower than 1 mm did not circumvent this problem. Wet jet, wet quench spinning was not attempted to avoid phase inversion inside the spinneret.

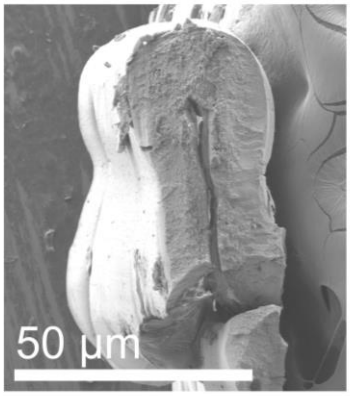

Figure 5.7 PIM-1 hollow fiber spun from a Spin 2 dope without a sheath layer.

To control the solvent flux in the air gap, an alternative spinning method was utilized. Using a triple orifice spinneret, a protective sheath layer was coextruded with the dope and bore fluid to simulate a dual-bath process without the need to modify the spinning line.[19] The presence of the sheath layer slows down the rate of solvent removal from the

nascent fiber and prevents a flash vitrification type formation of the skin layer. The composition and viscosity of the sheath layer also have a dramatic effect on the resulting fiber morphology as shown in Figure 5.8 and Figure 5.9. Pure NMP sheath layers (Figure 5.8a) slowly delaminate from the nascent fiber in the quench bath and produce irregular fibers. Increasing the viscosity of the sheath layer—via the introduction of the water soluble polymer PVP—only worsens this problem. These water soluble sheath layers form boundary layers with substantial mass transfer resistances around the nascent fiber during much of its time in the quench bath, leading to highly irregular fibers with contours shaped by liquid-liquid instabilities.

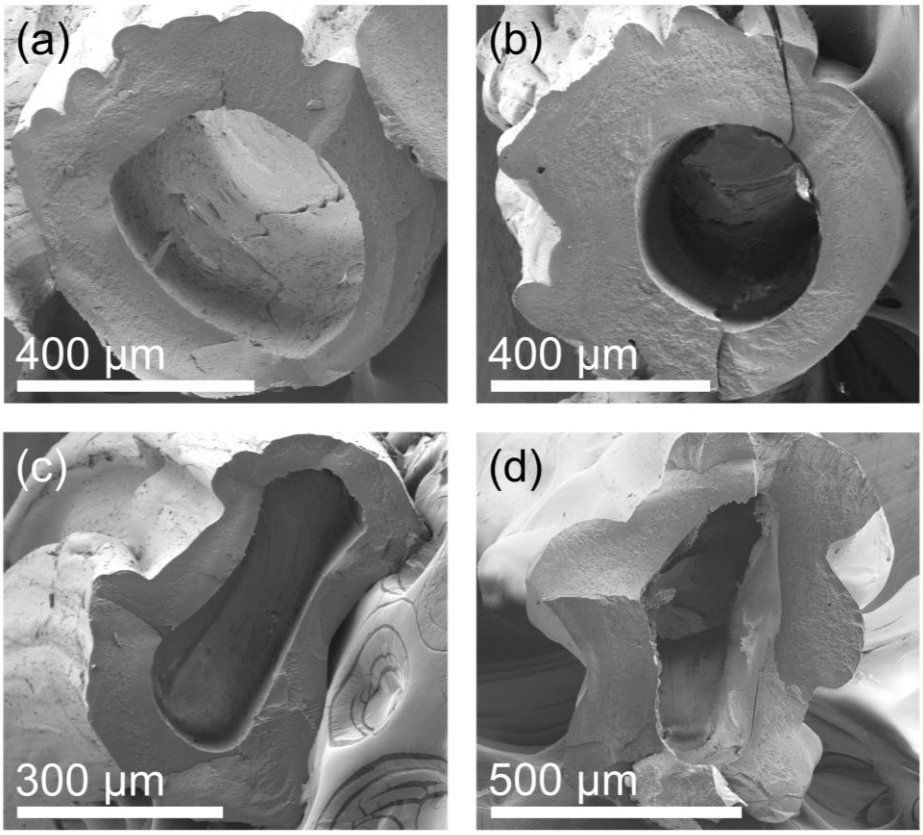

Figure 5.8 PIM-1 hollow fibers spun using sheath layers composed of (a) 100 wt% NMP, (b) 87.6/12.4 wt% NMP/PVP, (c) 69/31 wt% NMP/PVP, and (d) 37.3/44.5/18.2 wt% NMP/PVP/THF.

Utilizing an inviscid, water immiscible sheath fluid mitigates the issues encountered with the previous NMP sheath. Figure 5.9 shows fibers spun using 1-butanol sheath layers. The 1-butanol instantly and uniformly delaminates from the nascent fiber when it enters the water quench bath.[19,24] The fibers are smooth and round with the desired substructure. Even when the sheath layer is mostly THF by weight (Figure 5.9c and d) the 1-butanol delamination effect remains. It is likely that the majority of the THF remains with the 1-butanol sheath layer as the fiber enters the water quench bath rather than preferentially adhering to the fiber surface.

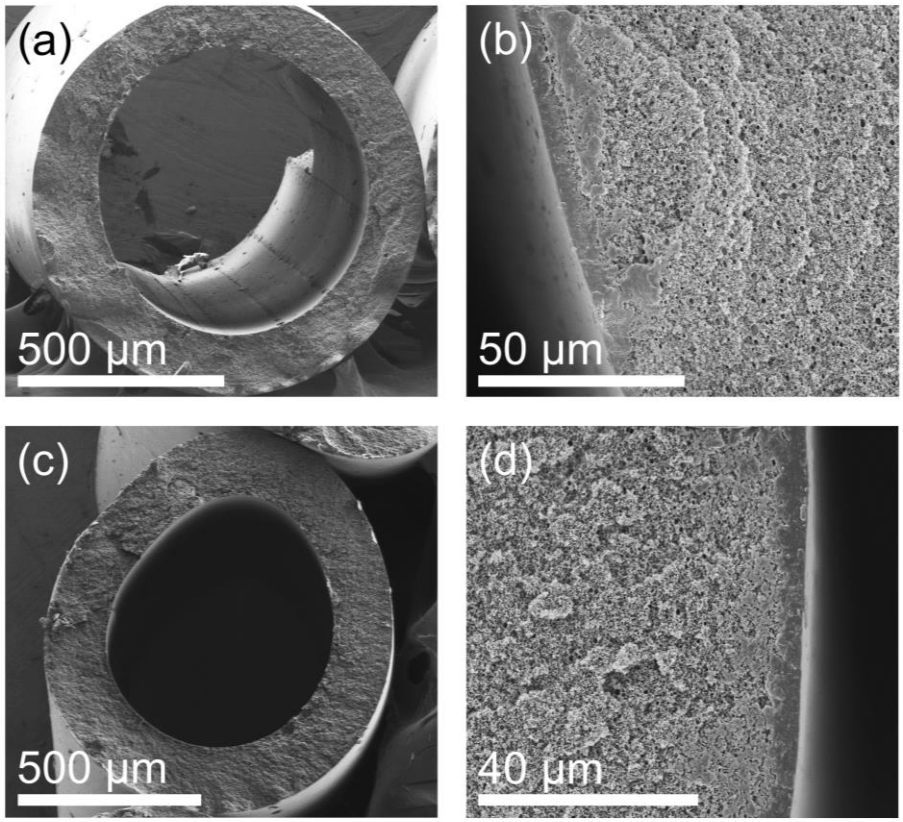

Figure 5.9 PIM-1 hollow fibers produced from (a) and (b) a 100 wt% 1-butanol sheath layer and (c) and (d) a 25/75 wt% 1-butanol/THF sheath layer.

5.3.4 Spin 1

1-Butanol was used as the sheath layer to produce the fibers in Spin 1 and the electron micrographs of the State S1 fibers are shown in Figure 5.10. The dope and spinning lines used in Spin 1 were kept at room temperature to minimize solvent loss from the dope before entering the water quench bath. The quench bath was kept at 50°C to promote exchange with the water and increase the rate of phase inversion. The resulting fibers spun with this sheath layer were round and much more mechanically robust than the previous fibers produced from the NMP-rich spin dopes. However, it is difficult to distinguish where the skin layer begins due to the relatively dense substructure that is seen throughout the State S1 fiber in Figure 5.10. Fibers from State S1 were not tested for gas

permeation due to the substantial anticipated substructure resistance based on electron microscopy analysis.

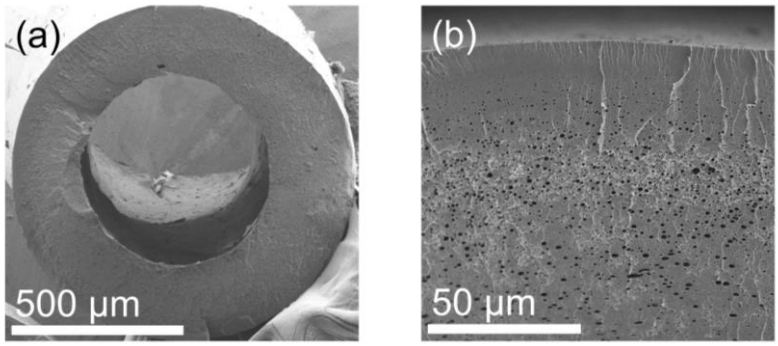

Figure 5.10 SEM images of (a) the cross section and (b) the skin layer and substructure of a PIM-1 hollow fiber produced from State S1 utilizing a pure 1-butanol sheath layer.

5.3.5 Spin 2

For the second illustrative spin, a less dense substructure was desired to achieve more practical membrane performance than what the State S1 fibers could likely provide. The already fairly low polymer concentration was lowered from 17.5 wt% to 15 wt% PIM-1 to avoid the development of dense substructures and 1-butanol was again used as the sheath. Lowering the polymer concentration in the dope consistently produces fibers with very porous substructures and clearly defined skin layers (as shown in the electron micrographs in Figure 5.11) regardless of changes to other parameters like draw ratios or bore fluid composition. The State S2 substructure shown in Figure 5.11 is indicative of (but does not confirm) spinodal decomposition of the dope in the water quench bath.

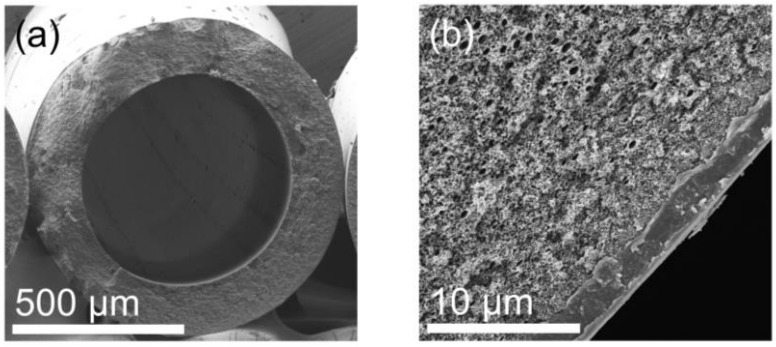

Figure 5.11 SEM images of (a) the cross section and (b) the skin layer and substructure of a PIM-1 hollow fiber produced from State S2 utilizing a pure 1-butanol sheath layer.

Mercury porosimetry was used to quantify the changes in pore structure as a result of changing the polymer concentration in the dope. Figure 5.12 shows the mercury intrusion plots for fibers from each spin. The State S2 fibers have a more porous and interconnected pore network compared to the State S1 fibers, as indicated by the higher and broader peak around 100 nm, which qualitatively agrees with microscopy analysis.

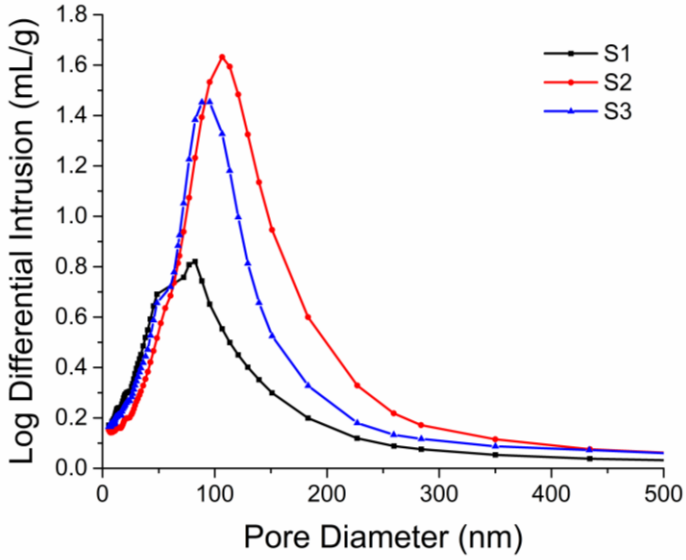

Figure 5.12 Mercury intrusion in the relatively dense State S1 fibers compared to the porous States S2 and S3 fibers.

Only a very narrow range of spinning parameters (air gaps, take up rates, etc.) were able to consistently produce round PIM-1 fibers from the Spin 2 dope. Within this small feasible working range, the skin layers produced were on the order of several micrometers thick as estimated from SEM images. The fibers from State S2 were tested with single component carbon dioxide and methane permeation to quickly assess the separation performance and quality of the skin layer. The permeances shown in Table 5.2 are significantly higher than expected based on SEM analysis of the skin layer thickness and the permeabilities reported for flat sheet PIM-1 membranes.[20,25,26] Moreover, these fibers exhibited a CO_2/CH_4 selectivity of 1.5—compared to a reported value of 15.4, indicative of somewhat defective fibers.[20] The fact that the fibers showed a greater selectivity than Knudsen diffusion (0.6) and in general greater than unity implies the presence of pinhole defects rather than prominent bulk defects. Pinhole defects are likely caused by the rapid loss of THF into the 1-butanol sheath layer while in the air gap. Due to this solvent loss, the nascent fibers quickly phase invert after entering the water quench bath, locking into place any defects in the skin layer. In essence, the THF removal rate in the air gap (where the PIM-1 solution contacts the 1-butanol sheath) is hypothesized to be high enough to result in nanoscopic defects that are then "frozen in" when the PIM-1 fiber contacts the water quench bath.

Table 5.2 Single component gas permeation results at 100 psig feed pressure and 35°C for a single State S2 PIM-1 fiber. The skin layer is estimated to be 5.8 µm thick based on SEM images. 1 GPU = 10^{-6} cm^3(STP) cm^{-2} s^{-1} $cmHg^{-1}$ and 1 Barrer = 10^{-10} cm^3(STP) cm cm^{-2} s^{-1} $cmHg^{-1}$ = 3.35 x 10^{-16} mol m m^{-2} s^{-1} Pa^{-1}.

CO_2 Permeance (GPU)	1500
Estimated CO_2 Permeability (Barrer)	8730
CH_4 Permeance (GPU)	1000
Estimated CH_4 Permeability	5790
CO_2/CH_4 Selectivity	1.5

5.3.6 Spin 3

In this simulated dual-bath spinning method, the sheath layer composition is the only accessible variable for adjusting the THF removal rate because of the low air gap height limitations for spinning PIM-1 (i.e., nascent PIM-1 fibers were not able to withstand the draw in the air gap). THF was therefore introduced into the sheath layer to slow the rate of THF extraction in the air gap where the skin layer is believed to form; as noted earlier, we hypothesized that reduction of the THF removal rate from the PIM-1 solution would lead to defect-free skin layer formation. Indeed, we observed that increasing the THF concentration in the 1-butanol sheath increased the resulting fiber's CO_2/CH_4 selectivity up to a maximum of 26 for the THF concentrations investigated in Figure 5.13. Sheath layers with THF concentrations greater than 15 wt% in 1-butanol produced fibers with similar separation performance, suggesting that defect-free skins are formed after a minimum THF loading. However, the further addition of THF significantly delays phase inversion in the air gap and causes the formation of skin defects due to the lack of vitrification before water-induced phase inversion in the quench bath.

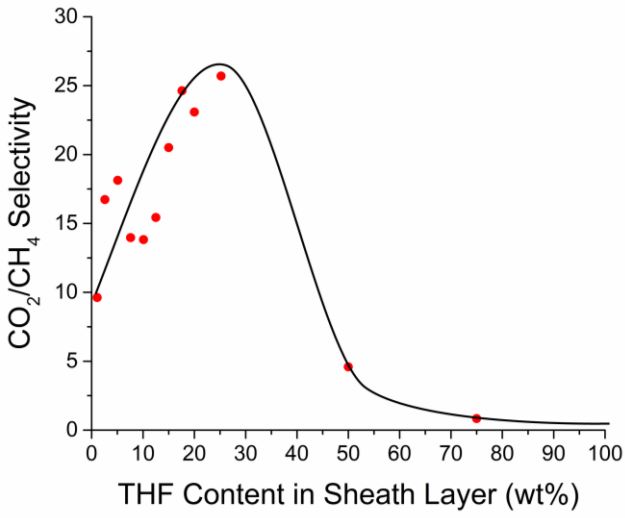

Figure 5.13 Effect of THF concentration in the 1-butanol sheath layer on the unaged fiber selectivity. Pure component gas permeation experiments were conducted on single fiber modules with a 100 psig feed pressure at 35°C. The black line is used to guide the eye.

The cross section and substructure of a defect-free State S3 PIM-1 hollow fiber is shown in Figure 5.14. Under electron microscopy, the fibers produced in Spin 3 with various amounts of THF in the sheath layer appear essentially identical to the fibers from Spin 2. The similar pore size distribution for the State S2 and S3 fibers shown in Figure 5.12 further indicates that the sheath composition does not significantly alter the final fiber morphology (provided that the sheath is immiscible with the quench bath).

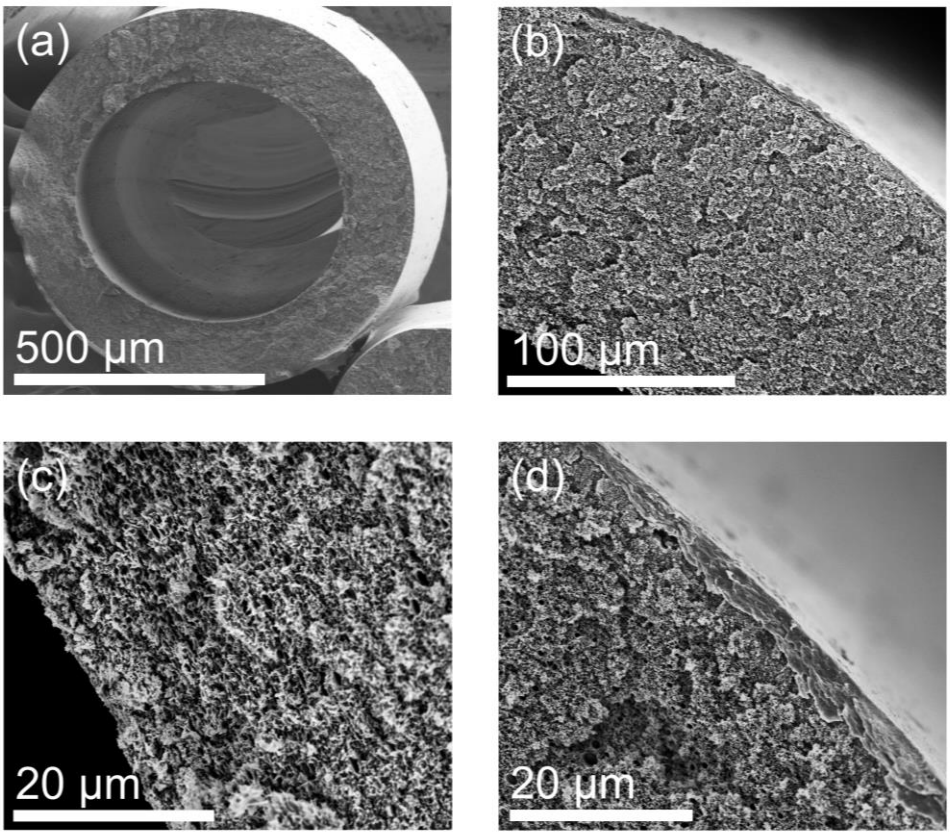

Figure 5.14 SEM images of a defect-free State S3 PIM-1 hollow fiber (a) cross section, (b) asymmetric substructure, (c) internal boundary, and (d) skin layer spun with a 17.5 wt% THF in 1-butanol sheath layer.

The selectivity of the State S3 fibers were measured using the same carbon dioxide and methane permeation experiments. As shown in Table 5.3, the State S3 fibers have a CO_2/CH_4 selectivity of 25 compared to 1.5 for the State S2 fibers. This high selectivity is from the defect-free PIM-1 fiber itself without the use of any PDMS top layer or other post-treatments. Given the large variation in reported gas permeabilities for PIM-1, SEM images were used to estimate the skin thickness. However, it is difficult to distinguish between the end of the porous substructure and the beginning of the skin layer based on visual inspection alone, which often results in overestimation of the size of the selective layer. The estimated carbon dioxide and methane permeabilities are much lower than of those

reported for dense PIM-1 membranes as a consequence. Regardless, the selectivity was in favorable agreement with reported values and the fibers from State S3 were used for further, more rigorous gas permeation testing.[20,25,26]

Table 5.3 Single component gas permeation results at 100 psig feed pressure and 35°C for a single State S3 PIM-1 fiber. The skin layer is estimated to be 2.8 µm thick based on SEM images. 1 GPU = 10^{-6} cm^3(STP) cm^{-2} s^{-1} $cmHg^{-1}$ and 1 Barrer = 10^{-10} cm^3(STP) cm cm^{-2} s^{-1} $cmHg^{-1}$ = 3.35 x 10^{-16} mol m m^{-2} s^{-1} Pa^{-1}.

CO_2 Permeance (GPU)	540
Estimated CO_2 Permeability (Barrer)	1500
CH_4 Permeance (GPU)	22
Estimated CH_4 Permeability	61
CO_2/CH_4 Selectivity	25

5.3.7 Gas Permeation

After spinning, solvent exchange, and drying, the fibers were allowed to age at ambient conditions for two months before gas permeation testing—well past the so-called "aging knee" that is particularly relevant for microporous membranes.[27] Testing aged fibers is more representative of the actual working performance of the membrane rather than their early-stage performance. Unlike dense films that are near their equilibrium packing everywhere, asymmetric membranes have a porous substructure due to the fast kinetics of the phase inversion process. Reversing the effects of aging and conditioning with nonplasticizing nonsolvents like methanol were not feasible for polymeric fibers already constructed into modules.[18] Significant nonsolvent-induced swelling could not be accommodated by the fibers once sealed in the module as the fibers broke upon subsequent

shrinkage during nonsolvent removal (we speculate that this could be a result of unrelaxed internal stresses created from the relatively rapid phase inversion during spinning). It is possible for more rigid thermally rearranged membranes to be regenerated with methanol while still assembled in a module as they do not swell to nearly the same extent as polymers.[28] Moreover, thermally annealing the PIM-1 fibers—which can remove pinhole defects in Matrimid® fibers and other (comparatively) low glass transition temperature polymers—did not have a significant effect on the selectivity due to the high glass transition temperature of PIM-1 (> 435°C).[29] Attempts to remove pinhole defects using high activity THF vapor yielded similarly poor results.

The aged fibers were constructed into single fiber modules and tested with various gases at 25, 35, and 45°C. The permeances for the State S3 fibers at 35°C are listed in Table 5.4 and compared to reported PIM-1 blend and other polyimide HFMs.[7,8,11,12] Similar data for the fiber permeances at 25 and 45°C are shown in Table 5.5. When measured against the unaged PIM-1/Matrimid® and PIM-1/Ultem® blend membranes, the aged State S3 fibers have higher permeances even with a substantially thicker skin layer (2.8 μm compared to 100 nm) due to the intrinsic high permeability of PIM-1. The State S3 fibers also have much higher permeances than the non-microporous polyimide HFMs Matrimid® and Torlon®. Even with performance loss due to aging, the PIM-1 HFMs still have permeances that exceed those of other polymeric HFMs that have been proposed for various gas separation applications.

Table 5.4 Pure component gas permeances for State S3 PIM-1 fibers and reported hollow fiber membranes. 1 GPU = 10^{-6} cm^3(STP) cm^{-2} s^{-1} $cmHg^{-1}$.

Gas	Permeance (GPU)				
	PIM-1[a]	PIM-1/Matrimid® (15:85)[b]	PIM-1/Ultem® (15:85)[c]	Matrimid®[d]	Torlon®[e]
Nitrogen	13 ± 2	9.9	2.24	2.7	$0.034 \pm 2x10^{-3}$
Methane	16 ± 3	7.1	1.70	-	$0.02 \pm 1x10^{-3}$
Argon	30 ± 5	-	-	-	-
Ethane	41 ± 10	-	-	-	-
Ethylene	58 ± 8	-	-	-	-
Oxygen	60 ± 10	59.9	13.02	18.1	0.26 ± 0.02
Helium	190 ± 40	-	-	243.5	7.4 ± 0.3
Hydrogen	350 ± 60	-	-	-	0.84 ± 0.05
Carbon Dioxide	360 ± 30	243.2	49	-	-

[a]Measured with a constant pressure system at 35°C and 100 psig feed pressure after two months of aging at ambient conditions. Skin layer thickness approximately 2.8 μm.
[b]Measured post solvent exchange and silicon rubber coating with a constant pressure system at 25°C and 14.7 psig feed pressure. Skin layer thickness less than 100 nm.[12]
[c]Measured post solvent exchange with a constant pressure system at 25°C and 43.5 psig feed pressure. Skin layer thickness 104 nm.[11]
[d]Measured post solvent exchange with a constant pressure system at 24°C and 50-100 psig feed pressure. Skin layer thickness 730 nm.[29]
[e]Measured post solvent exchange with a constant volume system at 35°C and greater than 200 psig feed pressures. Skin layer thickness 410 nm.[7]

Table 5.5 Tabulated gas permeances for State S3 PIM-1 hollow fibers at 100 psig feed pressure at 25 and 45°C.

Gas	Permeance at 25°C (GPU)	Permeance at 45°C (GPU)
Nitrogen	11 ± 2	15 ± 3
Methane	14 ± 3	20 ± 4
Argon	27 ± 4	34 ± 6
Ethane	35 ± 9	50 ± 10
Ethylene	52 ± 7	70 ± 10
Oxygen	50 ± 10	70 ± 10
Helium	170 ± 30	200 ± 40
Hydrogen	320 ± 50	370 ± 60
Carbon Dioxide	350 ± 20	370 ± 40

The ideal selectivities for the fibers given in Table 5.6. In general, the observed selectivities in our study are higher than those in previous works on dense films that focus on fundamental material characterization. This difference has been noted before for other glassy polymers and has been attributed to partial polymer chain alignment due to the high shear environment of the solution within the spinneret.[30,31] However, in our study it is difficult to deconvolute this effect from the tendency for ideal gas selectivity to increase somewhat with aging. It is important to note that plasticization effects potentially increased the observed permeances of carbon dioxide, ethane, and ethylene relative to the less condensable gases.

Table 5.6 Ideal selectivities relative to nitrogen for State S3 PIM-1 fibers and reported flat sheet membranes.

Gas	Selectivity (gas/N_2)			
	This work[a]	Li et al.[b]	Thomas et al.[c]	Budd et al.[d]
Methane	1.3	1.3	1.3	1.5
Argon	2.4	-	-	-
Ethane	3.3	2.3	4.4	-
Ethylene	4.6	4.2	-	-
Oxygen	4.9	3.4	3.8	3.4
Helium	15	4.8	4.4	4.8
Hydrogen	27	10	11	10
Carbon Dioxide	28	16	19	24

[a]Measured with a constant pressure system at 35°C and 100 psig feed pressure after two months aging at ambient conditions.
[b]Measured post methanol wash with a constant volume system at 35°C and 118 psig feed pressure.[26]
[c]Measured post methanol wash with a constant pressure system at 25°C and 65 psig feed pressure.[25]
[d]Measured post methanol wash with a constant volume system at 30°C and 2.9-4.4 psig feed pressure.[20]

The pure component permeances at various temperatures were used to calculate the activation energies of permeation for the defect-free PIM-1 HFMs. The values and fits are shown in Table 5.7 and Figure 5.15. It should be noted that these activation energy values are not directly comparable to reported dense film PIM-1 membranes due to the differences in the membranes (including morphology, aging, experimental conditions, etc.), but are still valuable for understanding the temperature dependence of permeation of PIM-1 in this new morphology. Similar to the permeation and selectivity data, the State S3 fibers have comparable activation energies of permeation with the same trends relative to the reported PIM-1 flat sheet membranes, although slightly higher values were observed in this work.

Table 5.7 Activation energies of permeation of State S3 PIM-1 fibers and reported flat sheet membranes.

Gas	Activation Energy of Permeation (kJ/mol)			
	This work[a]	Li et al.[b]	Thomas et al.[c]	Budd et al.[d]
Nitrogen	11.4 ± 0.7	11.9	14.3	10.5
Methane	15 ± 2	17.6	19.4	10.9
Argon	9.4 ± 0.2	-	-	-
Ethane	13.4 ± 0.5	-	-	-
Ethylene	10 ± 1	-	-	-
Oxygen	9.6 ± 0.5	2.6	5.6	3.3
Helium	7 ± 1	2.7	0.4	5.4
Hydrogen	4.9 ± 0.3	1.7	-0.4	3.2
Carbon Dioxide	3 ± 1	0.5	-1	-4.5

[a]Measured with a constant pressure system at 35°C and 100 psig feed pressure after two months aging at ambient conditions.
[b]Measured post methanol wash with a constant volume system at 35°C and 118 psig feed pressure.[26]
[c]Measured post methanol wash with a constant pressure system at 25°C and 65 psig feed pressure.[25]
[d]Measured post methanol wash with a constant volume system at 30°C and 2.9-4.4 psig feed pressure.[20]

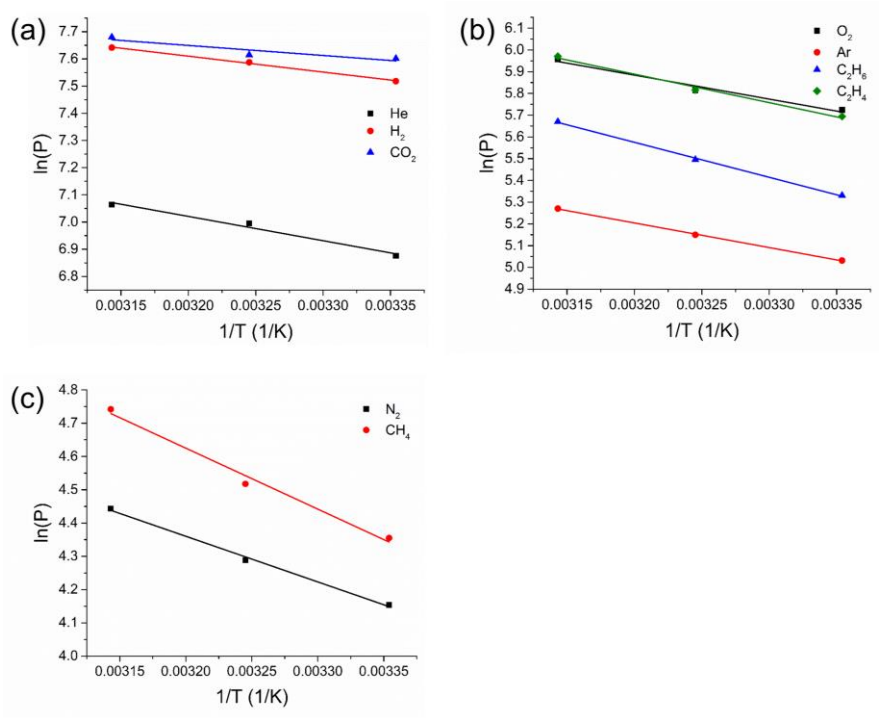

Figure 5.15 Linear regression plots for various gases in aged PIM-1 hollow fibers.

5.3.8 Additional Fiber Properties

Other fiber characteristics in addition to gas permeation were also probed. Nitrogen physisorption at 77 K was measured for both the neat PIM-1 powder and the State S3 fibers as shown in Figure 5.16. Forming PIM-1 into a fiber morphology slightly increased the BET surface area from 760 m^2/g to 800 m^2/g as shown in Table 5.8. Fibers are predominantly a porous, interconnected substructure that allows for additional nitrogen physisorption compared to the randomly phase inverted powder.

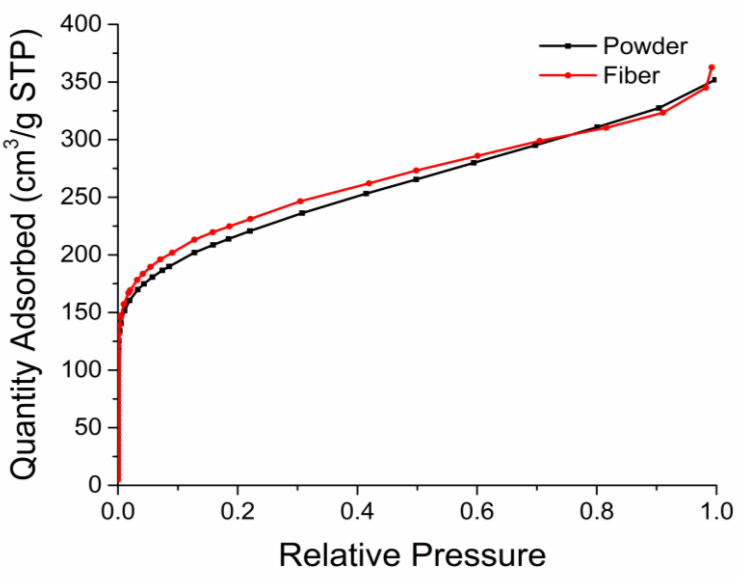

Figure 5.16 Nitrogen physisorption at 77 K of PIM-1 powder and State S3 PIM-1 hollow fibers.

Table 5.8 BET surface areas based on nitrogen physisorption at 77 K for PIM-1 powder and State S3 PIM-1 hollow fibers.

Sample	BET Surface Area (m^2/g)
Powder	760
Fiber	800

The PIM-1 fibers spun from all conditions were much more brittle than those made from other polymers such as cellulose acetate and various polyimides. Unlike those other polymers, the PIM-1 porous substructure is substantially more brittle and easily broken under shear stress than the dense skin layer (this can be inferred by the relative stability of a dense PIM-1 coupon). It is likely a combination of factors—including the relatively low

molecular weight of the polymer, the rigidity of the polymer structure, and the kinetically trapped internal strain caused by rapid phase inversion—contribute to the brittleness. Although the skin layer for these PIM-1 HFMs appears somewhat large compared to other HFMs—a few micrometers compared to a few hundred nanometers—the overall mechanical integrity should be considered before attempting to significantly thin down the skin layer further. It is possible that sub-micron thick skin layers would produce very high permeance fibers that are too fragile to use. However, these fairly thick skinned PIM-1 HFMs perform well under compressive stresses like those experienced during gas permeation applications once assembled into a module and still maintain high gas flux after aging.

5.4 Conclusions

The work here describes a method for spinning defect-free, integrally skinned, asymmetric PIM-1 hollow fiber membranes. A THF-based spin dope was developed that could be further adapted for use with other polymers having solubility limitations similar to those found with PIM-1 solutions. A 1-butanol/THF sheath layer was coextruded with the polymer dope to control solvent loss in the air gap and prevent fiber flattening or defective skin layer formation. Importantly, the presence of THF in the sheath layer was critical to control the THF removal rate from the nascent fibers, thus paving the way to defect-free fiber formation. The fibers were characterized and made into single-fiber modules. The pure component permeances, ideal selectivities, and activation energies of permeation were quantified for helium, hydrogen, oxygen, nitrogen, argon, carbon dioxide, methane, ethane, and ethylene at 25, 35, and 45°C. Although there is a large variation among previously reported permeabilities due to differences in experimental conditions,

the gas selectivities in this study are in good agreement with those reported for flat sheet PIM-1 membranes and are in fact slightly higher than the dense films. Mixed gas permeation experiments could be conducted to further characterize these membranes under more realistic feed conditions.

This work is a first step in developing more industrially relevant membrane morphologies using microporous polymers. PIM-1 is also the precursor for a wide range of other microporous materials, some of which are completely insoluble after modification.[32-38] The fibers fabricated here were not investigated for organic solvent separations due to the significant swelling of the polymer in these solutions. In particular, fibers already assembled into modules had difficulties in accommodating the substantial change in fiber length without introducing defects. To avoid these complications, the PIM-1 hollow fibers described here will be chemically converted to CMS that would otherwise be impossible to produce in an asymmetric hollow fiber morphology.

5.5 References

(1) McKeown, N. B.; Budd, P. M. Exploitation of Intrinsic Microporosity in Polymer-Based Materials. *Macromolecules* **2010**, *43*, 5163-5176.

(2) Carta, M.; Malpass-Evans, R.; Croad, M.; Rogan, Y.; Jansen, J. C.; Bernardo, P.; Bazzarelli, F.; McKeown, N. B. An Efficient Polymer Molecular Sieve for Membrane Gas Separations. *Science* **2013**, *339*, 303-307.

(3) Jimenez-Solomon, M. F.; Song, Q.; Jelfs, K. E.; Munoz-Ibanez, M.; Livingston, A. G. Polymer nanofilms with enhanced microporosity by interfacial polymerization. *Nat. Mater.* **2016**, *15*, 760-767.

(4) Ma, X.; Pinnau, I. A novel intrinsically microporous ladder polymer and copolymers derived from 1,1',2,2'-tetrahydroxy-tetraphenylethylene for membrane-based gas separation. *Polym. Chem.* **2016**, *7*, 1244-1248.

(5) Luo, S.; Wiegand, J. R.; Gao, P.; Doherty, C. M.; Hill, A. J.; Guo, R. Molecular origins of fast and selective gas transport in pentiptycene-containing polyimide membranes and their physical aging behavior, *J. Membrane Sci.* **2016**, *518*, 100-109.

(6) Membrane Technology. *Kirk-Othmer Encyclopedia of Chemical Technology*; Wiley: New Jersey, 2000.

(7) Kosuri, M. R.; Koros, W. J. Defect-free asymmetric hollow fiber membranes from Torlon®, a polyamide-imide polymer, for high-pressure CO_2 separations. *J. Membrane Sci.* **2008**, *320*, 65-72.

(8) Clausi, D. T.; Koros, W. J. Formation of defect-free polyimide hollow fiber membranes for gas separations. *J. Membrane Sci.* **2000**, *167*, 79-89.

(9) Bernard, P.; Drioli, E.; Golemme, G. Membrane Gas Separation: A Review/State of the Art. *Ind. Eng. Chem. Res.* **2009**, *48*, 4638-4663.

(10) Feng, C. Y.; Khulbe, K. C.; Matsuura, T.; Ismail, A. F. Recent progresses in polymeric hollow fiber membrane preparation, characterization and applications. *Sep. Purif. Technol.* **2013**, *111*, 43-71.

(11) Hao, L.; Zuo, J.; Chung, T.-S. Formation of Defect-Free Polyetherimide/PIM-1 Hollow Fiber Membranes for Gas Separation. *AIChE J.* **2014**, *60*, 3848-3858.

(12) Yong, W. F.; Li, F. Y.; Xiao, Y. C.; Chung, T. S.; Tong, Y. W. High performance PIM-1/Matrimid hollow fiber membranes for CO_2/CH_4, O_2/N_2 and CO_2/N_2 separation. *J. Membrane Sci*. **2013**, *443*, 156-169.

(13) Lau, C. H.; Nguyen, P. T.; Hill, M. R.; Thorton, A. W.; Konstas, K.; Doherty, C. M.; Mulder, R. J.; Bourgeois, L.; Liu, A. C. Y.; Sprouster, D. J.; Sullivan, J. P.; Bastow, T. J.; Hill, A. J.; Gin, D. L.; Noble, R. D. Ending Aging in Super Glassy Polymer Membranes. *Angew. Chem. Int. Edit*. **2014**, *53*, 5322-5326.

(14) Koschine, T.; Raetzke, K.; Faupel, F.; Khan, M. M.; Emmler, T.; Filiz, V.; Abetz, V.; Ravelli, L.; Egger, W. Correlation of Gas Permeation and Free Volume in New and used High Free Volume Thin Film Composite Membranes. *J. Polym. Sci. Pol. Phys*. **2015**, *53*, 213-217.

(15) Yong, W. F.; Kwek, K. H. A.; Liao, K.-S.; Chung, T. S. Suppression of aging and plasticization in highly permeable polymers. *Polymer* **2015**, *77*, 377-386.

(16) Mitra, T.; Bhavsar, R. S.; Adams, D. J.; Budd, P. M.; Cooper, A. I. PIM-1 mixed matrix membranes for gas separations using cost-effective hypercrosslinked nanoparticle fillers. *Chem. Commun*. **2016**, *52*, 5581-5584.

(17) Bushell, A. F.; Budd, P. M.; Attfield, M. P.; Jones, J. T. A.; Hasell, T.; Cooper, A. I.; Bernardo, P.; Bazzarelli, F.; Clarizia, G.; Jansen, J. C. Nanoporous Organic Polymer/Cage Composite Membranes. *Angew. Chem. Int. Edit*. **2013**, *52*, 1253-1256.

(18) Jue, M. L.; McKay, C. S.; McCool, B. A.; Finn, M.G.; Lively, R. P. Effect of Nonsolvent Treatments on the Microstructure of PIM-1. *Macromolecules* **2015**, *48*, 5780-5790.

(19) Wienk, I. M.; Teunis, H. A.; Boomgaard, T.v.d.; Smolders, C. A. A new spinning technique for hollow fiber ultrafiltration membranes. *J. Membrane Sci*. **1993**, *78*, 93-100.

(20) Budd, P. M.; McKeown, N. B.; Ghanem, B. S.; Msayib, K. J.; Fritsch, D.; Starannikova, L.; Belov, N.; Sanfirova, O.; Yampolskii, Y.; Shantarovich, V. Gas permeation parameters and other physicochemical properties of a polymer of intrinsic microporosity: Polybenzodioxane PIM-1. *J. Membrane Sci*. **2008**, *325*, 851-860.

(21) Swaidan, R.; Ghanem, B.; Litwiller, E.; Pinnau, I. Physical Aging, Plasticization and Their Effects on Gas Permeation in "Rigid" Polymers of Intrinsic Microporosity. *Macromolecules* **2015**, *48*, 6553-6561.

(22) Vu, D. Q.; Koros, W. J.; Miller, S. J. High Pressure CO_2/CH_4 Separation Using Carbon Molecular Sieve Hollow Fiber Membranes. *Ind. Eng. Chem. Res*. **2002**, *41*, 367-380.

(23) Sanders, D. F.; Smith, Z. P.; Guo, R.; Robeson, L. M.; McGrath, J. E.; Paul, D. R.; Freeman, B. D. Energy-efficient polymeric gas separation membranes for a sustainable future: A review. *Polymer* **2013**, *54*, 4729-4761.

(24) Li, S. G.; Koops, G. H.; Mulder, M. H. V.; Boomgaard, T.v.d.; Smolders, C. A. Wet spinning of integrally skinned hollow fiber membranes by a modified dual-bath coagulation method using a triple orifice spinneret. *J. Membrane Sci*. **1994**, *94*, 329-340.

(25) Thomas, S.; Pinnau, I.; Du, N.; Guiver, M. D. Pure- and mixed-gas permeation properties of a microporous spirobisindane-based ladder polymer (PIM-1). *J. Membrane Sci*. **2009**, *333*, 125-131.

(26) Li, P.; Chung, T. S.; Paul, D. R. Temperature dependence of gas sorption and permeation in PIM-1. *J. Membrane Sci*. **2014**, *450*, 380-388.

(27) Swaidan, R.; Al-Saeedi, M.; Ghanem, B.; Litwiller, E.; Pinnau, I. Rational Design of Intrinsically Ultramicroporous Polyimides Containing Bridgehead-Substituted Triptycene for Highly Selective and Permeable Gas Separation Membranes. *Macromolecules* **2014**, *47*, 5104-5114.

(28) Brunetti, A.; Cersosimo, M.; Dong, G.; Woo, K. T.; Lee, J.; Kim, J. S.; Lee, Y. M.; Drioli, E.; Barbieri, G. In situ restoring of aged thermally rearranged gas separation membranes. *J. Membrane Sci*. **2016**, *520*, 671-678.

(29) Zhou, F.; Koros, W. J. Study of thermal annealing on Matrimid® fiber performance in pervaporation of acetic acid and water mixtures. *Polymer* **2006**, *47*, 280-288.

(30) Chung, T. S.; Lin, W. H.; Vora, R. H. The effect of shear rates on gas separation performance of 6FDA-durene polyimide hollow fibers. *J. Membrane Sci*. **2000**, *167*, 55-66.

(31) Lively, R. P.; Dose, M. E.; Xu, L.; Vaughn, J. T.; Johnson, J. R.; Thompson, J. A.; Zhang, K.; Lydon, M. E.; Lee, J.-S.; Liu, L.; Hu, Z.; Karvan, O.; Realff, M. J.; Koros, W. J. A high-flux polyimide hollow fiber membrane to minimize footprint and energy penalty for CO_2 recovery from flue gas. *J. Membrane Sci*. **2012**, *423–424*, 302-313.

(32) Mason, C. R.; Maynard-Atem, L.; Al-Harbi, N. M.; Budd, P. M.; Bernardo, P.; Bazzarelli, F.; Clarizia, G.; Jansen, J. C. Polymer of Intrinsic Microporosity Incorporating Thioamide Functionality: Preparation and Gas Transport Properties. *Macromolecules* **2011**, *44*, 6471-6479.

(33) Du, N.; Park, H. B.; Robertson, G. P.; Dal-Cin, M. M.; Visser, T.; Scoles, L.; Guiver, M. D. Polymer nanosieve membranes for CO2-capture applications. *Nat. Mater.* **2011**, *10*, 372-375.

(34) Du, N.; Robertson, G. P.; Song, J.; Pinnau, I.; Guiver, M. D. High-Performance Carboxylated Polymers of Intrinsic Microporosity (PIMs) with Tunable Gas Transport Properties. *Macromolecules* **2009**, *42*, 6038-6043.

(35) Patel, H. A.; Yavuz, C. T. Noninvasive functionalization of polymers of intrinsic microporosity for enhanced CO_2 capture. *Chem. Commun.* **2012**, *48*, 9989-9991.

(36) Du, N.; Robertson, G. P. Dal-Cin, M. M.; Scoles, L.; Guiver, M. D. Polymers of intrinsic microporosity (PIMs) substituted with methyl tetrazole. *Polymer* **2012**, *53*, 4367-4372.

(37) Mason, C. R.; Maynard-Atem, L.; Heard, K. W. J.; Satilmis, B.; Budd, P. M.; Friess, K.; Lanc, M.; Bernardo, P.; Clarizia, G.; Jansen, J. C. Enhancement of CO_2 Affinity in a Polymer of Intrinsic Microporosity by Amine Modification. *Macromolecules* **2014**, *47*, 1021-1029.

(38) Salinas, O.; Ma, X.; Litwiller, E.; Pinnau, I. Ethylene/ethane permeation, diffusion and gas sorption properties of carbon molecular sieve membranes derived from the prototype ladder polymer of intrinsic microporosity (PIM-1). *J. Membrane Sci.* **2016**, *504*, 133-140.

CHAPTER 6. NONSOLVENT CONDITIONING OF PIM-1

Defect-free polymeric membranes are critically necessary to reliably fabricate defect-free CMS membranes for OSRO. Although spinning defect-free PIM-1 hollow fiber membranes is indeed possible, the reproducibility of the process can be further improved via the use of post-treatments after spinning. The use of various nonsolvents to condition PIM-1 is studied and applied to heal defects in pre-fabricated membranes.

Parts of this work are adapted from 'Jue, M. L.; McKay, C. S.; McCool, B. A.; Finn, M. G.; Lively, R. P. Effect of Nonsolvent Treatments on the Microstructure of PIM-1. *Macromolecules* **2015**, *48*, 5780-5790.' with permission of the American Chemical Society and from 'Jue, M. L.; Breedveld, V.; Lively, R. P. Defect-free PIM-1 hollow fiber membranes. *J. Membrane Sci.* **2017**, *530*, 33-41.' with permission of Elsevier B. V.

6.1 Introduction

PIMs and other high free volume polymers are highly susceptible to the effects of aging and conditioning. Membrane aging is characterized by a (sometimes severe) decrease in the permeance and a (typically marginal) increase in the selectivity with time after membrane formation. Conditioning relates to changes in the membrane's performance due to external stimuli such as exposure to water or thermal annealing. The effects of aging and conditioning can be difficult to deconvolute depending on the relative rates of these two phenomena and the processing history of the membrane. These effects are particularly pronounced for materials such as PIMs that have significant initial fractional free volume. Excess free volume between polymer chains arise from non-equilibrium packing defects

as polymers are cooled below their glass transition temperature (T_g). The concentration and nature of these free volume elements have been successfully used to describe the sorption, diffusion, and permeation of guest molecules through glassy polymers.[1-3] After membrane formation, PIM-1 naturally begins to lose some of its excess free volume due to slow relaxations of the polymer chains towards their equilibrium packing. Lau et al. have shown that the CO_2 permeability of PIM-1 decreases by 62% over a period of eight months storage at ambient conditions.[4] However, not all of the free volume was lost and microporosity remained within the polymer even after a year under ambient storage.[5] Moreover, PIMs are unusual linear polymers because they do not exhibit a measureable T_g before decomposition.[6] As a result, near-T_g annealing techniques used to alter the polymer microstructure cannot be practically utilized. Near-T_g annealing is a common technique used in membrane fabrication and testing to ensure more uniform experimental processing histories, thus allowing researchers to draw meaningful conclusions when comparing different data sets.

Indeed, the sensitivity of the membrane to its processing history is a crucial factor in evaluating the material's performance. The prior history of glassy polymers can have significant effects on the membrane's properties and guest sorption behavior.[7,8] This also applies to PIMs, as the permeability of PIM-1 membranes is susceptible to conditioning via interactions with nonsolvents. For example, PIM-1 films cast from chloroform have a carbon dioxide permeability of 4416 Barrer and selectivity of 24.2 relative to nitrogen.[9] When water is used to help delaminate the film from the casting plate, the dried film has a 65% lower CO_2 permeability with a similar selectivity.[9] Methanol treatments have been used to remove variability (such as casting solvent, age, thermal treatment, etc.) in

subsequent membrane testing and characterization experiments. Before testing, comparable membranes were soaked in methanol for several hours, completely dried, and then tested. The methanol-conditioned PIM-1 film had the highest CO_2 permeability of the membranes studied at 12,440 Barrer ($\alpha_{CO2/N2}$ = 25.5) with similar processing history trends remaining evident for all gas pairs tested.[9]

Especially for high free volume polymers like PIMs, this methanol treatment step is believed to both remove residual trapped solvents within the microstructure as well as erase the past processing history. The effects of methanol conditioning on poly(1-trimethylsilyl-1-propyne) (PTMSP), the highest free volume hydrocarbon backbone polymer known to date, has also been studied.[10] While the initial increase (and subsequent decrease) in gas permeability post-methanol treatment has been well documented in PIM-1 and PIM derivatives—indeed, Seong et al. have shown that microporous polyimide membranes have increased gas sorption, diffusion, and permeation after methanol treatments[11]—few studies have investigated the methanol treatment process itself in great detail. This work investigates nonsolvent conditioning of PIM-1 membranes, with emphasis on understanding methanol treatments to remove past processing history and exploiting that understanding to create DMF-based defect treatments.

6.2 Experimental

6.2.1 Materials

ACS grade *N,N*-dimethylformamide (DMF), methanol, acetone, and diethyl ether were used as received (VWR or Alfa Aesar). Ultra high purity (UHP) grade carbon dioxide and methane for gas permeation studies were supplied by Airgas.

6.2.2 Synthesis and Fabrication of PIM-1 Hollow Fiber Membranes

PIM-1 powders and films used for conditioning and physisorption experiments were synthesized as described elsewhere.[12] The fabrication of PIM-1 hollow fiber membranes for defect treatments and gas permeation follows the procedure outlined previously.[13]

6.2.3 Nitrogen Physisorption

BET surface area measurements on conditioned PIM-1 were obtained from nitrogen physisorption experiments at 77 K using an ASAP 2020 (Micromeritics). Newly-cast films ("as-cast" films) were tested without methanol treatment. "DMF-conditioned" films were soaked in DMF for 24 hours and then wiped dry before being completely dried during degassing. "Methanol-conditioned" films were soaked in DMF for 24 hours, rinsed with methanol, soaked in methanol for 24 hours, and wiped dry before being completely dried during degassing. All other samples tested used as-synthesized PIM-1 powder soaked in the nonsolvent of choice for 24 hours, which was subsequently decanted and completely dried during degassing. Before analysis, all samples were degassed at 115°C for 12 hours to completely dry the sample (as quantified and confirmed by separate TGA analysis). The maximum pore volumes were determined at $p/p^0 = 0.99$ of the isotherm.

6.2.4 Thermogravimetric Analysis

Nonsolvent removal from conditioned PIM-1 films was conducted using thermogravimetric analysis under nitrogen (TGA Q500, TA Instruments). The as-cast film was fabricated from THF and then stored at ambient conditions prior to analysis. The DMF-

conditioned film was soaked in DMF for 24 hours, wiped dry, and kept at ambient conditions for several hours before analysis. The methanol-conditioned film was soaked in DMF for 24 hours, rinsed with methanol, soaked in methanol for 24 hours, wiped dry, and kept at ambient conditions for several hours before analysis. This was used to confirm methanol's ability to remove residual trapped DMF from PIM-1. The temperature program consisted of a 10°C/min ramp to 100°C, a 1 hour hold at 100°C drying step to remove any sorbed species, and a 10°C/min ramp to 1000°C.

6.2.5 Fiber Swelling Measurements

Changes to the hollow fiber length and skin layer thickness were used to quantify any macroscopic changes due to the defect treatments. Dry fibers were first measured with a ruler and then soaked in DMF/deionized water solutions ranging from 0 to 100 wt% DMF for 24 hours. Next, the wet fibers were measured again to determine the degree of nonsolvent-induced swelling. The wet fibers were then dried under vacuum at 80°C overnight before being measured a final time to determine any permanent fiber shrinkage after post-treatment. Changes to the skin thickness were assessed via SEM. All swelling calculations were referenced against the initial dry fiber lengths.

6.2.6 Scanning Electron Microscopy

SEM images of hollow fiber membranes were taken using a Hitachi SU8230 FE-SEM with a cold field emission gun at 5 kV accelerating voltage and 20 μA emission current. Samples were sputtered using a Hummer 6 Gold/Palladium Sputterer. ImageJ image processing software was used to estimate the fiber dimensions based on SEM images.

6.2.7 Defect Treatments

"Defect-treated" fibers were completely immersed in various DMF/deionized water solutions at ambient conditions before being removed and immediately dried in an 80°C vacuum oven. Both the soak time and drying time for each sample were controlled as specified later in the text. Fibers dried overnight were dried for a minimum of 12 hours. "Methanol-exchanged" fibers were soaked in a 50 wt% DMF aqueous solution for 24 hours, solvent exchanged in methanol three times (at 20 minute intervals), then dried in an 80°C vacuum oven. "Ambient condition" fibers were soaked in a 50 wt% DMF aqueous solution for 24 hours before drying at ambient conditions for 10 days. All defect-treated fibers were from the same set of slightly defective fibers to ensure consistency among the initial sample population.

6.2.8 Gas Permeation

Single hollow fiber membranes were assembled into modules and tested for gas permeation as described previously.[13] Pure component carbon dioxide and methane permeabilities at 100 psig and 35°C were used to assess the quality of the membranes.

6.3 Results and Discussion

6.3.1 Nonsolvent Evaporation Rate

Nonsolvent conditioning can be utilized to manipulate the microstructure of PIM-1. One important parameter is the evaporation rate of the nonsolvent after it has been introduced to the polymer. To investigate the effect of nonsolvent evaporation rate on the PIM-1 microstructure, two different DMF-conditioned PIM-1 powders were analyzed with

nitrogen physisorption. PIM-1 powders, rather than films or membranes, were used since they offer less mass transfer resistance to nitrogen physisorption experiments. The trends seen with conditioned PIM-1 powders are equivalent to PIM-1 dense films, only the magnitude of the calculated properties are slightly offset. In general, the powder samples have higher surface areas and pore volumes than the corresponding dense films due to the irregular morphology induced from the phase inversion process. The "fast" DMF-conditioned sample in Figure 6.1 was soaked in DMF, vacuum filtered, and completely dried during the degas step—115°C under $1x10^{-6}$ torr vacuum—in the nitrogen physisorption apparatus. The "slow" DMF-conditioned sample was soaked in DMF and completely dried in a vacuum oven—80°C under 36 torr—before being degassed under the same conditions in the nitrogen physisorption apparatus. The main difference between the two samples is that the slow DMF-conditioned sample was exposed to a saturated DMF environment while evacuating the nonsolvent from the polymer for much longer than the fast DMF-conditioned sample. As will be shown later, TGA analysis confirms that there is no residual DMF in the PIM-1 during the nitrogen physisorption analysis (the pre-analysis drying step removes all the DMF in both the fast and slow conditioning steps). Changing the nonsolvent evaporation rate alone considerably alters the surface area and pore volumes of the two DMF-conditioned samples. The fast DMF-conditioned sample had a 28% greater surface area and 20% greater pore volume relative to the slow DMF-conditioned sample as shown in Table 6.1. Although the fast DMF-conditioned sample had a much higher surface area and pore volume than the slow DMF-conditioned sample, both DMF-conditioned samples had lower porosities than the corresponding methanol-conditioned PIM-1 powder. Although not shown, the slow DMF-conditioned sample had a lower

surface area and pore volume than the as-synthesized PIM-1 powder. The slow evaporation of a high boiling, plasticizing nonsolvent like DMF results in the lowest surface areas and pore volumes measured for any sample in this study because it allowed the most time for the mobilized polymer chains to pack towards their equilibrium packing. It is important to note that a slow DMF-conditioning treatment (and subsequent removal of the DMF) could be used to accelerate the apparent aging process of dense PIM-1 membranes towards their equilibrium packing.

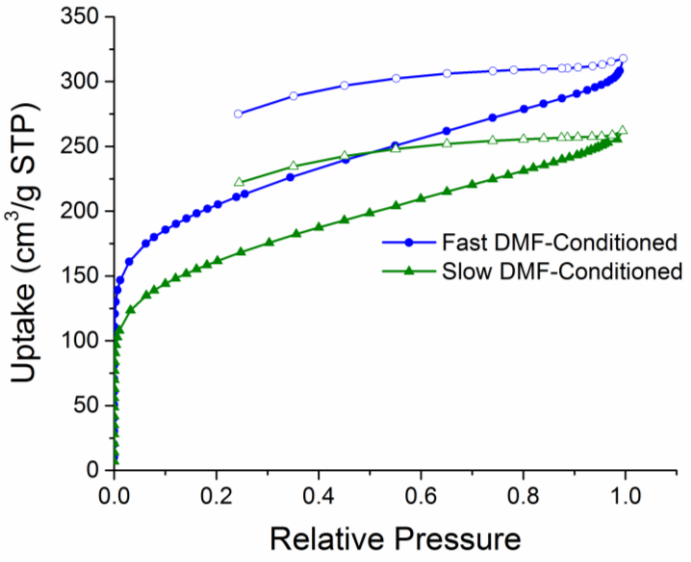

Figure 6.1 Nitrogen physisorption at 77 K in PIM-1 powders conditioned with differing DMF removal rates. The fast DMF-conditioned sample was soaked in DMF, vacuum filtered, and completely dried during degas at 115°C under $1x10^{-6}$ torr vacuum. The slow DMF-conditioned sample was soaked in DMF, completely dried in a vacuum oven at 80°C under 36 torr vacuum, and then degassed under the same conditions.

Table 6.1 BET surface area and pore volume of different DMF-conditioned PIM-1 powders as determined by nitrogen physisorption at 77 K.

Sample	BET Surface Area (m^2/g)	Pore Volume (cm^3/g)
Fast DMF-Conditioned	730	0.49
Slow DMF-Conditioned	570	0.41

A rough estimate of the DMF and methanol evaporation rates from PIM-1 can be determined from the weight change over time data obtained from the gravimetric sorption apparatus during the pre-analysis drying step.[12] Nonsolvent evaporation begins immediately after the sample is removed from the liquid and results in some unavoidable loss while loading the instrument. The normalized mass loss for each sample is shown in Figure 6.2 during the 1°C/min temperature ramp from 25 to 115°C under flowing nitrogen. Even under these changing conditions, the drastic difference in evaporation rates between the two nonsolvents is evident. The methanol-conditioned film lost essentially all of the sorbed methanol in approximately 250s (or about 5 mins). The DMF-conditioned film desorbed approximately 90% of the sorbed DMF at 2500s (or about 40 mins). The DMF loaded PIM-1 film needed around an hour at elevated temperatures to completely desorb the DMF (separately confirmed using TGA). The slower DMF nonsolvent evaporation rate, coupled with DMF-induced plasticization of the PIM-1 matrix, allows ample time for the chains to reorient themselves in the matrix and thereby reduce its fractional free volume.

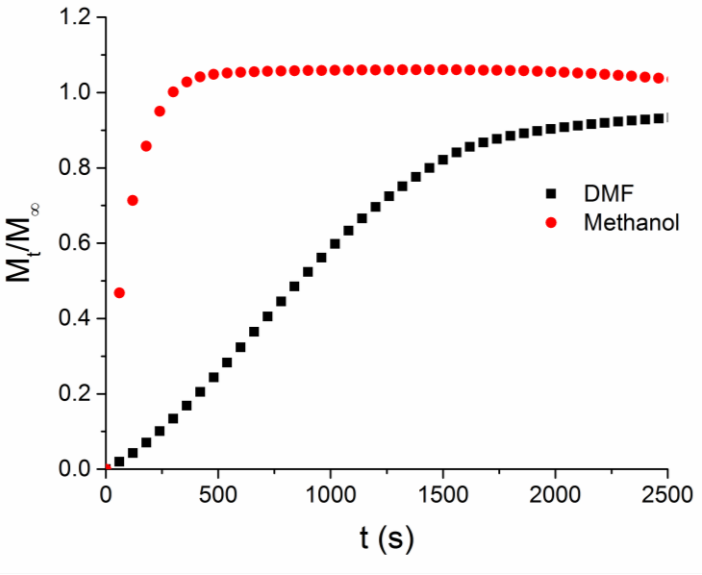

Figure 6.2 Normalized mass loss during in-situ, pre-analysis drying of methanol-conditioned and DMF-conditioned PIM-1 films. Data shown are during the 1°C/min ramp from 25 to 115°C under flowing dry nitrogen. The methanol-conditioned film was soaked in methanol for 24 hours before in-situ drying. The DMF-conditioned film was soaked in methanol for 24 hours then soaked in DMF for 24 hours before in-situ drying.

In essence, the nonsolvent evaporation rate can be thought of as analogous to the thermal quench rate after thermal annealing for glassy polymers, but with the added complication of highly non-ideal polymer-penetrant interactions. Moreover, the rate of volume relaxation of the polymer post-annealing—whether thermal or via nonsolvent desorption—is highly dependent on the state of the polymer (glassy or rubbery) during annealing.[7,14] In the case of PIM-1 soaked in methanol, PIM-1 is in a glassy state and essentially possesses very little segmental mobility during a rapid quench (relative to a rubber). For PIM-1 soaked in DMF, the PIM-1 is in a rubbery state (plasticization onset occurs at DMF saturation of ~0.55)[12] and possesses significant segmental mobility during a slow quench and thus the volume relaxation will be more significant. Sealed pan DSC

measurements should confirm that DMF-loaded PIM-1 is in a rubbery state, but these experiments are not available in the current study.

6.3.2 Nonsolvent Choice

Nitrogen physisorption was used to probe the microstructure and further understand nonsolvent conditioning in PIM-1. Figure 6.3 and Table 6.2 show isotherms and corresponding calculated BET surface areas and pore volumes. The as-cast film from THF and the DMF-conditioned film have similar isotherms since each sample was exposed to an organic that has very favorable interactions with PIM-1. Even though THF has a much higher vapor pressure than DMF, the two samples have similar surface areas, 600 and 650 m^2/g, respectively, and the same pore volume within error. For the as-cast film, the THF from film casting was very slowly evaporated from the PIM-1 films under nearly THF-saturated conditions, dried under ambient conditions to complete dryness (as separately confirmed by TGA), and then exposed to the degassing protocol in the nitrogen physisorption apparatus. The DMF-conditioned sample was vacuum filtered then immediately degassed in the physisorption unit; in essence, the evaporation rates of DMF and THF in this set of experiments are more similar than would normally be expected.

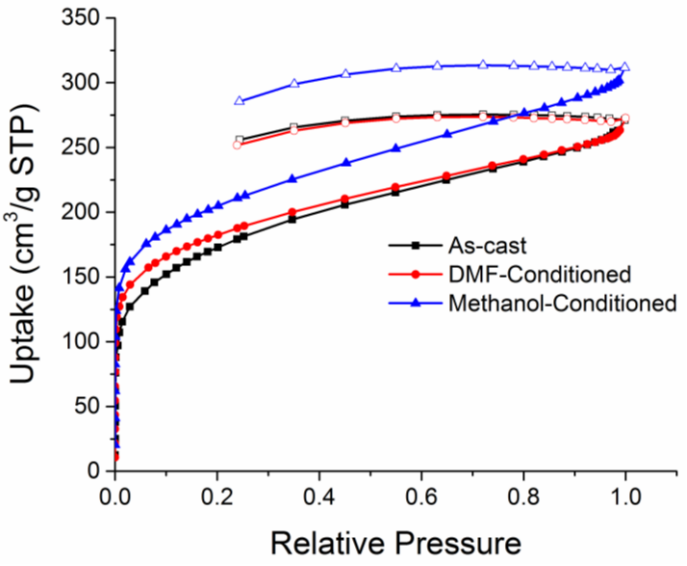

Figure 6.3 Nitrogen physisorption at 77 K in as-cast (black squares), DMF-conditioned (red circles), and methanol-conditioned (blue triangles) dense PIM-1 films.

Table 6.2 BET surface areas and pore volumes for PIM-1 films determined from nitrogen physisorption at 77 K.

Film	BET Surface Area (m^2/g)	Pore Volume (cm^3/g)
As-cast	600	0.42
DMF-Conditioned	650	0.42
Methanol-Conditioned	730	0.48

When comparing the DMF-conditioned and methanol-conditioned films, there are noticeable differences in the N_2 uptake throughout the range of relative pressures measured. The shape of the isotherm remains the same, but the uptake at every pressure is much higher for the methanol-conditioned film. This increased uptake is reflected in both higher BET surface areas and pore volumes. The methanol-conditioned films are within the surface

area range reported for PIM-1.[15] The methanol-conditioned films in this experiment were previously conditioned via exposure to liquid DMF. This past processing history does not have any apparent effect on the surface area or pore volume of the PIM-1 films, indicating that methanol treatments reverse the effects of conditioning. Although DMF swells PIM-1 more than methanol,[12] it does not impart additional free volume to the microstructure once it has been evacuated. The pore volume can be roughly comparable to the free volume within the polymer when qualitatively comparing the different conditioned PIM-1 samples. However, there exists free volume elements smaller than N_2 molecules that are not captured in the pore volume measurements.[16]

Three different PIM-1 films were analyzed with TGA in Figure 6.4 to determine the amount of residual solvent trapped in the films. An as-cast film sample was analyzed and showed almost no mass loss during the 100°C, in-situ drying step, indicating that the film was completely dry and did not retain any THF many days after film casting. The DMF-conditioned sample was soaked in DMF for 24 hours, removed from the liquid, and wiped dry. The sample was left at ambient conditions for several hours before analysis in the TGA. The seemingly dry sample retained a substantial amount of nonsolvent in the micropores, as seen in Figure 6.4, which was completely removed during the in-situ drying step. Lastly, the methanol-conditioned sample was soaked in DMF for 24 hours, rinsed with methanol, soaked in methanol for 24 hours, and then wiped dry. The sample was left at ambient conditions for several hours before TGA analysis just like the DMF-conditioned sample. The methanol-conditioned and as-cast samples are nearly identical, indicating that the methanol treatment effectively removed any DMF that would normally be trapped in the micropores and that the methanol completely evacuates the sample after several hours

under ambient conditions. Even relatively mild drying steps prior to analysis—in this case, 100°C under flowing dry nitrogen—are satisfactory in completely removing residual solvents in the films. Membranes are usually dried under much more aggressive conditions (high temperature and vacuum) to completely remove residual solvents. Based on this analysis, the in-situ, pre-analysis drying steps in the vapor sorption apparatus and the nitrogen physisorption apparatus should completely dry the samples. As a result, the effects of nonsolvent conditioning are most likely changes to the underlying polymer microstructure rather than effects due to residual nonsolvents occupying space in the pores.

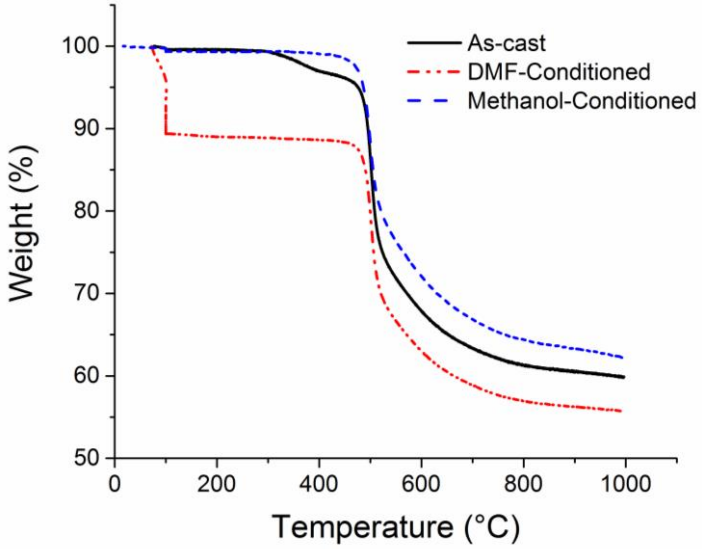

Figure 6.4 Thermogravimetric analysis curves of as-cast, DMF-conditioned, and methanol-conditioned PIM-1 films. The temperature profile consist of a 10°C/min ramp to 100°C, a one hour hold at 100°C, and a second 10°C/min ramp to 1000°C under a nitrogen atmosphere.

Both the DMF-conditioned and the methanol-conditioned films exhibit the same shape and mass loss at approximately 500°C compared to the as-cast film. The methanol-conditioned film is nearly identical to the as-cast film except for the small mass loss beginning at approximately 300°C for the as-cast film. That small loss corresponds to the

low molecular weight fractions of polymer remaining in the sample after purification (this initial loss has been misinterpreted as the decomposition temperature of PIM-1). These fractions are soluble in DMF and removed during the DMF conditioning step, as evidenced by the DMF solution turning fluorescent yellow and the presence of low molecular weight fractions in the GPC analysis. The high molecular weight fractions remain insoluble in DMF and as a result, these small mass losses do not appear in either the DMF-conditioned or methanol-conditioned films.

6.3.3 Alternative Nonsolvent Treatments

Taking into consideration all of the desirable qualities of an effective nonsolvent treatment for adding free volume, several alternatives to methanol were investigated. Based on the set of experiments in this study, ideal nonsolvents for increasing pore volume and surface area exhibit the following characteristics:

i. Induce appreciable swelling in the polymer at unit activity to impart as much free volume as possible
ii. have a high vapor pressure, and therefore a strong driving force for evaporation to leave the polymer
iii. have weak polymer-penetrant interactions to minimize plasticization effects.

Acetone was chosen as a potential nonsolvent because it swells PIM-1 to the same degree as methanol but has almost double the vapor pressure. Based on swelling and vapor pressure alone, acetone-conditioned PIM-1 would be expected to have a higher surface area and pore volume. However, the acetone-conditioned porosities are lower than those of the methanol-conditioned samples as determined by the nitrogen isotherms in Figure 6.5

and Table 6.3. Again, PIM-1 powders were used instead of films to lower the mass transfer resistance seen in the nitrogen physisorption experiments. This further emphasizes that specific polymer-penetrant interactions are also important in understanding and choosing nonsolvent treatments. Since the acetone-conditioned sample has a lower surface area and pore volume compared to the methanol-conditioned sample, acetone most likely plasticizes PIM-1 to some degree that ultimately reduces the free volume for the reasons noted earlier. Detailed experimental analysis is required to confirm the extent of acetone-induced plasticization of PIM-1, but it is reasonable to expect that acetone—a polar aprotic nonsolvent with a carbonyl group like DMF—will plasticize PIM-1.

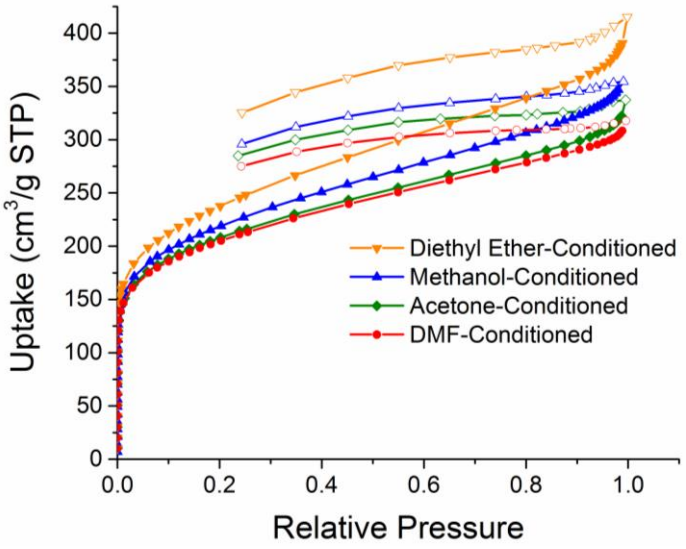

Figure 6.5 Nitrogen physisorption at 77 K in diethyl ether-conditioned, methanol-conditioned, acetone-conditioned, and DMF-conditioned PIM-1 powders.

Table 6.3 BET surface areas and pore volumes for different nonsolvent-conditioned PIM-1 powders determined from nitrogen physisorption at 77 K.

Sample	BET Surface Area (m^2/g)	Pore Volume (cm^3/g)	Reference
Diethyl ether-conditioned	830	0.64[a]	12
Methanol-conditioned	770	0.55[a]	12
Acetone-conditioned	730	0.52[a]	12
DMF-conditioned	730	0.49[a]	12
PIM-1	860	0.68[b]	5
PIM-1	768	0.70[a]	17
PIM-1	771	0.57[c]	18

[a]Pore volume determined at $p/p^0 = 0.99$.
[b]Pore volume determined at $p/p^0 = 0.98$.
[c] p/p^0 not reported.

Diethyl ether was chosen as a nonsolvent to further illustrate the effect of nonsolvent physical characteristics on the conditioning of PIM-1 since diethyl ether has a vapor pressure more than four times greater than methanol and swells PIM-1 to approximately the same degree.[12] Moreover, a non-halogenated, nonpolar nonsolvent will likely not significantly plasticize PIM-1, thus fulfilling the three criteria outlined for increasing free volume. Physisorption results in Table 6.3 indicate that diethyl ether produces PIM-1 powders with the highest surface area and pore volume of the nonsolvents studied to date. As diethyl ether likely does not drastically plasticize PIM-1 and quickly evacuates the polymer due to its very high vapor pressure, there is neither sufficient relaxation time nor segmental mobility to relax out the additional free volume imparted by the diethyl ether sorption.

Similarly, conditioning guidelines for reducing the fractional free volume and essentially artificially aging the polymer can be expressed. Nonsolvents that have low

vapor pressures, strong affinity for the polymer, and induce plasticization are desirable. The extent of swelling is not an important factor for reducing free volume and it is unlikely that a nonsolvent has the abovementioned criteria without inducing some degree of swelling.

6.3.4 Defect Treatment in PIM-1 Hollow Fiber Membranes

The susceptibility of PIM-1 to conditioning and microstructural changes due to exposure to nonsolvents can be exploited to remove small defects present in the membrane. During the hollow fiber spinning process, minor fluctuations in the parameters (flow rates, temperatures, etc.) can result in membranes with a small population of Knudsen defects in the selective layer. Glassy polymers like polyimides can be thermally annealed near their T_g to impart a small amount of polymer chain mobility and remove these types of defects or can simply be post treated with additional polymers (such as PDMS) to cover the defects. However, these additional coatings confound subsequent pyrolysis steps and are not solvent-resistant. PIM-1's lack of glass transition temperature before decomposition prevents sub-T_g annealing methods from being applied. Instead, various nonsolvents can be used to impart chain mobility to the system and effectively heal small defects. By treating partially defective, pre-fabricated hollow fiber membranes, defect-free fibers can be reliably produced.

As discussed earlier, DMF has been shown to condition and accelerate the aging of PIM-1 membranes through a combination of plasticization and low volatility that decreases the fractional free volume of the system.[12] Conditioning of PIM-1 hollow fibers with pure DMF was applied as shown in Figure 6.6.[13] The previously asymmetric fiber becomes

completely dense, increasing the skin layer from a few micrometers to several hundred micrometers. The DMF conditioning cannot be isolated to the skin layer alone due to the strong sorption in the polymer. The entire fiber plasticizes and the kinetically trapped porous substructure relaxes towards its dense equilibrium packing. This morphological observation supports previous analysis that indicates that PIM-1 completely plasticizes at DMF relative saturation in excess of 0.55.[12]

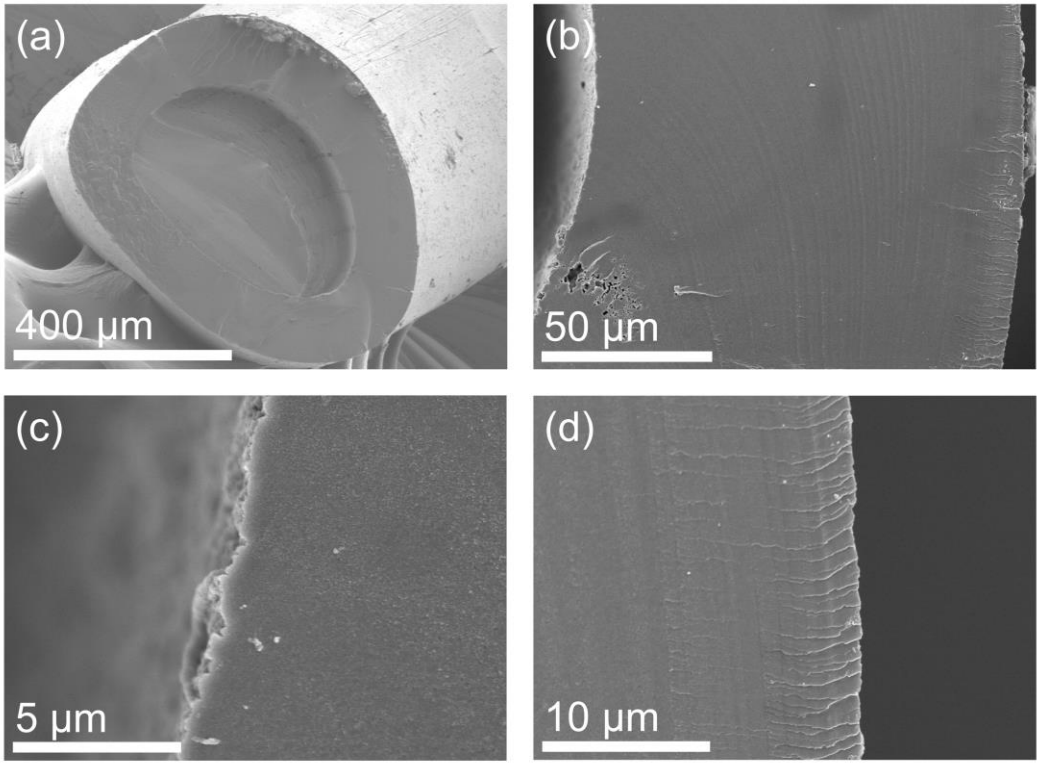

Figure 6.6 SEM images of a DMF-conditioned PIM-1 fiber (a) cross section, (b) wall cross section, (c) internal surface layer, and (d) external skin layer.

To moderate the extent and effectiveness of the DMF conditioning, the concentration of DMF in solution was controlled by mixing with water. Water acts as a very strong and minimally interacting nonsolvent for many hydrophobic polymers. It does not swell or plasticize the polymer and can effectively be used as an "inert" to control the

relative activity of the DMF in the liquid phase.[19] PIM-1 fibers were conditioned with various aqueous DMF solutions. The nonsolvent-induced swelling and subsequent shrinkage after drying is shown in Figure 6.7. Only after exposures greater than 40 wt% DMF do the fibers experience irreversible changes to the micro- and macrostructure of the fiber.

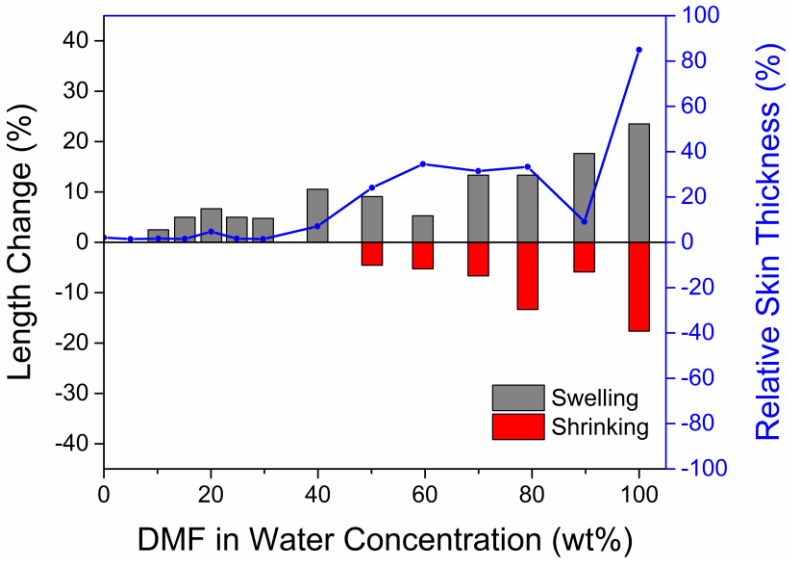

Figure 6.7 Nonsolvent-induced swelling and subsequent shrinkage after drying for PIM-1 hollow fiber membranes. Fibers were measured dry, soaked in various aqueous DMF solutions for 24 hours, dried under vacuum at 80°C, and then remeasured. The relative skin thickness is a measure of the thickness occupied by the skin layer relative to the entire fiber wall.

The extent and type of structural change is better visualized by examining the fibers after nonsolvent treatment. As the DMF concentration in solution increases, the skin layer densifies and becomes significantly thicker. Figure 6.8 shows the cross section of post-treated fibers exposed to different concentrations of DMF. The 0 wt% and 25 wt% fibers (Figure 6.8a and b) are nearly identical and maintain the same asymmetric structure as

formed during the fiber spinning process. The skin layer in these fibers is very small, at most a few micrometers thick. As the DMF concentration increases (Figure 6.8c and d), the skin layer increases significantly due to significant plasticization from the DMF followed by capillary collapse during drying.[19] When the DMF concentration becomes very high, the skin layer densification becomes less radially symmetric. The dense region in Figure 6.8d appears as striations through the fiber cross section. This is likely due to local variations in the fiber microstructure that allow for certain parts of the fiber to densify preferentially.

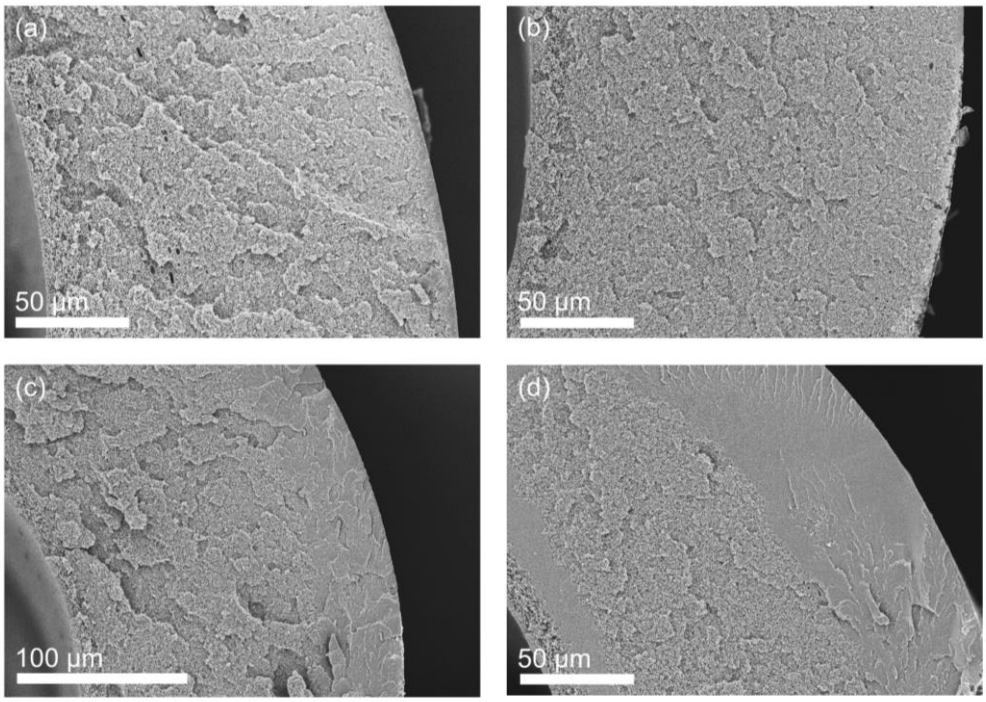

Figure 6.8 (a) PIM-1 fiber treated with a 0 wt% DMF aqueous solution. (b) PIM-1 fiber treated with a 25 wt% DMF aqueous solution. (c) PIM-1 fiber treated with a 50 wt% DMF aqueous solution. (d) PIM-1 fiber treated with an 80 wt% DMF aqueous solution.

Due to the radially asymmetric morphology of the hollow fiber, densification begins at the skin layer where the membrane is most dense. To confirm this hypothesis,

DMF conditioning was applied to a completely porous PIM-1 film without a skin layer. Figure 6.9 shows a porous PIM-1 film before and after DMF conditioning with a 50 wt% DMF aqueous solution. Without the nano- to mesoscopic porosity present near the membrane's skin layer to help initiate structural collapse, densification and substructure collapse are not seen under these conditions. However, local changes to the microstructure do occur as a result of nonsolvent conditioning. The very rough edges of the pores (Figure 6.9c) become more rounded and smooth after conditioning (Figure 6.9d), further supporting that DMF conditioning only effects change on the sub-micrometer level.

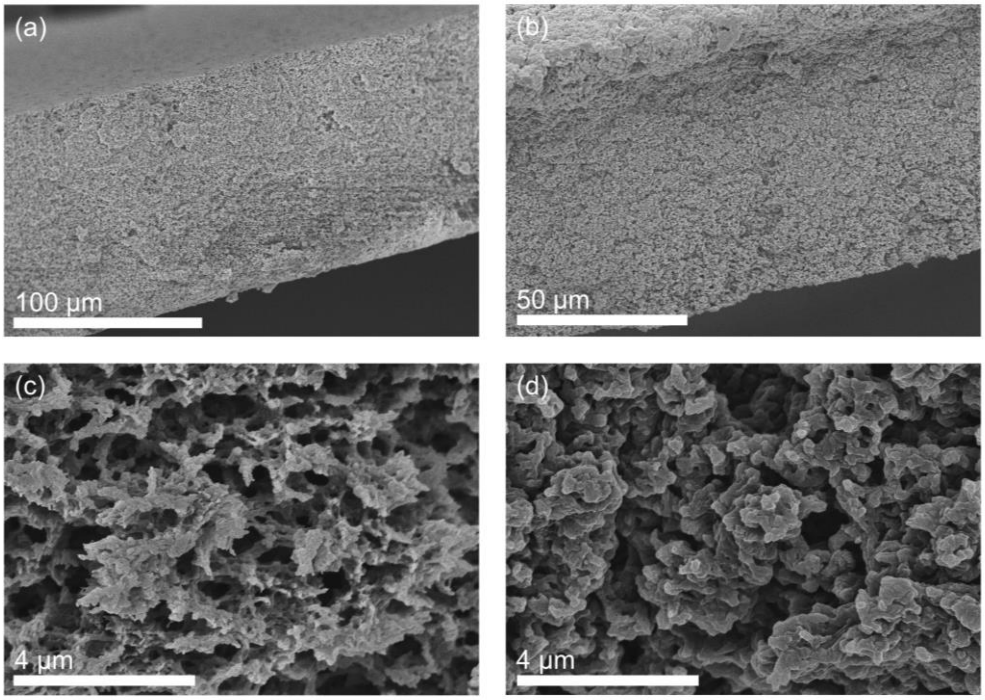

Figure 6.9 (a) and (c) Porous PIM-1 film without any conditioning. (b) and (d) Porous PIM-1 film after conditioning with a 50 wt% DMF aqueous solution.

Besides visual changes to the microstructure, gas permeation was used to quantify changes in performance due to DMF conditioning. Figure 6.10 shows an array of CO_2/CH_4

pure component permeation data for PIM-1 hollow fiber membranes treated under different conditions. Fibers soaked for the longest amount of time (24 hours, red squares) had the lowest performance overall, likely due to the highest degree of structural changes from prolonged exposure to plasticizing environments. Fibers with a longer drying time (overnight, blue triangles) had superior performance compared to fibers dried for only an hour (green diamonds). It is likely that extended drying of the sample allows for the plasticized polymer chains to fully reorient themselves and heal the small defects. As seen in Figure 6.8, fibers soaked in higher concentrations of DMF experience significant skin layer thickening and substructure densification. There is a tradeoff between removing the defects and unnecessarily densifying the skin layer, which adds additional mass transfer resistance. Regardless of the exact conditions used, using a DMF/water mixture to condition the membranes can remove small defects and improve the separation performance to those that exceed previously reported values.[13] Similar attempts to remove defects utilizing nonsolvent vapors proved less effective than in the liquid systems.[19]

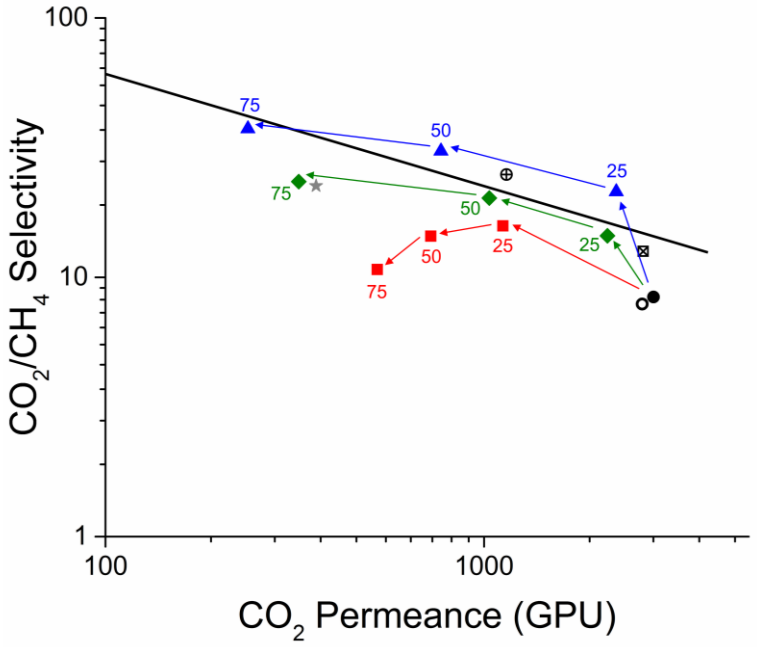

Figure 6.10 PIM-1 hollow fiber membrane performance after various nonsolvent treatments. Carbon dioxide and methane permeation were measured at 35°C and 100 psig. The black circle represents the unmodified, slightly defective control fiber and the grey star a defect-free, aged fiber. The red squares represent fibers soaked for 24 hours and dried overnight, the green diamonds fibers soaked for 1 hour and dried for 1 hour, and the blue triangles fibers soaked for 1 hour and dried overnight with the DMF wt% in the aqueous solution given above the symbol. Arrows are drawn to guide the eye. The open circle represents fibers soaked in a 0 wt% DMF solution, crossed circle methanol exchanged fibers, and crossed square ambient dried fibers. The 2008 upper bound for a 1 µm thick membrane is drawn for comparison.

Several control experiments were performed to confirm that the combination of plasticization and surface tension driven cohesive forces are indeed critical factors to the effectiveness of the DMF conditioning.[19] Fibers conditioned with pure water (open circle, Figure 6.10) exhibited essentially no change in the separation performance, indicating that plasticization of the polymer is required to alter the microstructure. Just as with the nonsolvents discussed previously (e.g., DMF, methanol), the rate of nonsolvent removal is key. Nonsolvent removal via solvent exchange (crossed circle, Figure 6.10) is slower than by vaporization, but still sufficiently rapid to cause some surface tension effects and heal

defects. Very slow nonsolvent removal at ambient conditions for several days (crossed square, Figure 6.10) slightly improved the membrane's performance, although that could mainly be due to plasticization effects during soaking. More detailed analysis of the PIM-1/nonsolvent interactions is somewhat difficult without further rheological and fundamental polymer solution measurements. However, from these gas permeation results, it is clear that the combination of both plasticization and high rate of nonsolvent removal are important factors in successful defect treatment.

6.3.5 Aging

The experiments discussed here did not investigate the aging of PIM-1 after membrane formation or after the various nonsolvent treatments. While exposure to high vapor pressure nonsolvents such as methanol and diethyl ether increases the free volume, it is uncertain how long the additional free volume remains in the polymer. Studies of freshly synthesized and year old PIM-1 stored at ambient conditions show that the surface area remains approximately the same but the gas permeability drops with age.[4,6] It is uncertain whether or not diethyl ether-conditioned PIM-1 will age faster than methanol-conditioned PIM-1, although it is likely. There is growing research interest to stabilize the aging effects of highly porous polymers and polymer derivatives, and these could be reasonably applied to PIM hollow fiber membranes.[20,21] It is worth noting that Pinnau et al. and Koros et al. have shown that physical aging in microporous materials such as poly(1-trimethylsilyl-1-propyne) (PTMSP) and carbon molecular sieve (CMS) membranes can largely be mitigated by keeping the membranes under active penetrant pressure (actively testing the membranes for extended periods of time rather than periodic testing

with long-term storage at ambient conditions).[21,22] The penetrant molecules likely act as "proppants" and physically hinder compaction or aging of the structure.[21,22]

6.4 Conclusions

The apparent microstructure of high free volume polymers such as PIM-1 are strongly dependent on the past processing history of the material. Organic nonsolvents such as DMF can condition, swell, and plasticize PIM-1. The combination of methanol's high vapor pressure, appreciable swelling and dilation of PIM-1, and weak polymer-penetrant interactions allows it to reverse the effects of conditioning—processing history and aging—on PIM-1 and restore lost free volume. These design principles can be applied to manipulate the microstructure of PIM-1 for a number of applications. The use of plasticizing nonsolvents with low vapor pressure such as DMF can be used to heal defects in the membrane. Nonsolvent mixtures can also be utilized to moderate the plasticization of the system. The combination of plasticization and removal rate contribute significantly to the effectiveness of the defect treatment and nonsolvent conditioning overall. Defect-treated PIM-1 hollow fibers exhibit good gas separation performance and greatly improve the reproducibility of defect-free PIM-1 fibers.

6.5 References

(1) Park, J. Y.; Paul, D. R. Correlation and prediction of gas permeability in glassy polymer membrane materials via a modified free volume based group contribution method. *J. Membrane Sci*. **1997**, *125*, 23-39.

(2) Freeman, B. D. Basis of Permeability/Selectivity Tradeoff Relations in Polymeric Gas Separation Membranes. *Macromolecules* **1999**, *32*, 375-380.

(3) Galizia, M.; De Angelis, M. G.; Sarti, G. C. Sorption of hydrocarbons and alcohols in addition-type poly(trimethyl silyl norbornene) and other high free volume glassy polymers, II: NELF model predictions. *J. Membrane Sci*. **2012**, *405-406*, 201-211.

(4) Lau, C. H.; Nguyen, P. T.; Hill, M. R.; Thornton, A. W.; Konstas, K.; Doherty, C. M.; Mulder, R. J.; Bourgeois, L.; Liu, A. C. Y.; Sprouster, D. J.; Sullivan, J. P.; Bastow, T. J.; Hill, A. J.; Gin, D. L.; Noble, R. D. Ending Aging in Super Glassy Polymer Membranes. *Angew. Chem. Int. Edit.* **2014**, *53*, 5322-5326.

(5) Budd, P. M.; Elabas, E. S.; Ghanem, B. S.; Makhseed, S.; McKeown, N. B.; Msayib, K. J.; Tattershall, C. E.; Wang, D. Solution-Processed, Organophilic Membrane Derived from a Polymer of Intrinsic Microporosity. *Adv. Mater*. **2004**, *16*, 456-459.

(6) Budd, P. M.; Ghanem, B. S.; Makhseed, S.; McKeown, N. B.; Msayib, K. J.; Tattershall, C. E. Polymers of intrinsic microporosity (PIMs): robust, solution-processable, organic nanoporous materials. *Chem. Commun*. **2004**, 230-231.

(7) Berens, A. R.; Hodge, I. M. Effects of annealing and prior history on enthalpy relaxation in glassy polymers. 1. Experimental study on poly(vinyl chloride). *Macromolecules* **1982**, *15*, 756-761.

(8) Chan, A. H.; Paul, D. R. Influence of history on the gas sorption, thermal, and mechanical properties of glassy polycarbonate. *J. Appl. Polym. Sci*. **1979**, *24*, 1539-1550.

(9) Budd, P. M.; McKeown, N. B.; Ghanem, B. S.; Msayib, K. J.; Fritsch, D.; Starannikova, L.; Belov, N.; Sanfirova, O.; Yampolskii, Y.; Shantarovich, V. Gas permeation parameters and other physicochemical properties of a polymer of intrinsic microporosity: Polybenzodioxane PIM-1. *J. Membrane Sci*. **2008**, *325*, 851-860.

(10) Hill, A. J.; Pas, S. J.; Bastow, T. J.; Burgar, M. I.; Nagai, K.; Toy, L. G.; Freeman, B. D. Influence of methanol conditioning and physical aging on carbon spin-lattice relaxation times of poly(1-trimethylsilyl-1-propyne). *J. Membrane Sci*. **2004**, *243*, 37-44.

(11) Seong, J. G.; Zhuang, Y.; Kim, S.; Do, Y. S.; Lee, W. H.; Guiver, M. D.; Lee, Y. M. Effect of methanol treatment on gas sorption and transport behavior of intrinsically microporous polyimide membranes incorporating Troger's base. *J. Membrane Sci*. **2015**, *480*, 104-114.

(12) Jue, M. L.; McKay, C. S.; McCool, B. A.; Finn, M. G.; Lively, R. P. Effect of Nonsolvent Treatments on the Microstructure of PIM-1. *Macromolecules* **2015**, *48*, 5780-5790.

(13) Jue, M. L.; Breedveld, V.; Lively, R. P. Defect-free PIM-1 hollow fiber membranes. *J. Membrane Sci*. **2017**, *530*, 33-41.

(14) Struik, L. *Physical Aging in Amorphous Polymers and Other Materials*, Elsevier: Amsterdam, 1978.

(15) Budd, P. M.; Msayib, K. J.; Tattershall, C. E.; Ghanem, B. S.; Reynolds, K. J.; McKeown, N. B.; Fritsch, D. Gas separation membranes from polymers of intrinsic microporosity. *J. Membrane. Sci*. **2005**, *251*, 263-269.

(16) Heuchel, M.; Fritsch, D.; Budd, P. M.; McKeown, N. B.; Hofmann, D. Atomistic packing model and free volume distribution of a polymer with intrinsic microporosity (PIM-1) *J. Membrane. Sci*. **2008**, *318*, 84-99.

(17) Swaidan, R.; Ghanem, B. S.; Litwiller, E.; Pinnau, I. Pure- and mixed-gas CO_2/CH_4 separation properties of PIM-1 and an amidoxime-functionalized PIM-1. *J. Membrane. Sci.* **2014,** *457*, 95-102.

(18) Patel, H. A.; Yavuz, C. T. Noninvasive functionalization of polymers of intrinsic microporosity for enhanced CO_2 capture. *Chem. Commun.* **2012,** *48*, 9989-9991.

(19) Rezac, M. E.; Le Roux, J. D.; Chen, H.; Paul, D. R.; Koros, W. J. Effect of mild solvent post-treatments on the gas transport properties of glassy polymer membranes. *J. Membrane Sci*. **1994**, *90*, 213-229.

(20) Lau, C. H.; Konstas, K.; Thornton, A. W.; Liu, A. C. Y.; Mudie, S.; Kennedy, D. F.; Howard, S. C.; Hill, A. J.; Hill, M. R. Gas-Separation Membranes Loaded with Porous Aromatic Frameworks that Improve with Age. *Angew. Chem. Int. Ed.* **2015**, *54*, 2669-2673.

(21) Xu, L.; Rungta, M.; Hessler, J.; Qiu, W.; Brayden, M.; Martinez, M.; Barbay, G.; Koros, W. J. Physical aging in carbon molecular sieve membranes. *Carbon* **2014**, *80*, 155-166.

(22) Pinnau, I.; Casillas, C. G.; Morisato, A.; Freeman, B. D. Long-Term Permeation Properties of Poly(1-trimethylsilyl-1-propyne) Membranes in Hydrocarbon-Vapor Environment. *J. Polym. Sci. Part B: Polym. Phys.* **1997**, *35*, 1483-1490.

CHAPTER 7. FORMATION AND SEPARATION PERFORMANCE OF PIM-1-DERIVED CARBON MOLECULAR SIEVE HOLLOW FIBER MEMBRANES FOR ORGANIC SOLVENT REVERSE OSMOSIS

The formation, characterization, and membrane separation performance of carbon molecular sieve membranes derived from PIM-1 are discussed. The separation of *p*-xylene and 1,3,5-triisopropylbenzene is used as a proof-of-concept demonstration of organic solvent reverse osmosis in this system.

7.1 Introduction

Carbon molecular sieves (CMS) are the primary product of the pyrolysis of an organic precursor in an inert atmosphere. Although the exact mechanism of decomposition is difficult to determine, polymer chain scission and rearrangement to form sp^2 hybridized sheets are generally believed to occur.[1-3] The resulting turbostractic carbon packs into an amorphous structure that has short range order and a distribution of pores.[4,5] These carbon sheets tend to result in a microstructure composed of ultramicropores—which lead to high diffusive selectivities—and micropores, which contribute to high sorption capacity. The ultramicropores in the material dominate the diffusive transport and allow CMS materials to act as molecular sieves. Generally the formation protocol is investigated to alter the diffusive selectivity of the CMS, as the sorption selectivity remains close to unity after the loss of most non-aromatic functional groups.[6] However, recent work has shown that the sorption capacity of the CMS materials can also be altered by changes in the pyrolysis

conditions.[7] Being able to tune both the sorption and diffusion selectivity of the CMS allows for even greater control of the system for targeted separations.

The formation of CMS membranes is dependent on a number of parameters. The most prominent being the choice of precursor material, the pyrolysis temperature profile (emphasis on the final temperature), and the pyrolysis environment.[3,8] Increasing the maximum pyrolysis temperature tightens the CMS structure, generally leading to more selective, but less permeable membranes.[4,9] An illustrative diagram of the pore size distribution shown in Figure 7.1, where the average pore size decreases and the pore size distribution narrows with increasing pyrolysis temperature.[4] Other specifics of the pyrolysis temperature profile, such as the amount of time at the final temperature, can also influence the resulting separation performance.[4]

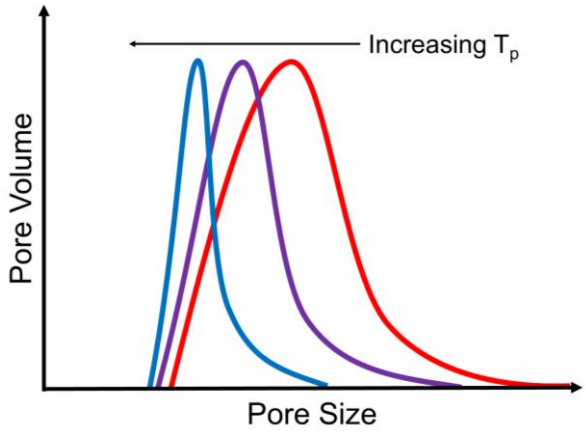

Figure 7.1 Hypothetical change in CMS pore size distribution with increasing pyrolysis temperature.

Temperature protocol aside, the pyrolysis environment is also important. Either inert gases or vacuum are used to reduce the oxygen content around the CMS during pyrolysis to prevent rapid oxidation at high temperatures. Even parts per million levels of

oxygen have been shown to alter the CMS separation performance.[3,6,8] This controlled oxygen doping can be used to fine tune the pore size of the resulting CMS structure by introducing oxygen atoms to the ultramicropores.[6] However, introduction of high levels of oxygen can lead to incorporation throughout the CMS structure that begins to lower the permeability and selectivity.[6] Other molecules besides oxygen, have been introduced to the CMS structure to manipulate the resulting membrane performance.[10,11]

CMS membrane materials have primarily been studied for gas separation applications. The small, generally less than 6 Å pores, created during the pyrolysis process lend themselves favorably to the separation of similarly-sized small molecules. CMS membranes have demonstrated extremely high selectivity for many gas pairs such as C_3H_6/C_3H_8,[12] C_2H_4/C_2H_6,[13] N_2/CH_4,[14] O_2/N_2,[4] and CO_2/CH_4.[4] Plasticization and swelling due to hydrocarbon vapors is significantly less pronounced in CMS membranes than their polymeric precursors. That resistance combined with their good separation performance position CMS as a promising membrane material.

Recently, CMS membranes have been applied to organic liquid separations. The first demonstration of OSRO of xylene isomers utilized polyvinylidene fluoride-based (PVDF) membranes.[15] First the PVDF was spun into defect-free, asymmetric hollow fiber membranes and then crosslinked with *p*-xylylenediamine.[15] Crosslinking with a rigid crosslinker is crucial to prevent substructure collapse of the rubbery polymer during pyrolysis.[15] Substructure collapse and densification of the support layer is particularly detrimental to the performance of OSRO membranes that operate with very low driving forces. Next, the crosslinked PVDF was pyrolyzed and assembled into a solvent-resistant membrane module for OSRO testing. These CMS membranes have diffusive selectivities

near 30 for *p*-xylene over *o*-xylene, which leads to an 81 mol% *p*-xylene enriched permeate starting from an equimolar feed.[15] While these separations were performed at room temperature, extremely high pressures (over 100 bar) were required—further emphasizing the need for the highly pressure-resistant hollow fiber form factor.[15]

Building upon this initial success, the work described here focuses on developing new CMS materials for OSRO based on the microporous polymer PIM-1. The formation, characterization, and gas and liquid separation performance of PIM-1-derived CMS hollow fiber membranes is used as another proof-of-concept study for the emerging area of OSRO separations.

7.2 Experimental

7.2.1 Materials

ACS grade *p*-xylene, *o*-xylene, 1,3,5-triisopropylbenzene, and tetrahydrofuran (THF) were purchased from either VWR or Alfa Aesar and used as received without purification. Rose bengal for OSN experiments was purchased from Alfa Aesar. Ultra high purity (UHP) grade gases used for pyrolysis and permeation were supplied by Airgas.

7.2.2 CMS Formation

The CMS materials used for sorption and permeation analysis were pyrolyzed from dried PIM-1 powders and fibers. Powders were placed in a ceramic holder supported on a 316 stainless steel mesh. Fibers were directly fixed to the mesh. The PIM-1 was pyrolyzed in a three zone tube furnace (MTI Corp.) under a 250 mL/min flowing argon atmosphere.[15] The polymer samples were purged for a minimum of six hours to ensure the oxygen content

was below 5 ppm before heating. An in-line oxygen sensor (Rapidox 1100Z, Cambridge Sensotec) at the outlet of the furnace was used to measure the oxygen content of the inert purge gas. CMS powders used for physisorption analysis followed the pyrolysis protocol as given in Table 7.1.[3]

Table 7.1 Temperature protocol for pyrolyzing PIM-1 powders.

Temperature Range (°C)	Ramp Rate (°C/min)
50 - 250	10
250 - (T_{max} – 15)	3
(T_{max} – 15) - T_{max}	0.25
T_{max}	Isothermal 2 hours
T_{max} - 25	Ambient

CMS hollow fiber membranes for OSRO followed various pyrolysis protocols as will be discussed in detail later. Untreated fibers were pyrolyzed according to the temperature profile given in Table 7.1. Defect-treated fibers were soaked in a 50 wt% DMF aqueous solution for one hour and dried overnight in an 80°C vacuum oven before pyrolysis.

7.2.3 Physisorption

Nitrogen physisorption at 77 K was attempted on CMS powders using an ASAP 2020 (Micromeritics). Due to the extremely slow kinetics of the sorption measurements, isotherms were not obtained even after multiple days. Instead, carbon dioxide physisorption at 195 K was performed on the CMS powders using the same instrument. A

dry ice and isopropyl alcohol bath was used to maintain the temperature. Samples were degassed at 115°C under vacuum for 12 hours before analysis.

7.2.4 Scanning Electron Microscopy

Fiber dimensions were measured using SEM images of CMS membranes with a Hitachi SU8230 FE-SEM with a cold field emission gun. A 5 kV accelerating voltage and 20 μA emission current were used to image samples. A Hummer 6 Gold/Palladium Sputterer was used to sputter coat the samples before imaging and analysis with ImageJ image processing software.

7.2.5 Organic Vapor Sorption Isotherms

Organic vapor sorption isotherms of CMS powders were conducted using the procedure described previously.[16]

7.2.6 Fiber Module Assembly

CMS fibers were assembled into single fiber membrane modules using ¼ inch Swagelok® tubing and fittings as shown in Figure 7.2. J-B Weld 8272 epoxy was used as the solvent-resistant epoxy to seal the fibers into the module. PTFE tape is placed in the tee to prevent the epoxy from leaking from the port adaptor into the module during curing.

Figure 7.2 CMS hollow fiber membrane module made from ¼ inch Swagelok® fittings.

7.2.7 Gas Permeation

Pure component gas permeation was conducted on the CMS fiber modules before liquid permeation to assess the quality of the membranes. Helium and nitrogen at 100 psig and 35°C were used in an isobaric permeation unit.[17] Modules were connected in parallel to the gas feed and slowly pressurized from the shell side of the module. The permeate flowrate from the bore side of the module was measured using a soap bubble flow meter. The membranes were allowed to permeate for a minimum of four hours before testing to ensure thermal equilibrium and steady state was reached. Steady state was assumed when there was no discernable change to the permeate flow rate over a period of two hours.

7.2.8 Organic Liquid Permeation

Dye solutions for OSN experiments were pressurized via syringe pump (Teledyne Isco). Rose bengal dissolved in THF (1 mg/L) was used as the feed solution. Modules were tested at 500 psig at ambient temperature in a dead end configuration. The pressure was increased slowly with a 1 psi/s ramp rate. The feed and permeate composition were analyzed using an UV-Vis spectrophotometer (Evolution 220, ThermoFisher Scientific) in the wavelength range from 200 to 750 nm, with a 1 nm resolution. The absorbance peak at 559 nm was used to determine the rose bengal concentration in solution.

Organic solvent mixtures for OSRO were tested in cross flow using a dual-pump continuous flow system shown schematically in Figure 7.3 (500D and 500E, Teledyne Isco).[15] Solutions of 95/5 mol% *p*-xylene/*o*-xylene and *p*-xylene/1,3,5-triisopropylbenzene were used as the feed mixtures. Modules were slowly pressurized from the shell side to the target pressure at 1 psi/s at ambient temperature. The membranes were allowed to permeate

for a minimum of 12 hours before testing. Steady state permeation was assumed after 10 times the downstream volume had permeated through the system. The stage cut was set to less than 1% using a needle valve connected to the retentate line to avoid concentration polarization. The permeate flow rate was determined by measuring the fluid level in a piece of calibrated 1/16 inch PTFE tubing. The permeate composition was analyzed via gas chromatography (7890 GC, Agilent) using a FID. The Wilson equation was used to estimate activity coefficients and calculate the intrinsic permeance of the system.

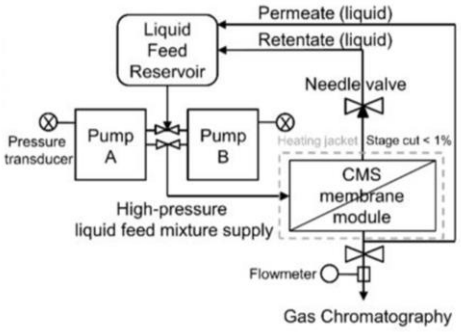

Figure 7.3 Schematic of dual-pump crossflow system for OSRO testing. Adapted with permission from ref 15. Copyright 2016 American Association for the Advancement of Science.

7.3 Results and Discussion

7.3.1 CMS Characterization

Glassy polymers such as polyimides are common precursor materials for CMS membranes. Especially for low driving force separations such as OSRO, asymmetric membranes with very thin separating layers are needed to maximize module productivity. If pyrolyzed directly—without any crosslinking or other pre-treatments—many of these materials will suffer some form of substructure collapse. Figure 7.4 shows an example of

substructure collapse in an asymmetric hollow fiber membrane. The very thin skin layer (less than 3 μm) increases to over 100 μm in thickness, thereby significantly increasing the transport resistance of the membrane. Substructure collapse during pyrolysis is attributed to a loss in storage modulus of the polymer as it passes through its glass transition temperature.[18] The rubbery polymer cannot maintain the kinetically trapped, asymmetric structure at elevated temperatures and collapses towards its denser, equilibrium packing.

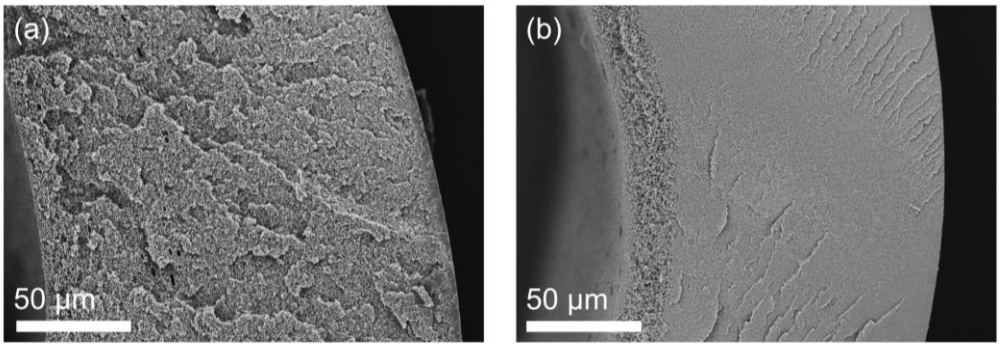

Figure 7.4 (a) Asymmetric hollow fiber membrane with a thin skin layer. (b) Asymmetric hollow fiber membrane after substructure collapse exhibiting a thick skin layer.

Crosslinking and other similar treatments have been shown to rigidify the polymer structure during pyrolysis and maintain the asymmetric structure.[15,18] While necessary, the crosslinking procedure adds a number of additional steps to the fabrication process and may also introduce defects into the selective layer. By utilizing polymeric precursor materials with no glass transition temperature, these crosslinking or pretreatment steps could be eliminated and therefore simplify the formation of asymmetric CMS membranes. Highly rigid polymers, like PIM-1, do not have an observable glass transition before the onset of decomposition and maintain their storage modulus even at very high temperatures.[19] Therefore, asymmetric PIM-1 membranes should be maintained during and

after pyrolysis without the need for crosslinking. SEM images of an asymmetric PIM-1 hollow fiber membrane before and after pyrolysis are shown in Figure 7.5. The retained asymmetric structure of the CMS fiber suggests that maintaining the storage modulus is indeed responsible for preserving the pre-fabricated structure.

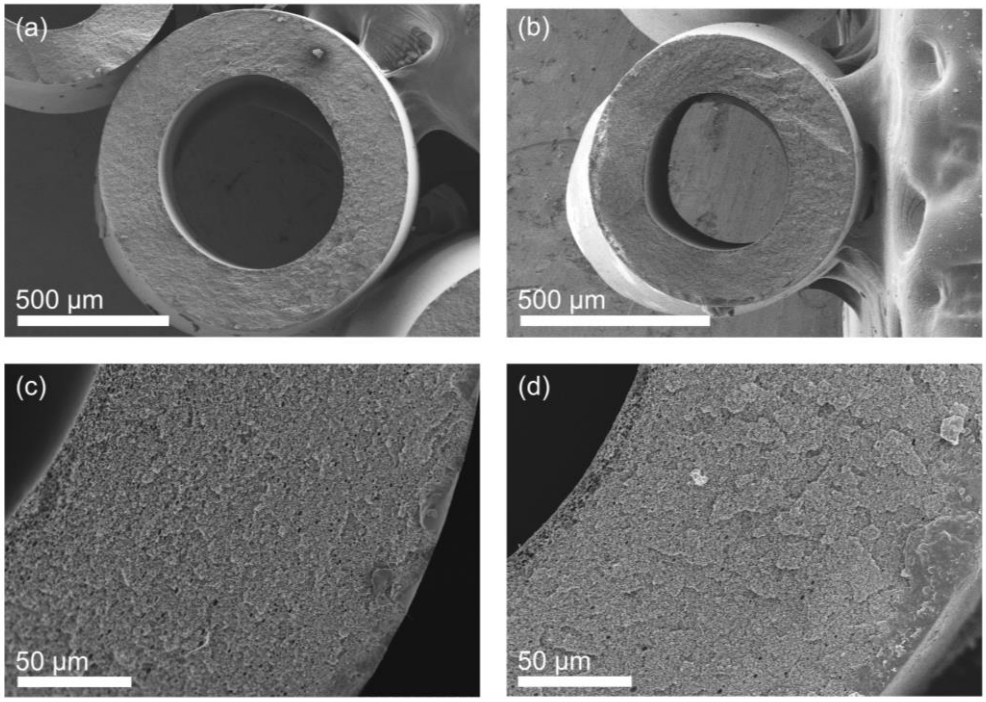

Figure 7.5 (a) and (c) PIM-1 hollow fiber membrane. (b) and (d) CMS hollow fiber membrane pyrolyzed from unmodified PIM-1.

Physisorption experiments were conducted to elucidate the structure and pore size information of PIM-1-derived CMS. Nitrogen physisorption at 77 K proved to be kinetically limited in both films (less than 10 µm) and powders. The nitrogen uptake is severely restricted and isotherm analysis is prohibitively slow. Instead, CO_2 physisorption at 195 K was used to characterize the CMS microstructure. The higher adsorption temperature allows measurement of CO_2 uptake and confidence that the equilibrium state is being measured. A select number of isotherms are shown in Figure 7.6. Pyrolysis at

500°C results in a CMS that still has significant polymer characteristics remaining, as seen by the dual mode shape of the isotherm. As the pyrolysis temperature increases to 750°C, the CMS becomes more carbon-like and exhibits a Langmuir isotherm. Finally at very high pyrolysis temperatures, the CMS structure packs very tightly, lowering the accessible volume. Attempts to determine the pore size distribution of the PIM-1 CMS using these isotherms led to physically unrealistic results, likely due to the strong quadrupole of CO_2 and its interactions with the carbon structure.

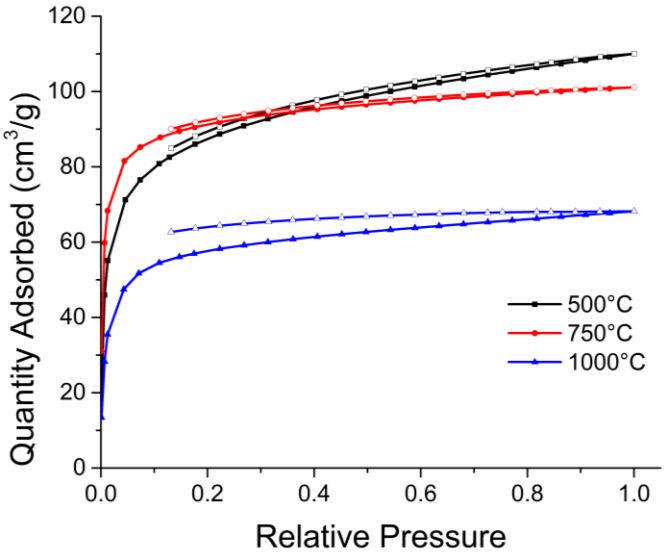

Figure 7.6 Carbon dioxide physisorption isotherms at 195 K for PIM-1 pyrolyzed at various temperatures.

The CO_2 isotherms can be further analyzed to determine the total pore volume for the system as shown in Figure 7.7. The PIM-1 CMS pore volume measured from CO_2 isotherms is compared to the crosslinked PVDF CMS pore volume as measured from N_2 isotherms at 77 K.[15] The PIM-1 CMS pore volume decreases with increasing pyrolysis temperature as expected of a tightening microstructure. The magnitude of the PIM-1 CMS pore volume is also significantly lower than both the neat PIM-1 (~0.5 cm_3/g) and

crosslinked PVDF CMS (~0.3 cm_3/g).[15,16] As PIM-1 is pyrolyzed, the high pore volume polymer begins to decompose and collapse into a denser carbon structure.[2] The opposite trend is true for PVDF-based CMS materials. Both the neat and crosslinked PVDF have negligible pore volume and only begin to become microporous during pyrolysis.[15] For the limited temperatures investigated, the crosslinked PVDF CMS gains pore volume with increasing temperature, which suggests that the creation of porosity in PVDF carbons at low pyrolysis temperatures follows a different mechanism than that observed in PIM-1.[15].

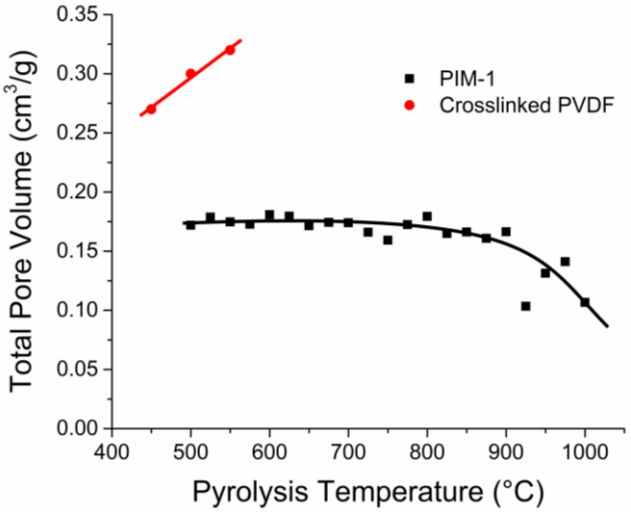

Figure 7.7 Total pore volume for PIM-1-derived CMS as determined from CO_2 physisorption at 195 K and reported crosslinked PVDF-derived CMS as determined from N_2 physisorption at 77 K. Lines are drawn to guide the eye.

Organic vapor sorption isotherms were measured on PIM-1 CMS powders. Figure 7.8 shows the adsorption of *p*-xylene in neat PIM-1, PIM-1-derived CMS pyrolyzed at 575°C, and crosslinked PVDF-derived CMS.[15] At low *p*-xylene activities, PIM-1 has substantial *p*-xylene sorption and a characteristic dual mode isotherm shape for sorption in a glassy polymer. After pyrolysis, the CMS loses much of that sorption capacity as evidenced by the order of magnitude decrease in mass uptake at 0.7 relative saturation.

Both CMS materials exhibit Langmuir isotherms and the *p*-xylene uptake for crosslinked PVDF CMS is nearly double that of the PIM-1 CMS, in agreement with the CO_2 physisorption results regarding the nature of PIM-1 CMS.[15]

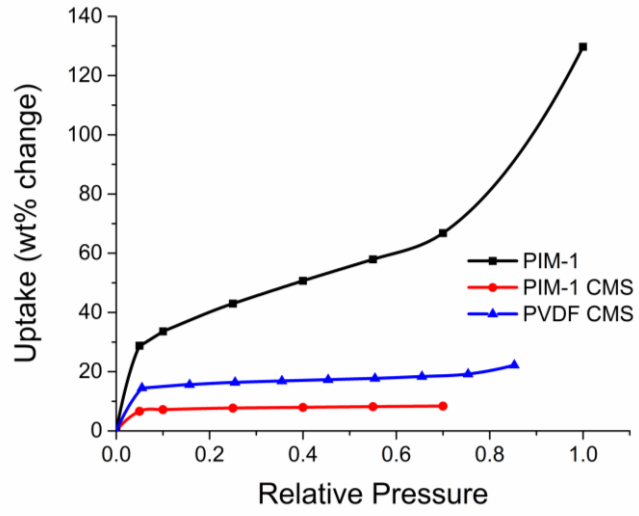

Figure 7.8 *p*-Xylene sorption isotherms at 35°C for PIM-1 and PIM-1-derived CMS pyrolyzed at 575°C, and at 25°C for crosslinked PVDF CMS.

7.3.2 Membrane Separations

Pure component gas separations were used to first assess the quality of the CMS membranes. Untreated PIM-1 fibers with known defects were pyrolyzed according to the pyrolysis protocol given in Table 7.1 to observe any changes to the fiber selectivity after pyrolysis. The population of existing defects remain in the final CMS after pyrolysis as given by a He/N_2 selectivity less than 2—lower than the Knudsen selectivity of 2.6 for the gas pair. Although not feasible for OSRO separations, these defective CMS membranes were tested for OSN applications. A rose bengal rejection study was conducted using THF as the solvent. The UV-Vis spectra for the separation is shown in Figure 7.9. The membrane exhibited a 97% rejection of rose bengal when operated in dead end filtration mode at

500 psig and ambient temperature. Based on estimates of the defect size from gas permeation experiments, nearly complete rejection of the rose bengal was expected. Although the solvent-resistant epoxy used to fabricate the membrane modules is resistant to many organic solvents, it is not highly resistant to oxygenated solvents such as THF. It is possible that poor interactions with the epoxy resulted in the lower than expected rose bengal rejection performance. Strong dye sorption and weakening of the epoxy were observed after testing with THF solutions. Regardless, this preliminary separation demonstrates the possibility of utilizing PIM-1-derived CMS with nanoscopic defects as highly solvent- and pressure-resistant OSN membranes.

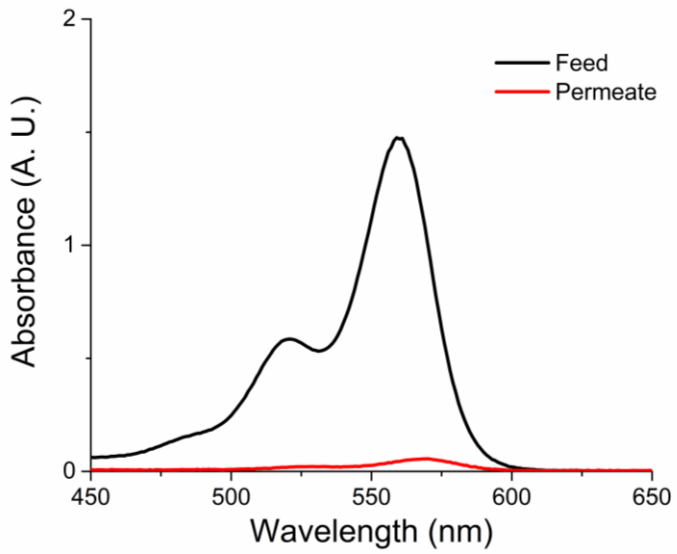

Figure 7.9 UV-Vis spectra of rose bengal in THF solutions for a PIM-1-derived CMS membrane pyrolyzed at 750°C. The membrane was run in dead end filtration mode with an applied pressure of 500 psig at room temperature.

The fiber pre-treatment and pyrolysis protocols were modified to help remove pre-existing defects in the PIM-1 fibers and improve the overall CMS membrane performance. Slightly defective PIM-1 fibers were treated with 50 wt% DMF aqueous solutions to

minimally densify the skin layer and ensure defect healing throughout the membrane. These defect-treated fibers were then pyrolyzed using a modified pyrolysis protocol given in Table 7.2. This new protocol includes an intermediate temperature hold before ramping to the final pyrolysis temperature. For polymers such as 6FDA/DETDA:DABA(3:2) with carboxylic acid functionality, the intermediate temperature hold allows for thermally induced crosslinking to occur before pyrolysis.[3] For PIM-1, a similar crosslinking-like step is included in the modified pyrolysis protocol.[2] In this system, thermo-oxidative crosslinking can occur at elevated temperatures with even parts per million levels of oxygen that leads to improved gas separation performance.[20]

Table 7.2 Modified pyrolysis protocol for CMS fibers.

Temperature Range (°C)	Ramp Rate (°C/min)
50 - 250	13.33
250 - 450	4
450	Isothermal for 1.5 hours
450 - (T_{max} – 15)	3.67
(T_{max} – 15) - T_{max}	0.25
T_{max}	Isothermal 2 hours
T_{max} - 25	Ambient

The gas separation performance of the defect-treated CMS fibers pyrolyzed at 575°C is shown in Figure 7.10. Even for these treated fibers, the separation performance varies significantly—indicating incomplete defect removal or unanticipated densification of the substructure. When compared to the crosslinked PVDF-derived CMS, the PIM-1 CMS generally has lower permeance but higher selectivity, although certain PIM-1 CMS

samples exceed the PVDF materials in both performance metrics.[15] After defect treatment and pyrolysis, the skin layer on the CMS fibers is several micrometers thick compared to the tens of nanometers thick skin on the crosslinked PVDF fibers.[15] Further optimization of the PIM-1 CMS membrane fabrication scheme should be employed to improve the defect treatment method, reduce the skin layer thickness, and boost the permeance.

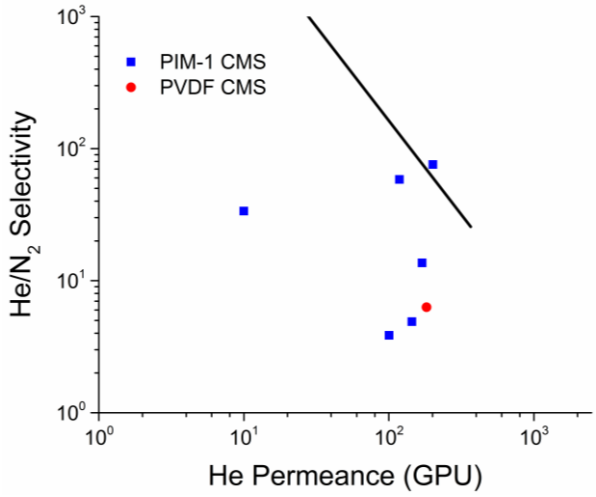

Figure 7.10 Gas separation performance of PIM-1-derived CMS pyrolyzed at 575°C and crosslinked PVDF-derived CMS. The 2008 Robeson polymer upper bound is given as a reference.

The gas tested fibers were then used for organic liquid separations. Due to the difficulties in determining the pore size of the CMS from physisorption analysis, a binary *p*-xylene/*o*-xylene mixture was chosen as a direct comparison to the previously reported PVDF-based membranes.[15] However, no separation selectivity was observed for this organic solvent pair. Consistent with the previous sorption isotherm analysis, it is possible that the CMS created during the pyrolysis of PIM-1 forms a very graphitic structure primarily composed of slit-like ultramicropores without many micropores for sorption. Indeed, XRD analysis of PIM-1 derived CMS indicates the formation of graphitic carbon

along with significant loss in porosity.[2] In such a system, planar xylene molecules can pass through the CMS with similar ease and no selectivity is expected. Both *p*-xylene and *o*-xylene molecules would permeate in the "flat" state and thus lose equal conformational states in the activated diffusion process.

Instead of the separation of two completely planar xylene isomers, a *p*-xylene/1,3,5-triisopropylbenzene mixture was chosen as the next mixture. Not only is there a large difference in the kinetic diameters of the two molecules (5.84 Å versus 8.5 Å), the bulky isopropyl groups are not in plane with the aromatic ring. The separation performance of the PIM-1-derived CMS membranes with this mixture is shown in Figure 7.11. The 95 mol% *p*-xylene mixture is enhanced up to 97 mol% in *p*-xylene (separation factor of 1.7) at 103 bar.

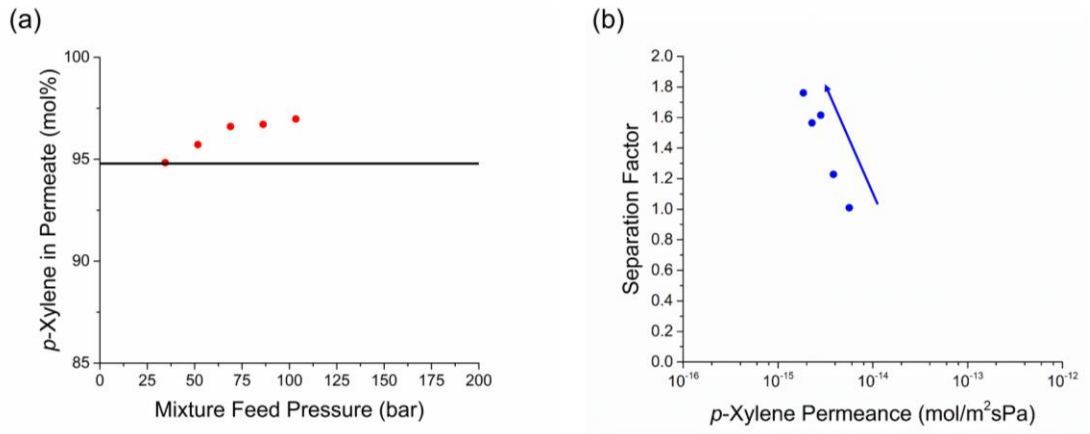

Figure 7.11 (a) Room temperature mixture permeation of *p*-xylene and 1,3,5-triisopropylbenzene. A 95 mol% *p*-xylene feed is enriched up to 97 mol% *p*-xylene in a single stage. (b) The corresponding separation factors for each composition. The arrow is in the direction of increasing hydraulic pressure.

Using the permeance flow rate and composition, the permselectivity can be calculated as shown in Figure 7.12.[15] Compared to previously reported CMS membranes

for OSRO, the permeate flux of these PIM-1-derived CMS membranes is about an order of magnitude lower due to the several orders of magnitude thicker skin layer.[15] The several orders of magnitude difference in intrinsic permeance further confirms the difference in the two membrane materials. Significantly decreasing the skin layer thickness should boost the permeance of the PIM-1 CMS membranes to similar levels as those exhibited by the crosslinked PVDF CMS membranes. The 575°C final pyrolysis temperature was chosen to ensure full carbonization of the polymer (as determined by the shape of the CO_2 sorption isotherm at 195 K) while maintaining as much pore volume as possible. Further improvements to the permselectivity can also be achieved by tuning the pyrolysis parameters for the desired separation. Nonetheless, the separation of *p*-xylene and 1,3,5-triisopropylbenzene remains a proof-of-concept demonstration of simplifying the fabrication route of asymmetric CMS membranes for OSRO by utilizing a rigid microporous polymeric precursor.

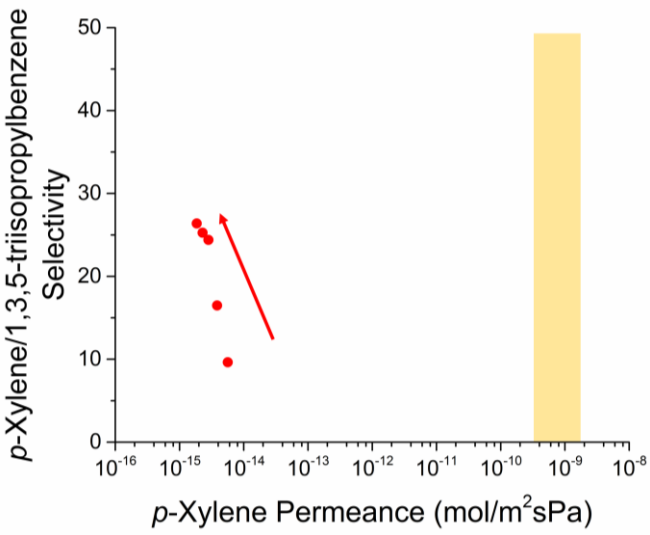

Figure 7.12 Mixture permselectivity of *p*-xylene/1,3,5-triisopropylbenzene at ambient temperature using PIM-1-derived CMS pyrolyzed at 575°C. The arrow is in the direction of increasing hydraulic pressure. The *p*-xylene permeances for the separation of *p*-xylene/*o*-xylene mixtures using crosslinked PVDF CMS is highlighted in gold.

7.4 Conclusions

PIM-1 hollow fiber membranes were directly pyrolyzed to form CMS hollow fiber membranes without the need for crosslinking or similar treatments. The asymmetric structure of the membranes remains intact during pyrolysis due to the lack of glass transition temperature of the highly rigid PIM-1 precursor. Removing the crosslinking step substantially reduces the fabrication complexity and enables a two-step method for creating asymmetric CMS hollow fiber membranes starting from a polymer powder.

Carbon dioxide physisorption and *p*-xylene sorption isotherms of PIM-1-derived CMS suggest that PIM-1 forms a much less porous and more restricted carbon structure than crosslinked PVDF CMS. Pure component gas separation experiments were performed to assess the membrane quality before organic liquid testing. Even after relatively aggressive

defect treatments, the membrane performance has quite a large spread in performance due to incomplete defect removal and unanticipated substructure densification. The proof-of-concept enrichment of a 95/5 mol% *p*-xylene/1,3,5-triisopropylbenzene mixture up to 97 mol% *p*-xylene was used to demonstrate the capability of PIM-1-derived CMS for challenging OSRO separations.

7.5 References

(1) Suda, H.; Haraya, K. Gas Permeation through Micropores of Carbon Molecular Sieve Membranes Derived from Kapton Polyimide. *J. Phys. Chem. B* **1997**, *101*, 3988-3994.

(2) Salinas, O.; Ma, X.; Litwiller, E.; Pinnau, I. Ethylene/ethane permeation, diffusion and gas sorption properties of carbon molecular sieve membranes derived from the prototype ladder polymer of intrinsic microporosity (PIM-1). *J. Membrane Sci*., **2016**, 504, 133-140.

(3) Fu, S.; Wenz, G. B.; Sanders, E. S.; Kulkarni, S. S.; Qiu, W.; Ma, C.; Koros, W. J. Effects of pyrolysis conditions on gas separation properties of 6FDA/DETDA:DABA(3:2) derived carbon molecular sieve membranes. *J. Membrane Sci*. **2016**, *520*, 699-711.

(4) Steel, K. M.; Koros, W. J. An investigation of the effects of pyrolysis parameters on gas separation properties of carbon materials. *Carbon* **2005**, *43*, 1843-1856.

(5) Steel, K. M.; Koros, W. J. Investigation of porosity of carbon materials and related effects on gas separation properties. *Carbon* **2003**, *41*, 253-266.

(6) Kiyono, M.; Williams, P. J.; Koros, W. J. Effect of pyrolysis atmosphere on separation performance of carbon molecular sieve membranes. *J. Membrane Sci.* **2010**, *359*, 2-10.

(7) Zhang, C.; Koros, W. J. Ultraselective Carbon Molecular Sieve Membranes with Tailored Synergistic Sorption Selective Properties. *Adv. Mater.* **2017**, 1701631.

(8) Geiszler, V. C.; Koros, W. J. Effects of Polyimide Pyrolysis Conditions on Carbon Molecular Sieve Membrane Properties. *Ind. Eng. Chem. Res.* **1996**, *35*, 2999-3003.

(9) Koros, W. J.; Zhang, C. Materials for next-generation molecularly selective synthetic membranes. *Nat. Mater*. **2017**, *16*, 289-297.

(10) Kim, H. J.; Kim, D. G.; Lee, K.; Baek, Y.; Yoo, Y.; Kim, Y. S.; Kim, B. G.; Lee, J. C. A Carbonaceous Membrane based on a Polymer of Intrinsic Microporosity (PIM-1) for Water Treatment. *Sci. Rep.* **2016**, *6*, 8.

(11) Wenz, G. B.; Koros, W. J. Tuning carbon molecular sieves for natural gas separations: A diamine molecular approach. *AIChE J.* **2017**, *63*, 751-760.

(12) Swaidan, R. J.; Ma, X.; Pinnau, I. Spirobisindane-based polyimide as efficient precursor of thermally-rearranged and carbon molecular sieve membranes for enhanced propylene/propane separation. *J. Membrane Sci.* **2016**, *520*, 983-989.

(13) Salinas, O.; Ma, X.; Wang, Y.; Han, Y.; Pinnau, I. Carbon molecular sieve membrane from a microporous spirobisindane-based polyimide precursor with enhanced ethylene/ethane mixed-gas selectivity. *RSC Adv.* **2017**, *7*, 3265-3272.

(14) Ning, X.; Koros, W. J. Carbon molecular sieve membranes derived from Matrimid® polyimide for nitrogen/methane separation. *Carbon* **2014**, *66*, 511-522.

(15) Koh, D.-Y.; McCool, B. A.; Deckman, H. W.; Lively, R. P. Reverse osmosis molecular differentiation of organic liquids using carbon molecular sieve membranes. *Science* **2016**, *353*, 804-807.

(16) Jue, M. L.; McKay, C. S.; McCool, B. A.; Finn, M. G.; Lively, R. P. Effect of Nonsolvent Treatments on the Microstructure of PIM-1. *Macromolecules* **2015**, *48*, 5780-5790.

(17) Jue, M. L.; Breedveld, V.; Lively, R. P. Defect-free PIM-1 hollow fiber membranes. *J. Membrane Sci.* **2017**, *530*, 33-41.

(18) Bhuwania, N.; Labreche, Y.; Achoundong, C. S. K.; Baltazar, J.; Burgess, S. K.; Karwa, S.; Xu, L.; Henderson, C. L.; Williams, P. J.; Koros, W. J. Engineering substructure morphology of asymmetric carbon molecular sieve hollow fiber membranes. *Carbon* **2014**, *76*, 417-434.

(19) Budd, P. M.; Elabas, E. S.; Ghanem, B. S.; Makhseed, S.; McKeown, N. B.; Msayib, K. J.; Tattershall, C. E.; Wang, D. Solution-Processed, Organophilic Membrane Derived from a Polymer of Intrinsic Microporosity. *Adv. Mater.* **2004**, *16*, 456-459.

(20) Song, Q.; Cao, S.; Pritchard, R. H.; Ghalei, B.; Al-Muhtaseb, S. A.; Terentjev, E. M.; Cheetham, A. K.; Sivaniah, E. Controlled thermal oxidative crosslinking of polymers of intrinsic microporosity towards tunable molecular sieve membranes. *Nat. Commun.* **2014**, *5*.

CHAPTER 8. CONCLUSIONS AND RECOMMENDATIONS

The major findings, conclusions, and recommendations for future work related to PIM-1-derived CMS membranes for furthering organic solvent reverse osmosis are discussed. Critical needs relating to the utilization of microporous materials for the separation of organic liquids are identified as well.

8.1 Summary

The work discussed here broadly encompasses many aspects of understanding and developing membrane-based separations at an academic level. First, starting with polymer synthesis, large quantities of the microporous polymer PIM-1 was produced with sufficient molecular weight for membrane formation. Dense PIM-1 membranes were fabricated and used to study the transport of organic molecules in microporous polymers. The inherent microporosity of the system does not significantly affect the transport mechanism and anomalous behavior—typical of organics in glassy polymers—was observed.[1] The relationship between solvent physical properties and the influence on PIM-1 were identified. In general, high boiling point solvents tend to plasticize and swell while low boiling point solvents tend to only swell PIM-1.[1] However, more detailed sorption and diffusion measurements are required to confirm any plasticization effects.

Next, PIM-1 was spun into defect-free hollow fiber membranes. Membrane solution processing techniques require the use of nonvolatile solvents such as NMP in combination with volatile solvents like THF; however, PIM-1 is not soluble in the typical nonvolatile solvents used for hollow fiber spinning. Utilizing a primarily volatile solvent

in the polymer solution introduces significant complications to the hollow fiber spinning process. To overcome these challenges, a simulated dual-bath spinning approach was taken. The primary quench medium, 1-butanol, was coextruded along with the polymer solution into a secondary water quench bath.[2] The 1-butanol layer acts as a protective sheath and prevents rapid THF evaporation from the polymer solution during spinning.[2] By carefully controlling the mass transfer rate during the fiber formation process, the first reported defect-free PIM-1 hollow fiber membranes were produced.[2] The gas separation performance of these membranes was in good agreement with reported work on analogous flat sheet PIM-1 membranes.

As thoroughly discussed in the literature, PIMs are highly susceptible to the effects of aging and conditioning—the change in material performance with time and processing history—due to the large excess free volume in the polymer. The specifics of this PIM-1 conditioning was studied and also exploited to develop a defect treatment method for pre-fabricated membranes. By utilizing nonsolvents with different affinities for PIM-1, DMF/water mixtures were used to existing heal defects in PIM-1 hollow fiber membranes.

Finally, a simplified fabrication scheme for creating asymmetric CMS hollow fiber membranes was developed utilizing PIM-1 as the precursor. Asymmetric PIM-1 hollow fiber membranes were directly pyrolyzed without the need for crosslinking or other pretreatments to produce asymmetric CMS membranes. Existing defects in the PIM-1 are maintained during pyrolysis and can compromise the separation performance. Although not feasible for OSRO, PIM-1-derived CMS membranes with small defects have potential as highly solvent-resistant OSN membranes. To address those defects, aggressively defect-treated PIM-1 membranes were pyrolyzed to form improved CMS hollow fiber

membranes. The separation of *p*-xylene and 1,3,5-triisopropylbenzene was used as a proof-of-concept demonstration of OSRO with these new membranes. Mixture selectivities as high as 26 were obtained for the separation of 95/5 mol% *p*-xylene/1,3,5-triisopropylbenzene at ambient temperatures. Taken together, this body of work probes many fundamental aspects of membrane science and engineering to further establish the emerging area of membrane-based organic solvent separations.

8.2 Future Work

Much of the work described here focused on developing the techniques to study fundamental material properties and fabricate practical membrane devices. Especially for the nonsolvent defect treatments, many of the findings are phenomenological in nature rather than based on physical properties of the system. A detailed study of PIM solution behavior could elucidate how microporous polymers relate to previously studied polymer systems, especially in terms of scaling with known physical parameters. Many of the rheological properties of PIMs are not widely known in the literature and could be used to predict the behavior of PIMs using recognized polymer interaction relationships.

Although PIM membranes for gas separations have been extensively studied in the literature, many aspects of applying these materials to other separations are largely unexplored. The techniques developed here for the study of PIM-1 could easily be applied to understanding new PIM systems. Although spinning of new polymers is indeed possible, the process can be quite time and labor intensive to develop. The PIM-1 hollow fibers fabricated in this work could be post-synthetically modified to access PIMs with different functionality without the need for redeveloping the spinning process. As long as the

asymmetric structure is not severely compromised in the chemical transformation, similar defect treatments could also be applied to the functionalized fiber to heal defects that have developed. Given the general design principles governing PIMs, many new microporous polymers that have not been reported in the literature could also be imagined. These new materials could then be evaluated for organic solvent separations via methods described previously in this work.

As discussed, many parameters directly impact the formation of CMS. The effect of pyrolysis protocol was the primary factor investigated here as a means to create more selective membranes. This particular protocol and final pyrolysis temperature have not been optimized for any specific separation, as the intent of this work was to demonstrate a simplified fabrication of asymmetric CMS hollow fiber membranes for proof-of-concept OSRO separations. The effects of pyrolysis atmosphere, temperature profile, and pretreatments could be significantly improved to form PIM-1-derived membranes with superior permeance and selectivity for a targeted separation. Temperature-dependent sorption and diffusion measurements of organic solvent molecules of interest can further elucidate the role of enthalpic and entropic selectivity to the diffusion selectivity. The PIM-1 membranes used here were fairly aggressively defect-treated to produce more robust, yet less permeable membranes for OSRO testing. The result of this treatment is shown in Figure 8.1. The radially asymmetric PIM-1 membrane develops a very distinctive skin layer after defect treatment and pyrolysis. A less aggressive defect treatment should produce CMS fibers with thinner skin layers and higher permeance.

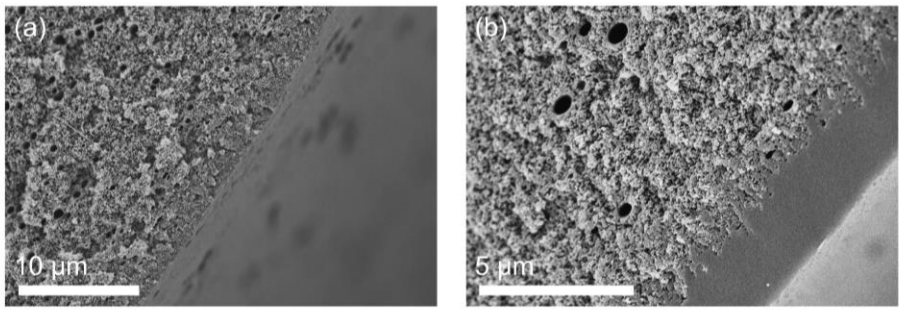

Figure 8.1 (a) Skin layer of an as-spun PIM-1 hollow fiber membrane. (b) Skin layer of a 50 wt% DMF/water treated and pyrolyzed CMS hollow fiber membrane.

Further material characterization of the CMS is needed as well. Determination of the pore size and pore size distribution of the CMS is critical for being able to tailor the material to a specific separation of interest. As explained previously, cryogenic physisorption techniques proved invaluable for elucidating much information about the PIM-1 CMS pore size and distribution. Instead, gas permeation at or above ambient temperatures could be used to determine an effective pore size cutoff. By comparing the pure component permeances of different gases with known sizes, an effective pore size can be estimated—similar to work done on inorganic membranes. Larger gas molecules up to SF_6 are of comparable kinetic diameter to the smaller hydrocarbon fluids and could be used to evaluate CMS materials for these separations.

Many practical aspects of the existing membrane formation and module fabrication techniques influenced the solvent separations studied. The auxiliary components required for assembling membrane modules are often overlooked for more forgiving feed mixtures such as noncorrosive gases and water. Moreover, the separation of organic solvents can be quite harsh on the entire membrane module. Appropriately solvent- and pressure-resistant auxiliary components are critical to the success of OSRO. A single solvent-resistant epoxy

was used in this work as it is stable under elevated temperatures and pressures in the presence of cycloaromatics. However, this epoxy is not suitable for organic liquid separations that involve oxygenated species such as alcohols. Matching the epoxy/solvent compatibility with the separation of interest is another hurdle to overcome in enabling practical testing of OSRO membranes. Moving away from epoxy-based adhesives to chemically inert glass-based sealants is a possible solution to separating a variety of solvents with a single membrane module. Very high temperatures—sometimes as high as 800°C—are required to melt the glass and form the seal. It is unclear what changes to the CMS structure will occur under those conditions after initial pyrolysis, although it is likely to be similar to rapid physical aging.

8.3 Critical Needs

Several more broadly applicable needs are required in the field to realize success in these new and increasingly difficult molecular separations. The most pressing and potentially impactful needs are highlighted and discussed along with suggestions for further research on the topic.

8.3.1 Pore Size Control

When using microporous materials, controlling the pore size is key to obtaining high degrees of size and shape selectivity. The pore size, pore size distribution, and pore chemistry can all significantly affect the resulting separation performance of the membrane. Current research on microporous materials has identified and characterized many smaller pore materials suitable for gas separations (less than 6 Å pores) and some larger pore materials for OSN (greater than 15 Å) and other filtration-type separations.

However, there is a dearth of information for "midrange" microporous materials (6-15 Å) that would be most suitable for the separation of small organic liquids (e.g., xylene isomer separation from 1,4-diethylbenzene). Although many organic liquid systems have solutes/solvents with sizes in excess of 15 Å, current OSN technology is not refined enough to differentiate between molecules in these systems yet (i.e., OSN membranes cannot yet differentiate a 15 Å molecule from a 17 Å molecule).[3]

Large pore MOFs are another potential candidate for organic liquid separations. However, MOFs like ZIF-8 are known to undergo structural transitions under elevated pressures, sometimes even forming completely dense phases.[4,5] The nature and reversibility of these transitions vary depending on the material and need to be considered before utilization for organic liquid separations that require large applied pressures. Indeed, the susceptibility to amorphization under pressure of large pore MOFs relative to ZIF-8 is still unknown. While there are a number of large pore materials that could enable organic liquid separations, the same issues noted earlier associated with continuous, defect-free membrane fabrication exist. The most promising route for quickly assessing the performance of these materials may lie in mixed matrix membranes. Utilizing these large pore materials as fillers circumvents the needs to produce large quantities of materials, fabricate standalone membranes, and utilize different testing apparatuses. Moreover, it is possible to conduct detailed transport analysis for materials in this morphology under different operating modalities, although understanding of the individual material properties and the determination of an appropriate model is necessary.[6-8] Screening of multiple new materials simultaneously is also possible, especially with the aid of molecular modeling of sorption and diffusion in crystalline materials;[9] there is still a critical need to improve

modeling tools for the area of transport in amorphous microporous materials. As previously discussed, compatibility between the continuous polymeric phase and the discrete filler phase need to be considered. Zeolites have the least favorable interactions, while MOFs and COFs adhere to the polymer much better.

Even though a significant number of possible large pore fillers and polymers exist, the most effective approach for studying the effects of pore size control on separation performance would be via the establishment of different platform materials. A single platform material would allow for changes to the pore size with minimal changes to the rest of the system, which simplifies transport analysis and comparisons made between different membranes. A few of the microporous materials previously discussed could become platform materials if key issues are resolved. For instance, MOFs and COFs have potential to be platform materials due to the relative ease of modifying the synthesis procedure and possible post-synthetic modifications that allow for the creation of families of modified materials. Hybrid MOFs based on ZIF-8 and ZIF-90 are an exemplary illustration of a platform material for gas separations.[10,11] The pore aperture can be finely tuned via the introduction of different linkers into the ZIF structure without changing the crystal topology. In this way, changes to the effective pore aperture are easily related to the changes in organic molecule diffusion,[11] while secondary effects that might typically complicate comparison between different materials such as changes in topology, particle size, exposed facets, etc. are minimized in this platform approach. The primary issues hindering MOFs and COFs from being platform materials for OSRO straightaway are related to their fabrication into defect-free membranes and uncertain performance under high pressures and organic liquid feeds.

Carbon membranes are another potential platform material. The pore size of CMS membranes are largely controlled by minor changes to the pyrolysis conditions.[12-15] Therefore only a single polymeric precursor is needed to generate a variety of different pore size CMS. However, the critical limitation is the formation of large CMS pores in the 6-15 Å range. Pyrolysis of common polymer precursors tends to lead to ultramicroporous membranes with pore sizes less than 6 Å, which is more suited for gas separations rather than organic liquid separations. Breakthroughs in the formation of large pore polymeric precursors or the formation of larger pores during pyrolysis will enable the use of CMS membranes for more varied separations.

Although zeolites have shown the most promise as size- and shape-selective microporous materials, the lack of diverse structures compared to MOFs and anticipated poor performance with very high sorbate loadings will likely prevent them from being considered as a platform material for organic liquid separations, although they have immense potential in certain applications (e.g., *p*-xylene/*o*-xylene separation).

Being able to control the pore size and pore size distribution is key to fabricating functional separation materials. However, being able to determine what types of separations those pores enable is another challenge. When independent determination of a material's pore size is not feasible through methods such as physisorption, membrane performance can be used as a practical gauge of pore size. Currently, there is significantly more transport data available for small molecules—such as gases—in microporous materials than for larger organic molecules. The little organic molecule data that exists is generally limited to equilibrium sorption isotherms that do not elucidate much about the transport or diffusive aspects of the system—factors that are critical to size- and shape-

selective membranes. Analytical techniques such as PFG NMR can shed insight into the self-diffusion of organics in microporous materials.[16] Membrane permeation experiments are clearly needed to assess the performance of the material, although significant variations in testing can be somewhat problematic. Temperature dependent measurements are also lacking in the literature, but are needed to provide fundamental insight into understanding the driving forces for permeation and selectivity.

8.3.2 Scalable Microporous Membrane Materials

Decades of research on microporous materials and membranes has produced a significant number of promising candidate materials, yet very few industrial-scale membranes have been realized. The bulk of commercially available membranes are polymeric materials fabricated via interfacial polymerization.[17] Cost-effective control of the defect concentration is the major challenge facing all membrane devices. Indeed, the advent of straightforward, large-scale membrane post-treatments enabled the mass production of low-cost polymeric gas separation membranes. To date, equivalent solvent-resistant post-treatments have not been developed. Fundamental understanding of defect formation not only during synthesis of the material, but in the membrane fabrication process, will lead to improved membrane processing techniques. Internal defects in crystalline materials like MOFs have been studied as well, although it is unclear how these defects affect membrane formation.[18]

Regardless of the means of controlling defects, high throughput and scalable fabrication are essential prerequisites to enabling membrane technology. Laboratory research tends to focus on the synthesis of high performance materials, rather than

membrane device fabrication. However, it is often significantly more challenging to adapt high performance materials with complex syntheses into specific membrane morphologies (like hollow fibers) than to start from materials already demonstrated in that morphology. Critically, the field needs to consider membrane fabrication from the onset of research rather than as an afterthought, as this will streamline the transition from laboratory to practice. Solution processable polymeric membranes currently lead the way in ease of fabrication, scalability, and the path from fundamental materials research to modular device engineering is well-established. Carbon membranes possess many of those same advantages since they are derived from polymeric precursors, although they are subject to their own fabrication challenges when pyrolyzing hundreds of fibers simultaneously; however, this is likely not an insurmountable challenge.[19] Meanwhile, MOFs and zeolite membranes still suffer from difficulties in producing large surface area membranes without cracks.

8.3.3 Consistent Methods, Testing, and Analysis

As an emerging field, organic solvent separations have yet to fully establish consistent nomenclature, methodologies, and analytical standards like the gas and water separation fields. Currently, different metrics have been used to define the types of separations occurring, generally based on the IUPAC definitions of solute size (i.e., reverse osmosis, nanofiltration, ultrafiltration, microfiltration). This convention has worked well for aqueous separations since the solvent remains water in all cases. However, this convention becomes muddled when applied to organic solvent separations where the size of the solvent can vary significantly. This convention breaks down further when separating isomeric mixtures where even the term solvent is unclear. Basing a new convention on the relative

size difference of the solute and solvent can also be problematic as the size range of the molecules becomes very large in organic systems. In the case of separation systems enriching the permeate (i.e., RO, NF, etc.), one potential approach that could be effective for permanently porous materials is to delineate RO/NF based on the difference in size of the fastest permeating molecule and the limiting pore size in the membrane material. Sufficiently small size differences between these two will inhibit a hydraulic driving force for permeation, which would classify the separation as a "reverse osmosis" modality. If hydraulic driving forces adequately describe transport of the fastest permeating molecule, then the conventional NF/UF/MF classifications can be used based on the differences between the slowly permeating component and the membrane's pore size.

Along the same lines as establishing more precise nomenclature, identifying and defining standardized mixtures as proxies for relevant feeds and membrane testing guidelines is needed. Lab-scale research currently utilizes organic dyes and polystyrene oligomers to determine the performance of OSN membranes and are adequate for initial characterization.[20] However, these solutions differ substantially compared to actual feeds encountered by OSN membranes. Trace contaminants are the most concerning aspect of moving from synthetic to actual feeds. Especially for polymers, MOFs, and zeolites that are susceptible to decomposition in acidic and/or basic conditions, stability testing under real feeds is critical. For OSRO, *p*-xylene/*o*-xylene separations represent an important industrial chemical feedstock. However, this is by no means the only relevant mixture, and collaboration between industry and academia could provide additional insight into organic solvent mixtures to help direct future research. In addition, membrane operation can be as important as the choice of feed mixture. Testing under dead end filtration as opposed to

continuous flow can lead to varying results for the exact same system, and continuous flow should be utilized where possible.

Fundamental membrane analysis and modeling quickly becomes complex when moving from relatively ideal systems (such as gas) to fairly non-ideal systems like organic liquid mixtures. Non-idealities of the liquid-phase driving force quickly lead to very complicated transport models and the formation of uniform transport analysis would be beneficial to the field. Even the establishment of consistent units and simplifying assumptions would improve the accuracy and uniformity of the transport analysis, as done previously in the gas and water separation fields. Modeling of membrane performance in the context of organic solvent separations has helped determine system operating limits. Livingston et al. have developed models of various polymeric OSN membrane systems to better understand which membrane and module properties are industrially relevant; a similar analysis would be highly beneficial for the development of OSRO.[21,22]

8.4 References

(1) Jue, M. L.; McKay, C. S.; McCool, B. A.; Finn, M. G.; Lively, R. P. Effect of Nonsolvent Treatments on the Microstructure of PIM-1. *Macromolecules* **2015**, *48*, 5780-5790.

(2) Jue, M. L.; Breedveld, V.; Lively, R. P. Defect-free PIM-1 hollow fiber membranes. *J. Membrane Sci*. **2017**, *530*, 33-41.

(3) Song, Q.; Cao, S.; Pritchard, R. H.; Ghalei, B.; Al-Muhtaseb, S. A.; Terentjev, E. M.; Cheetham, A. K.; Sivaniah, E. Controlled thermal oxidative crosslinking of polymers of intrinsic microporosity towards tunable molecular sieve membranes. *Nat. Commun*. **2014**, *5*.

(4) Chapman, K. W.; Halder, G. J.; Chupas, P. J. Pressure-Induced Amorphization and Porosity Modification in a Metal−Organic Framework. *J. Am. Chem. Soc*. **2009**, *131*, 17546-17547.

(5) Ortiz, A. U.; Boutin, A.; Fuchs, A. H.; Coudert, F.-X. Investigating the Pressure-Induced Amorphization of Zeolitic Imidazolate Framework ZIF-8: Mechanical Instability Due to Shear Mode Softening. *J. Phys. Chem. Lett*. **2013**, *4*, 1861-1865.

(6) Zornoza, B.; Tellez, C.; Coronas, J.; Gascon, J.; Kapteijn, F. Metal organic framework based mixed matrix membranes: An increasingly important field of research with a large application potential. *Micropor. Mesopor. Mat*. **2013**, *166*, 67-78.

(7) Jia, Z.; Wu, G. Metal-organic frameworks based mixed matrix membranes for pervaporation. *Micropor. Mesopor. Mat*. **2016**, *235*, 151-159.

(8) Vinh-Thang, H.; Kaliaguine, S. Predictive Models for Mixed-Matrix Membrane Performance: A Review. *Chem. Rev*. **2013**, *113*, 4980-5028.

(9) Chung, Y. G.; Camp, J.; Haranczyk, M.; Sikora, B. J.; Bury, W.; Krungleviciute, V.; Yildirim, T.; Farha, O. K.; Sholl, D. S.; Snurr, R. Q. Computation-Ready, Experimental Metal–Organic Frameworks: A Tool To Enable High-Throughput Screening of Nanoporous Crystals. *Chem. Mater*. **2014**, *26*, 6185-6192.

(10) Thompson, J. A.; Blad, C. R.; Brunelli, N. A.; Lydon, M. E.; Lively, R. P.; Jones, C. W.; Nair, S. Hybrid Zeolitic Imidazolate Frameworks: Controlling Framework Porosity and Functionality by Mixed-Linker Synthesis. *Chem. Mater*. **2012**, *24*, 1930-1936.

(11) Eum, K.; Jayachandrababu, K. C.; Rashidi, F.; Zhang, K.; Leisen, J.; Graham, S.; Lively, R. P.; Chance, R. R.; Sholl, D. S.; Jones, C. W.; Nair, S. Highly Tunable Molecular Sieving and Adsorption Properties of Mixed-Linker Zeolitic Imidazolate Frameworks. *J. Am. Chem. Soc*. **2015**, *137*, 4191-4197.

(12) Zhang, C.; Koros, W. J. Ultraselective Carbon Molecular Sieve Membranes with Tailored Synergistic Sorption Selective Properties. *Adv. Mater*. **2017**, *29*, 1701631.

(13) Geiszler, V. C.; Koros, W. J. Effects of Polyimide Pyrolysis Conditions on Carbon Molecular Sieve Membrane Properties. *Ind. Eng. Chem. Res*. **1996**, *35*, 2999-3003.

(14) Kiyono, M.; Williams, P. J.; Koros, W. J. Effect of pyrolysis atmosphere on separation performance of carbon molecular sieve membranes. *J. Membrane Sci*. **2010**, *359*, 2-10.

(15) Fu, S.; Wenz, G. B.; Sanders, E. S.; Kulkarni, S. S.; Qiu, W.; Ma, C.; Koros, W. J. Effects of pyrolysis conditions on gas separation properties of 6FDA/DETDA:DABA(3:2) derived carbon molecular sieve membranes. *J. Membrane Sci*. **2016**, *520*, 699-711.

(16) Forman, E. M.; Trujillo, M. A.; Ziegler, K. J.; Bradley, S. A.; Wang, H.; Prabhakar, S.; Vasenkov, S. Self-diffusion of heptane inside aggregates of porous alumina particles by pulsed field gradient NMR. *Micropor. Mesopor. Mat*. **2016**, *229*, 117-123.

(17) Lee, K. P.; Arnot, T. C.; Mattia, D. A review of reverse osmosis membrane materials for desalination—Development to date and future potential. *J. Membrane Sci*. **2011**, *370*, 1-22.

(18) Sholl, D. S.; Lively, R. P. Defects in Metal–Organic Frameworks: Challenge or Opportunity? *J. Phys. Chem. Lett*. **2015**, *6*, 3437-3444.

(19) Karvan, O.; Johnson, J. R.; Williams, P. J.; Koros, W. J. A Pilot-Scale System for Carbon Molecular Sieve Hollow Fiber Membrane Manufacturing. *Chem. Eng. Technol*. **2013**, *36*, 53-61.

(20) Marchetti, P.; Jimenez Solomon, M. F.; Szekely, G.; Livingston, A. G. Molecular Separation with Organic Solvent Nanofiltration: A Critical Review. *Chem. Rev*. **2014**, *114*, 10735-10806.

(21) Marchetti, P.; Livingston, A. G. Predictive membrane transport models for Organic Solvent Nanofiltration: How complex do we need to be? *J. Membrane Sci*. **2015**, *476*, 530-553.

(22) Shi, B.; Peshev, D.; Marchetti, P.; Zhang, S.; Livingston, A. G. Multi-scale modelling of OSN batch concentration with spiral-wound membrane modules using OSN Designer. *Chem. Eng. Res. Des*. **2016**, *109*, 385-396.